2018-01-01

Hybrid 3d Printing Demonstrated By Arbitrary 3d Meandering Transmission Lines

Ubaldo Robles
University of Texas at El Paso, Ubaldo.Robles@gmail.com

HYBRID 3D PRINTING DEMONSTRATED BY ARBITRARY 3D MEANDERING TRANSMISSION LINES

UBALDO ROBLES DOMINGUEZ

Doctoral Program in Electrical and Computer Engineering

APPROVED:

Raymond C. Rumpf, PhD., Chair

Bryan Usevitch, PhD.

Thompson Sarkodie-Gyan, Ph.D.

Deidra R. Hodges, Ph.D.

Peter N. Kim, Ph.D.

Kenneth H. Church, Ph.D.

Paul I. Deffenbaugh, PhD.

Charles Ambler, Ph.D.
Dean of the Graduate School

Dedication

To my Lord who provided the life, time, and guidance. My family, especially to my wife, my Intervarsity students, my EM Lab colleagues, and my mentor Raymond "Tipper" Rumpf. All who have helped me focus on today's efforts towards a better version of myself.

"No person can break the boundary of knowledge by themselves"

-Ubi

HYBRID 3D PRINTING DEMONSTRATED BY ARBITRARY 3D MEANDERING TRANSMISSION LINES

by

UBALDO ROBLES DOMINGUEZ M.S. in E.E.

DISSERTATION

Presented to the Faculty of the Graduate School of

The University of Texas at El Paso

in Partial Fulfillment

of the Requirements

for the Degree of

DOCTOR OF PHILOSOPHY

Department of Electrical and Computer Engineering

THE UNIVERSITY OF TEXAS AT EL PASO

December 2018

Acknowledgements

I fully acknowledge the support and patience my family Dalia Dominguez Carrasco and Eduardo Robles Sandoval whose parental love and dedication enabled me to start life on the right foot. My unconditional love and wife, Jennifer Marie Lamon-Robles – "you have become one of the strongest pillars in my life." My loving siblings Dalhia Robles Dominguez and Eduardo Robles Dominguez who set the example before me to follow and think ahead. My grandmother Elia Carrasco Lujan whose strength and dedication showed me that persistence and hard work brings success in life. My grandfather, Silvino Robles a man of few words but strong ethics. To all my extended family that cheered me on through my education at UTEP.

I specially acknowledge the efforts, hours, wrestling, and care that Raymond "Tipper" Rumpf, Ph.D. has invested in my mentoring, training, and growth as a professional Engineer. - "I, honestly, believe you're the most dedicated teacher in my life."

I want to recognize the following professionals and friends that supported me and enhanced my ability to accomplish this dissertation

Paul I. Deffenbaugh, Ph.D.	Joseph Pierluissi, Ph.D.	Deidra R. Hodges, Ph.D.
Kenneth Church, Ph.D.	Cesar Valle	Ralph Loya
Peter N. Kim, Ph.D.	Jose Avila	Priscilla Bustamante
Thomas Weller, Ph.D.	Edgar Bustamante	Andelle Kudzal
Kenneth Church, Ph.D.	Noel Martinez	Hans Schenk
Harvey Tsang, Ph.D.	Jose Enriquez	Rebekah Fogleman
Javier Pazos, Ph.D.	Gilbert Carranza	Krissy Rumpf
Scott Starks, Ph.D.	Jesus Gutierrez	IV@UTEP Chapter Students

Financial support is provided by the following sources.

- Army contract # W911NF-13-1-0109, US ARMY RDECOM ACQ CTR - W911NF, Title: HBCU/MI: 3D Formable RF Materials and Devices
- The Texas Office of the Governor, Rick Perry under the Texas Emerging Technologies Fund
- Raytheon Space and Airborne Systems

Facilities and in-kind support is provided by the following sources.

- Army Research Lab
- at the University of Texas at El Paso
  - EM Lab
  - ECE Department
  - PNE Lab
  - The W.M. Keck Center
- nScrypt, Inc. and Sciperio, Inc.
- Intervarsity Christian Fellowship
- WAMI Lab at the university of South Florida

Table of Contents

List of Tables

List of Figures

Chapter 1: Introduction

This dissertation focuses on the automation of multi-material direct write three-dimensional (3D) manufacturing of arbitrary metal-dielectric structures. The technology was demonstrated by manufacturing 3D meandering interconnects and transmission lines (TLs). Manufacturing 3D functional electronics with multiple materials required pushing the current state of 3D printing (3DP) technology to utilize simultaneous multi-material processes combined with sophisticated slicing and bonding under one process. Multi material 3DP is known as hybrid 3DP. This research pioneered the process for producing meandering transmission lines, starting with design and manufacturing, using hybrid 3DP through micro-dispensing and fuse deposition modeling. The research starts by 3DP magnetic and dielectric 3D structures using micro-dispensing. A comparison of 3D filters to their industry standard counterparts is shown. A new way of slicing 3D parts for hybrid 3DP is created and various demonstration parts are 3D printed.

1.1 Problem Statement

Electromagnetics and circuit technology remain stuck in two dimensions, primarily due to limitations in manufacturing. When most people hear the term "3D circuit," they envision what are essentially planar circuits connected vertically through vias. This is perhaps better described as 2.5D since use of the third dimension remains highly limited. A true 3D circuit, as envisioned in this research, is a circuit where all three dimensions have equal freedom. Components can be located at any position and be in any orientation. This greater design freedom will make circuits smaller, lighter, more power efficient, and exhibit greater bandwidth [1]. A 3D circuit can be produced in virtually any form factor imaginable. Even more, the third dimension offers physics that cannot be exploited in 2D, making it very possible that 3D circuits will vastly outperform conventional 2D circuits. To make this possible, 3D printing has recently evolved from mere rapid prototyping to a manufacturing technology capable of producing final products [2]. 3D printing offers the ability to deposit small amounts of materials in three dimensions with high precision [3]. It can build parts with complex geometries that are impossible to produce by other approaches [2]. This promises a very 3D future for electromagnetics and circuits.

Aside from huge manufacturing challenges, there are serious electromagnetic problems with 3D circuits that are especially pronounced at high frequencies. There can be no ground planes in a 3D circuit

because a ground plane is fundamentally a 2D concept. The ground plane, however, is critical in high frequency electrical circuits to confine fields, maintain clean signals, participate in thermal management, and distribute power. In fact, virtually every aspect of modern circuits utilizes a ground plane. To work around this, entirely new practices must be developed in order to evolve electromagnetics and high frequency circuits into three dimensions.

The vision for this research is very 3D, where all components will be imbedded in media in any position and any orientation. Making the components and signal traces part of the volume of the electronic. Before any of these problems can be studied, the design methodologies and manufacturing processes must be developed to form the electrical interconnects between active components. Direct current (DC) and low frequency interconnects are much less problematic and virtually any conductive path will suffice [4]. High frequency interconnects in 3D circuits cannot require a ground plane and must do an excellent job of confining fields and isolating the signals from noise and interference. At a minimum, interconnects must be differential TLs. From a purely electromagnetic perspective, interconnects should be coaxial TLs, but certain differential lines are expected to be easier to manufacture. Interconnects need to be impedance matched to launch waves properly. Further, the TLs will meander smoothly throughout all three dimensions like splines in order to minimize parasitic impedances and maximize bandwidth.

1.2 BACKGROUND

There were several areas needed for this research effort. From computational electromagnetics to the signal testing of devices. In addition, 3D computer aided design to complete software control of 3D printers. Specifically, the background needed involves: high frequency microwave communication systems, extensive knowledge of additive manufacturing (AM), microdispensing of pads and structures, fused deposition modeling (FDM) or fused filament fabrication (FFF), and electronics manufacturing process using direct digital manufacturing (DDM) [4][6][7]. Finally, in order to evaluate the hybrid 3D printing process and test the manufactured devices there was a need for different computational electromagnetic simulation approaches to optimize the performance of the intermediate steps and final product of this research.

1.3 STATE-OF-THE-ART

Current circuits are exclusively two-dimensional, primarily, due to limitations in manufacturing [2]. During the 1930s, electronic circuits looked very 3D because their components were chunky and connected using thick wires that went in all directions [5]. Presently, conventional electronics utilizes the third dimension by stacking multiple layers creating a volumetric device [6]. One way this is being solved now, is the approach of using multi layers, flexible electronics, or even some 3D printing in the creation of multi-material 3D electronics [5]. Conventional manufacturing methods are process intensive and subtractive manufacturing of electronics produces much waste. The Dimatix printer lead the printed circuit effort by using inkjet technology to produce circuit vias on Kapton and other bendable surfaces making printed flexible electronics [10]. Similarly, there are many attempts to create fully 3DP high frequency devices; however, the attempts still take the approach of stacking due to the inconvenience of removing the ground plane [11]. It is a common practice on high frequency circuits to add baluns and tapers to design TLs [8][9]. The research community is working on the production of conductive filaments that facilitate the manufacturing of multi-material parts [12]. The W. M. Keck Center for 3D Innovation has taken the route of embedding solid wire onto 3D printed parts to increase conductivity and functionality on 3D high frequency circuits [1]. High-end multi-material printers by companies, like nScrypt, can handle manufacturing electronics using a variety of techniques and materials for 3DP antennas and circuits [13]. Production of low frequency digital electronics is happening in the W. M. Keck Center, University of Central Florida, The University of Texas at El Paso, and University of Delaware that prove the capabilities of AM to produce functional devices [6][13][15]. Further efforts by Sciperio and the University of Texas at El Paso have produced low frequency and high frequency 3D printed transmission lines using a planar approach [16]. The desire to create electronics with 3D printing has taken the industry to new levels of integrating different DDM processes onto one machine [17]. Unfortunately, there is virtually zero research devoted to exploring new concepts in circuits enabled by 3DP. There has not been a development on the next step of truly complex 3D printed high frequency systems until today [18]. The next step would be the manufacturing of TLs.

1.4 TECHNICAL APPROACH

This research develops a hybrid 3DP process for interconnects. In this research, TLs will be of different design than in conventional circuits because there is no ground plane, desire to exploit all three dimensions equally, no standard vias, smooth spline-like, creating intricate geometries that can handle high frequency, and improving on volume and weight usage. Figure 1.1 on the left, represents a conventional printed circuit board (PCB) with a planar approach that has standard interconnects all through its structure. On the right, the spatial advantages of exploiting the third dimension display an improvement in size reduction, material usage, and possible cost saving compared to the planar circuit. The design also has shorter traces making it more power efficient. In addition, electronic elements are imbedded in a support material and can be placed on arbitrary orientations. Consequently, fully using the third dimension will transform the way we think of building high frequency devices by becoming structural electronics, improving on designs when using the 3D dimension, and enhancing the performance of devices.

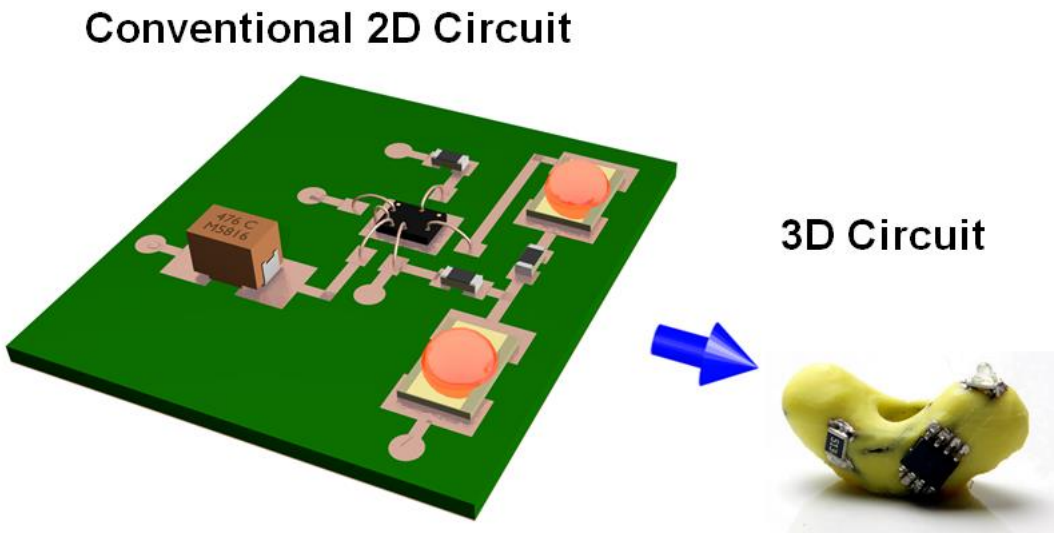

Figure 1.1: Representation of new concept electronics with intricate geometry and no ground planes

Furthermore, the next step of this research is to manufacture meandering TLs. The design for the TLs is 50 Ω. The ground planes will be omitted by using the parallel plate design. New ways of combining micro-dispensing of metals with FFF of plastics were developed in this manufacturing process. This was done by using a hybrid 3D printer equipped with both capabilities [19]. This process needs to be able to

3D print features down to the micron size level to make the meandering of TLs as smooth as possible and surface roughness, mismatched transitions, and scattering. This research uses nScrypt's approach of 3D printing, which is the capability of printing plastics and metals simultaneously with low high accuracy, high resolution, and very small tolerances.

Currently, PCB designs take a 2D approach of planar electronics, then stacking them on makes the designs 3D or 2.5D. By using the third dimension, the capabilities of designing electronics are open to more possibilities. Most TL designs are inherently two dimensional, but some can be taken as a base to consider building TLs in 3D. Coaxial lines, parallel plates, and two-wire are parts of the TLs that are easier to implement three-dimensionally. Other TLs require ground planes that cannot be used to meander in 3D space. The future of this research will be to implement parallel plate transmission lines (PPTLs) to connect electronic components dispersed throughout a 3D circuit. Figure 1.2 shows the concept of having a meandering PPTL move in any given orientation to connect circuit elements.

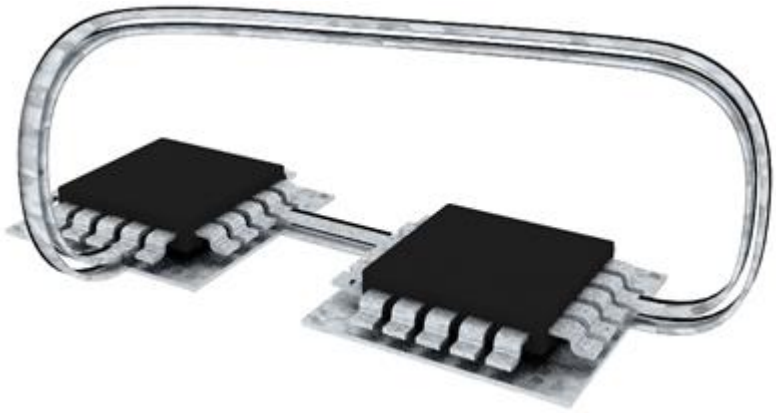

Figure 1.2: Concept design of a PPTL interconnecting two electronic components.

This research started with designing the basic PPTLs. Then it moved forward with developing the manufacturing methodologies for hybrid 3DP, studying the use of 3D printable materials using micro-dispensing and FFF, and designing printable models for different meandering PPTLs. It is essential to distinguish that this dissertation is not improving the already existing technology of transmitting and

receiving signals, but to evaluate design freedom and the manufacturing techniques of creating the devices that handle high frequency communications in three dimensions. Finally, the performance of the PPTLs were be quantified in volume, transmission, and losses. Future work should focus on more rigorous and accurate measurements of loss and impedance as this was outside of the scope and mission of the research described here.

The goal of this research is that next generation 3D circuits will be 3D printed with automated and multi-material processes, have TLs that are free to meander in space, require no ground planes, and will be built using DDM. This process is already producing a new generation 3D designs, further 3DP development, and enabling new research ideas [18]. Then, next generation electronics will have a new freedom in design, will be cheaper to manufacture due to savings in space and weight, have a faster prototype production, exploit the new physics that come with the third dimension, and have arbitrary form factors.

Chapter 2: Manufacturing Methodologies

3DP is a process where any given design model is processed through a slicing software creating layers with tool paths that contain instructions for dispensing the material that creates a functional part. After the 3DP process, there is a need for post processing to clean or cure the printed parts. Finally, an evaluation is necessary to ensure the quality and standards of the 3D manufacturing process. The diagram in Figure 2.1 explains the 3DP process we will be following to manufacture our PPTLs.

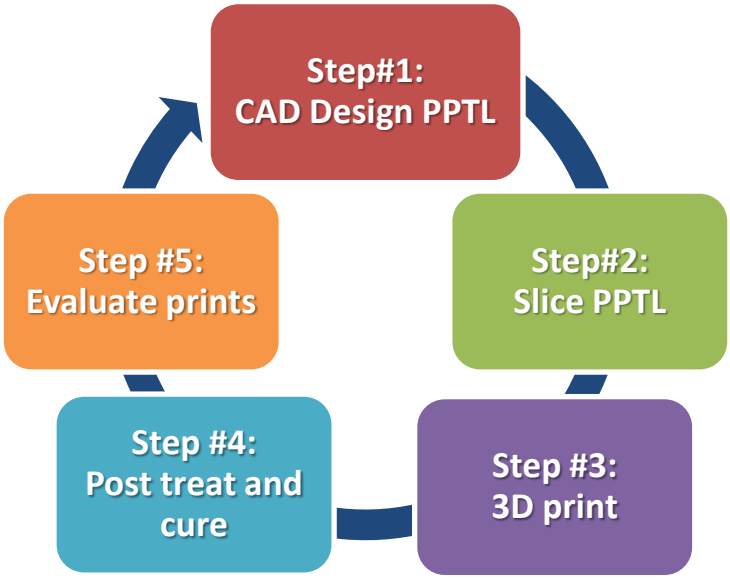

Figure 2.1: PPTL development process

This research required multiple aspects of manufacturing to create 3D PPTLs such as 3D printers, materials, post manufacturing techniques, and process rules. Table 2.1 categorizes and lists the various components needed to complete this research. The various items needed are described in this chapter. There are four main categories of items used to complete this research; they are divided in 3D printing technologies, software, and other machines that were mainly used for measurement, post-treatment of printed devices, and mixing. The 3D printing technologies used in this research are based on the nScrypt approach to 3D printing. The tools for micro-dispensing, FFF, and monitor the process are all provided

by nScrypt. The materials used are standard materials used in the 3D printing community because they are low loss, easy to handle, and have acceptable responses for manufacturing antennas, microstrips, and other electronic components [11]. The software used ranges from simulators, slicers, scripting programs, and tool controllers. This research added a hybrid-manufacturing step in the software tool chain by using creating a MATLAB based script needed to complete the tool chain from design to 3DP devices with more than two materials.

Table 2.1: Various items needed to complete this research

3D Printing Technologies	Materials	Software	Other Machines
nScrypt Table Top Series 3D Printer	DuPont CB028 silver ink	Motion Composer	Centrifuge
SmartPump™ 100	ABS filament for 3D Printing	MATLAB	Vacuum chamber
nFD™ pump	H2 Conductive epoxy	MTGen-3	500˚F Oven
Heating Elements	Optical epoxy EPO-TEK 353ND	Ansys HFSS	Vector Network Analyzer
Process view cameras	Distilled water	Slic3r	Weight scale
Ceramic pen tips	Acetone	Repetier-Host	Damaskos split-cavity resonator

The 3DP technologies needed to complete this research were driven mostly by an nScrypt Tabletop™ series 3D printer. This printer is capable of depositing filaments via nFD™ pump down to 12.5 μm line widths with a resolution of 0.1 μm. It can simultaneously deposit pastes via microdispensing with SmartPump™ 100 system since it controls volume down to 100 pL with a resolution of 0.1 μm [13][16][18]. In addition, the 3D printer can cure plastic filaments and silver ink with heat produced by the heat plate and the nFD™ pump [24]. Two process cameras were required to verify dispensing and structural integrity throughout the layers the process deposits.

Different software tools were used in order to process our design files for the 3D printed PPTLs. Solidworks was used to initially design the geometry of the TLs, then, The EM Lab team created a layout and signal routing tool based on Blender [18]. The designs were divided into separate STL files for the dielectrics and conductors. These STL files for the dielectric portion were processed using Slic3r, a free software tool that generates g-code from the STL file to drive the 3D printer. Then Repetier-Host was

used to bundle the ink and plastic under one file. Figure 2.2 shows the write path for hybrid 3DP. Initially, the STL file for the conductor portion was not used, it was a processed using an nScrypt proprietary software called PCAD that creates dispensing lines for the SmartPump™ system. However, for the purpose of this research a hybrid-slicing translator was created in MATLAB that was able to handle the metal ink portion of the print job and add it into one print job. Last, both file processes are interpreted into a single g-code file by the nScrypt Tabletop printer. The g-code file was translated into a manual pulse generator (MPG) code, which creates pgm files, that controls the microdispensing and fuse deposition pumps of the printer creating our PPTL devices. Therefore, the software developed to control the manufacturing of the TLs is of great importance to this effort. Figure 2.3 describes the multi-material slicing process to build PPTLs using two materials. Initially, two STL files composed of triangles and faces will be used to describe the materials needed to build our TLs. Consequently, the whole device will be divided in slices where plastics and metals will be dispensed accordingly. Finally, the slicing will produce tool paths, dispensing speeds, valve controls, needed for the 3D printer to dispense both materials to form the PPTLs.

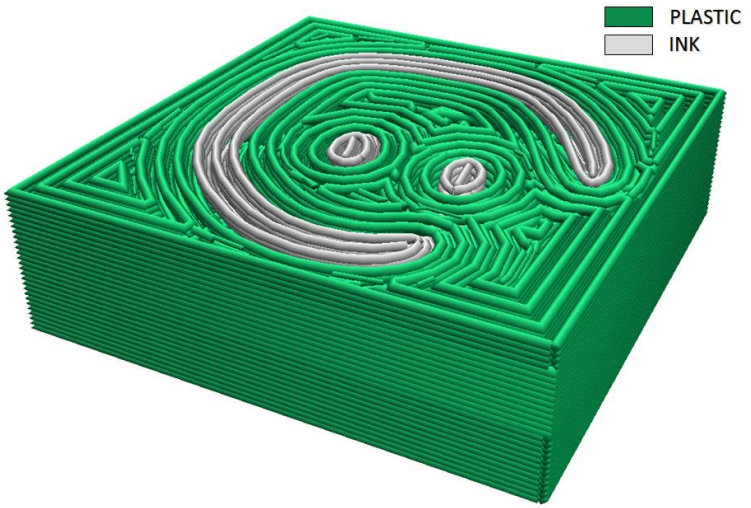

Figure 2.2: Software processed tool for hybrid 3DP

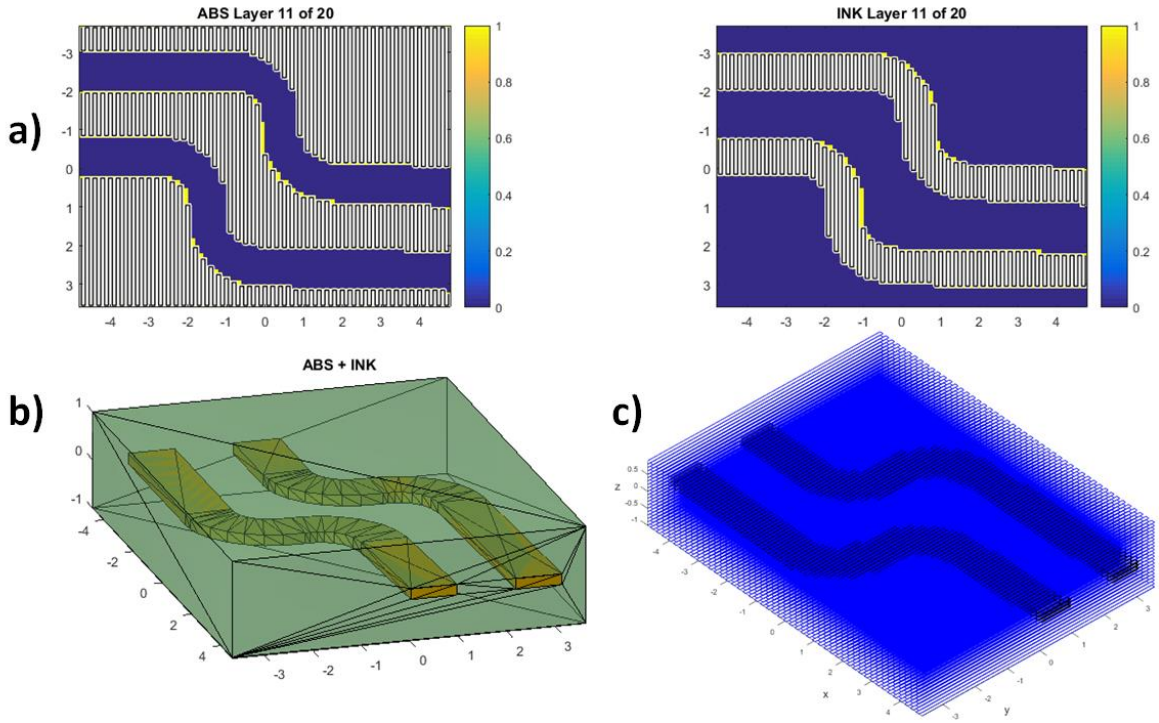

Figure 2.3: Description of multi-material slicing process. First, (b) two files will be joined and prepared for the slicing process. Then, (a) the whole device will be divided in layers where plastic (ABS) and metal (ink) will be dispensed accordingly. Finally, (c) the tool paths needed the 3D printer to dispense both materials to form the PPTLs under one print job.

When simulating PPTLs, copper with a sheet resistivity of ρ = 1.05 mΩ/sq/mil was used for the metal lines [25]. The SMA connectors we installed on the PPTLs with conductive silver epoxy H20E with a resistivity of ρ = 0.0004 cmΩ/sq/mil [26]. The metal parallel plates were fabricated using DuPont's CB028 silver ink. The dielectric constant of the ABS was measured using a Damaskos split-cavity resonator and vector network analyzer (VNA) to be 2.5 with a loss tangent of 0.005. Optical epoxy (EPO-TEK 353ND) was used to fix the standard SMA connectors on the plastic part of the substrates of the 3D printed filters to avoid connector breaks [27]. Needed parameters were simulated ANSYS® HFSS software and then compared them to the measurement results later on the testing sections of this effort [28].

For this research, there will be two types of problems during the manufacturing that will be either avertable or ineludible. Problems like warping, the distribution of ABS line grooves, ink leakage, under curing of inks, or smearing materials are avoidable since there are adjustments that can prevent these

problems. Problems like material debris, clogged pen tips, inhomogeneous ink flow, and filament lumps are ineludible since there are no solutions to treat these problems yet.

Characterization of the PPTLs was performed using an Agilent N5245A PNA-X VNA with a 1601-point sweep from 1 GHz to 10 GHz [29]. This was used to measure all microwave structures in this research. The main measurements looked for power loss, frequency responses up to 10 GHz, reflectance (S_{11}) and transmittance (S_{21}). After printing devices, we measured line width, layer thickness, overall size of the printed devices, curing time, porosity and material densities using an x-ray machine.

The PPTL design is a device that handles balanced signals as shown in Appendix A. The measuring VNA system is an unbalanced signal, that is, a single signal that works against a ground. In this case, the PPTLs can be measured using subminiature version A (SMA) connectors that are unbalanced. Typically, there is a need for a balun system that forces an unbalanced TL to feed a balanced component [8]. In this effort, we require a symmetric launch that maintains amplitude and phase enough to launch a signal. Baluns are not part of this research since we considered the TLs to be matched good enough to conduct a signal and be able to measure its performance. We are avoiding launch techniques and focus on the bare line. Similarly, we will be avoiding tapers or smooth SMA to PPTL transitions in this effort. Future work will focus on perfecting 3D printable launches between electronic elements and interconnects.

Chapter 3: 3D Printed Structures with Loaded Resins

Micro-dispensing is one of the first 3D printing technologies capable of manufacturing three-dimensional multi-material components [2]. In the present work, we adopted electromagnetic [30] and chemical [31] mixing rules to create materials for micro-dispensing using an nScrypt machine by mixing different powders into a high viscosity silicone host. To produce a material that prints small 3D structures reliably, we also considered the diameter of the dispensing pen tip, the size and shape of the particles loaded into silicone, and the viscosity of the final mixture. The objective is to allow the material to flow homogeneously through the pen tip without agglomerating or clogging the tip [31]. In this chapter, we demonstrated using different mixed materials and 3D printing processes. Then, by manufacturing small towers and bridges using silicone loaded with Strontium Titanate and ferrite powders. Our printing process included adjusting a variety of printing parameters as well as post treating the samples with heat curing. Lastly, the dielectric constant, permeability, and loss tangent of our materials were measured and the data summarized in this chapter [32].

3.1 Materials Development

Ultimately, materials are needed that satisfy two requirements. First, they must be suitable for 3D printing by micro-dispensing. The important characteristics that the ideal material needs are high viscosity to maintain shape during printing, small particles in order to manufacture small feature sizes, and homogeneous properties so that the process parameters do not have to be adjusted during the print [33]. Second, the materials must be able to accept a high range of powder loading while still being 3D printable using micro-dispensing. It is typically desired to minimize the electrical loss in dielectric materials [34]. The following sections outline our materials and methodologies.

3.1.1 Material Selection

Our materials selection consisted of two parts: (1) the host material, and (2) the loading materials [34]. From a micro-dispensing perspective, the ideal host material should have a high viscosity with low permittivity and permeability while the loading materials should have high permittivity and/or permeability. This allows us to mix fluids with suitable viscosity to produce 3D printed structures. At the same time, it is usually desired for the mixture to exhibit a very low loss tangent (tan $\delta < 0.01$), although some applications in shielding require high loss materials [31]. From a process perspective, the host material should be compatible with the loading materials and substrate. It should have a suitable viscosity so that 3D structures will not sag during printing before they can be cured [35]. The particle size of the loading material should be around one-tenth of the inner diameter (ID) of the pen tip in order to avoid agglomeration and clogging at the tip. Irregular shaped particles are harder to mix uniformly and agglomerate more easily [36]. Large particle sizes limit how small of a pen tip can be used, ultimately limiting how small of feature sizes one can realize. The outer diameter (OD) of the pen tip also affects the minimum feature size that can be printed because the paste tends to wick to the outside of the tip during printing [36]. While a small outer diameter is preferred, mechanical fragility is a concern for small size tips.

As the host material, we used SS-3045 silicone due to its higher viscosity and good chemical compatibility with our loading materials [37]. As the dielectric power, we chose Strontium Titanate ($SrTiO_3$) with 5 μm spherical particles due to its small particle size and ease of mixing [38]. We also used two different forms of ferrite powder to achieve a magnetic response at low frequencies. The first ferrite powder had irregularly shaped flake particles that varied in size from 1 μm to 75 μm. The irregularly shaped particles made the mixture very difficult to print. The second ferrite powder had spherical particles that varied in size from 50 μm up to 200 μm. This printed well, but limited the feature sizes that could be

realized. Images of the particles were captured on a scanning electron microscope (SEM) and are shown in Figure 3.1.

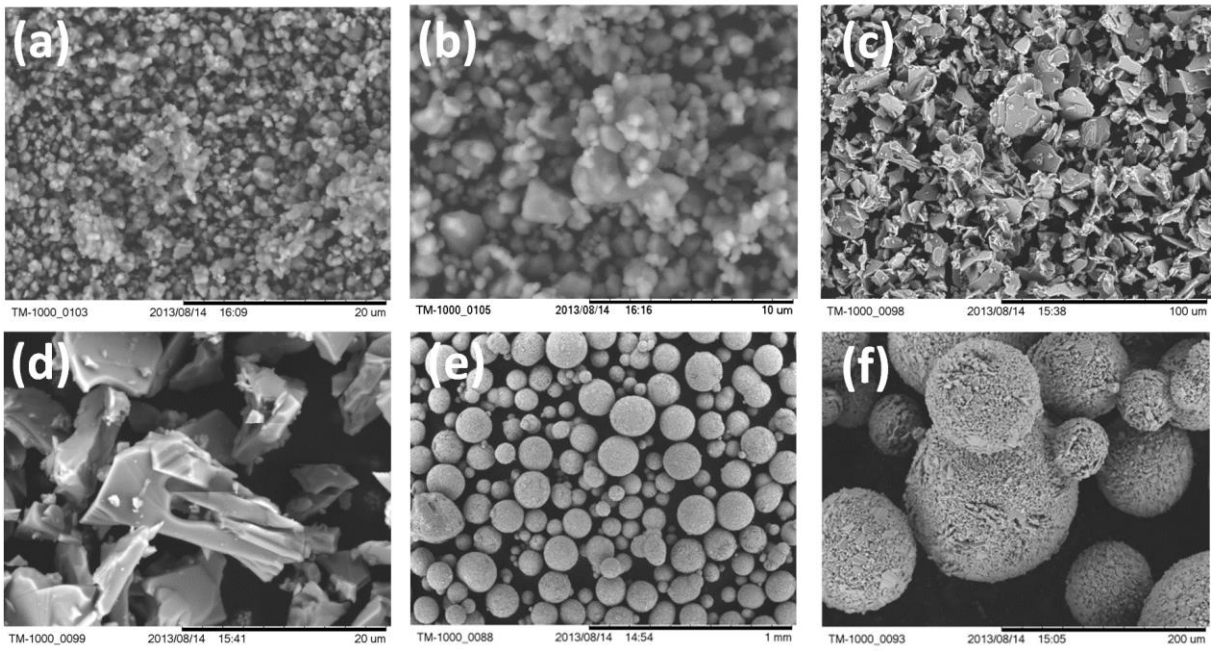

Figure 3.1: (a)&(b) SEM images of 5 μm SrTiO3 powder. (c)&(d) SEM images of ferrite flake powder. (e)&(f) SEM images of ferrite powder.

3.1.2 Electromagnetic Mixing Rules

In order to develop an accurate mixing rule, the statistics of the particle shape, size, and distribution must be determined accurately. These properties are often unknown or too difficult to obtain. Instead, the Weiner bounds are used to determine the maximum and minimum values for the dielectric constant of a mixture of two materials [39]. Given two materials with dielectric constants ε_1 and ε_2 and the volume fill fraction f_1 of the first material, these bounds are:

$$\frac{1}{\varepsilon_{\min}} = f_1 \frac{1}{\varepsilon_1} + (1 - f_1) \frac{1}{\varepsilon_2} \tag{0.1}$$

$$\varepsilon_{\max} = f_1 \varepsilon_1 + (1 - f_1) \varepsilon_2 \tag{0.2}$$

Many mixing rules can be found in the literature, but the following seem to offer the most insight because they consider the shape of the particle in addition to volume fill fraction. Given the dielectric constant ε_d of the pure crystal of the powder, its volume fill fraction f_d, and the dielectric constant of the host matrix ε_m, the overall dielectric constant ε_eff for three special cases are [34]:

Spherical Particles

$$\frac{\varepsilon_\mathrm{eff}}{\varepsilon_\mathrm{m}} = \frac{\varepsilon_\mathrm{d}\left(1+2f_\mathrm{d}\right)+2\varepsilon_\mathrm{m}\left(1-f_\mathrm{d}\right)}{\varepsilon_\mathrm{d}\left(1-f_\mathrm{d}\right)+\varepsilon_\mathrm{m}\left(2+f_\mathrm{d}\right)} \qquad \text{low } f_d \tag{0.3}$$

$$\frac{\varepsilon_\mathrm{eff}-\varepsilon_\mathrm{m}}{3\varepsilon_\mathrm{eff}} = \frac{\varepsilon_\mathrm{d}-\varepsilon_\mathrm{m}}{\varepsilon_\mathrm{d}+2\varepsilon_\mathrm{eff}} f_\mathrm{d} \qquad \text{high } f_d \tag{0.4}$$

Cylindrical Particles

$$\varepsilon_\mathrm{eff}-\varepsilon_\mathrm{m} = \frac{\left(\varepsilon_\mathrm{d}-\varepsilon_\mathrm{m}\right)\left(\varepsilon_\mathrm{d}+5\varepsilon_\mathrm{m}\right)}{3\left(\varepsilon_\mathrm{d}+\varepsilon_\mathrm{m}\right)} f_\mathrm{d} \qquad \text{low } f_d \tag{0.5}$$

$$1-f_\mathrm{d} = \frac{\left(\varepsilon_\mathrm{d}-\varepsilon_\mathrm{eff}\right)\left(2\varepsilon_\mathrm{m}+\varepsilon_\mathrm{d}+3\varepsilon_\mathrm{eff}\right)}{\left(\varepsilon_\mathrm{d}-\varepsilon_\mathrm{m}\right)\left(\varepsilon_\mathrm{d}+5\varepsilon_\mathrm{eff}\right)} \qquad \text{high } f_d \tag{0.6}$$

Flake Particles

$$\varepsilon_\mathrm{eff}-\varepsilon_\mathrm{m} = \frac{\left(\varepsilon_\mathrm{d}-\varepsilon_\mathrm{m}\right)\left(\varepsilon_\mathrm{m}+2\varepsilon_\mathrm{d}\right)}{3\varepsilon_\mathrm{d}} f_\mathrm{d} \qquad \text{low } f_d \tag{0.7}$$

$$\frac{\varepsilon_\mathrm{eff}}{\varepsilon_\mathrm{d}} = \frac{3\varepsilon_\mathrm{m}+2f_\mathrm{d}\left(\varepsilon_\mathrm{d}-\varepsilon_\mathrm{m}\right)}{3\varepsilon_\mathrm{d}-f_\mathrm{d}\left(\varepsilon_\mathrm{d}-\varepsilon_\mathrm{m}\right)} \qquad \text{high } f_d \tag{0.8}$$

The shape of the particle strongly affects the electromagnetic response. The electric field tends to bend toward the interfaces of the particle. The more irregular the shape, the more the fields are perturbed and the greater the electromagnetic response of the particle. For this reason, spheres produce the weakest

electromagnetic response while flakes produce the strongest. Cylinders respond somewhere between spheres and flakes. The spacing between particles also affects the electromagnetic response. When the particles are spaced far apart, they do not electromagnetically interact and the effective dielectric constant increases linearly with fill fraction. When the fill fraction is high, the particles are spaced close enough for them to interact and produce more perturbations to the field. This enhances the overall electromagnetic response. These models are plotted and compared in Figure 3.2.

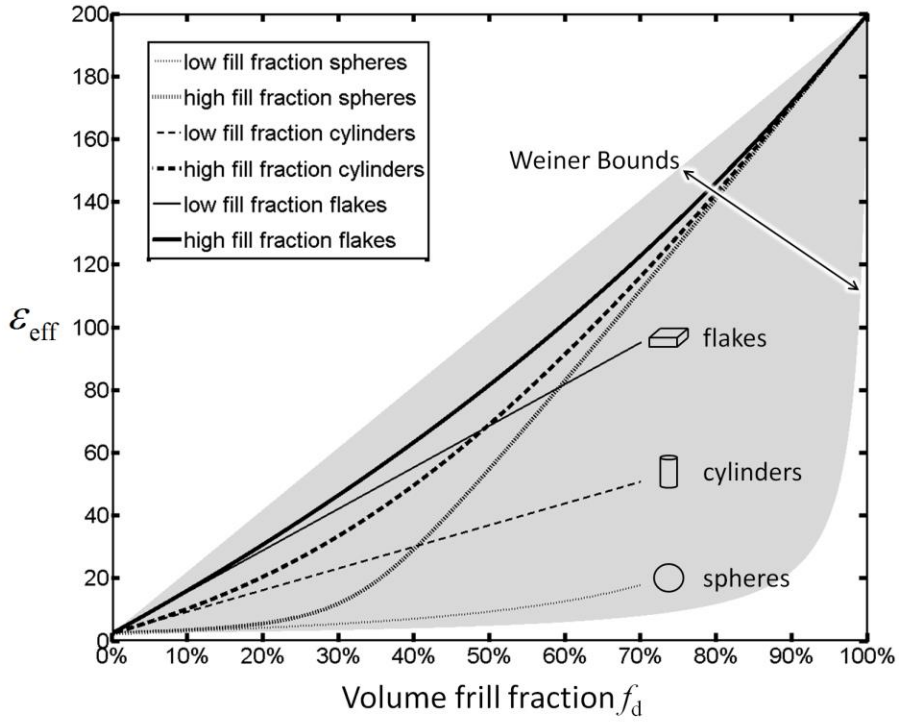

Figure 3.2: Comparison of electromagnetic mixing rules where host material has $\varepsilon_r = 2.5$ and the dielectric load has $f_d = 20\%$. Flake particles produce the strongest response while spheres produce the weakest.

3.2 EXPERIMENTAL PROCEDURES

The procedure for mixing materials with different loadings is based on the chemical dilution equation [31]. Our process consisted of two simple steps. First, a mixture was created with the highest possible percent loading of interest. Second, a controlled amount of silicone was added to lower the percent loading. For easier mixing, loading was determined by percentage weight (%*w*) as that was the

easiest quantity to measure. The density of the materials was taken into account to convert to percent loading by volume before applying equations (3.1) – (3.8).

For the initial mixture, we weighed both silicone and powder. If we mixed 50 grams of each, our final mixture was 50% by weight.

$$\%w = \frac{(\text{mass of powder})}{(\text{mass of powder}) + (\text{mass of silicone})} \tag{0.9}$$

Given this mixture, we calculated how much silicone we needed to add to dilute it to a desired loading using the dilution equation. While some variants of this equation can be found, we used the following where C_1 is the concentration by weight (%w) of the powder in the first mixture, M_1 is the weight of the first mixture, C_2 is the desired concentration in the second mixture, and M_2 is the total weight of the second mixture.

$$C_1 M_1 = C_2 M_2 \tag{0.10}$$

Continuing with the above example, suppose it was desired to mix our 50% mixture down to 30% by weight. Substituting

$$(50\%w)(100\text{ g}) = (30\%w) M_2 \tag{0.11}$$

Solving this for M_2 we get 166.7 grams. Since the first mixture already weighed 100 grams, is it necessary to add 66.7 grams of silicon to dilute the mixture to 30% by weight. Given the mass of the powder and silicone and their densities, the volume fill fraction f_d of the powder is calculated according to the following equation.

$$f_{\text{d}} = \frac{1}{1 + \frac{d_{\text{powder}}}{d_{\text{silicone}}} \frac{m_{\text{silicone}}}{m_{\text{powder}}}} \tag{0.12}$$

The materials were initially mixed by hand, and then placed in a planetary centrifugal THINKY mixer for fifteen minutes [40]. Lastly, the materials were finished using an orbital mixer with the following settings summarized in Table 3.1

Table 3.1: Orbital Mixing Procedures

Loading Material	Time (min)	Speed (rpm)
$SrTiO_3$	15	1200
$Fe(\text{flake particle})$	10	600
$Fe(\text{spherical particle})$	10	900

After mixing, the materials were treated in vacuum for at least 3 hours under 0.5 mbar pressure in order to remove bubbles. The materials were then loaded into syringes that were spun at 2000 rpm for 3 minutes to ensure even material distribution throughout the syringe and to avoid more bubbles from appearing.

3.3 EXPERIMENTAL RESULTS

In this research, we 3D printed a variety of samples for material characterization. The electrical properties were determined by placing samples in a X band waveguide (8.2 to 12.4 GHz), measuring transmission and reflection from the sample using a vector network analyzer, and calculating the permittivity and permeability following the Nicolson-Ross-Weir procedure [41]. The results tabulated are demonstrated in Table 3.2, and 3.3. The results are measured at a frequency of 10 GHz.

3.3.1 Dielectric Measurements from Printed Samples

We printed various samples using loadings of spherical dielectric powders. After measuring the mixtures, an increase of permittivity was observed as the loading percentage increased. However, the Smart Pump™ was not able to handle materials with more than 60% loading. As the loading got higher, the loaded mixture got thicker.

Table 3.2: Dielectric SrTiO3 Silicon mixture measurements

Loading (%)	Permittivity (ε_{eff})	Loss (tan γ)
0	2.8	0.001
10	3.1	0.003
26	3.6	0.023
34	4.2	0.046
60	10.58	0.039

3.3.2 Magnetic Measurements for spherical and flake particle samples

We printed magnetic samples of various loadings using the spherical and flake particle ferrite powders. Here the magnetic response was observed to be minimal. The responses from both particle shapes was very similar. Given the measured results, the materials need to be loaded up to 60 to 90 percent for the mixture to have a considerable magnetic response. However, the mixture was already very viscous and thick with the loadings at 20%.

Table 3.3: Magnetic mixture using flake particle powder (75 μm)

Loading (%)	Permeability (ε_{eff})	Loss (tan γ)
0	1.00	0.009
5	1.16	0.011
10	1.26	0.012
15	1.29	0.011
20	1.31	0.012

Table 3.4: Magnetic mixture using sphere particle powder (200 μm)

Loading (%)	Permeability (ε_{eff})	Loss (tan γ)
0	1.00	0.008
5	1.18	0.010
10	1.22	0.011
15	1.29	0.011
20	1.30	0.011

3.3.3 3D Printed Dielectric Structures

The target dimensions for a simple tower and bridge structure are depicted in Figure 3.3. These dimensions were easily realized with the dielectric material because the small spherical particles made it ideal for dispensing through a small pen tip.

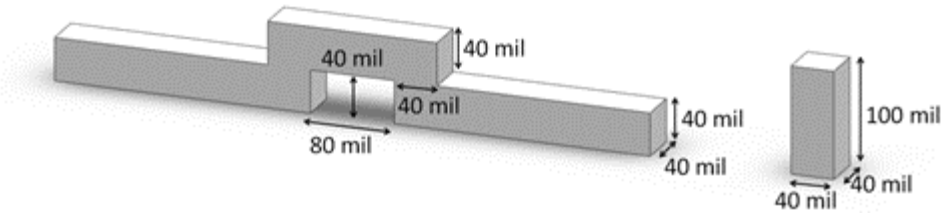

Figure 3.3: Target dimensions of towers and bridges

Process parameters were determined empirically for each material independently. The goal of the process parameters was to dispense the material with as close to zero momentum as possible. After determining the optimum parameters for a first representative mixture, determining the optimum parameters for other mixtures was a simple task because all of our materials were based on the same silicone host material. It is important to note that the high viscosity of the silicon resin proved to be most useful for building sturdy three-dimensional structures. The tower and bridge structures were built using a log stacking technique [36] in order to deposit the mixed paste and fabricate 3D structures as shown in Figure 4.4. The process parameters remained unchanged for all materials, namely: valve speed (5 mm/s) and print speed (7 mm/s). The other process parameters were adjusted according to the loading material and are summarized in Table 3.5.

Table 3.5: Printing parameters according to material

Loading Material	Pen Tip Size	Print Height	Pressure
$SrTiO_3$	50/100 μm	50 μm	26 psi
Fe(flake particle)	1.54 mm	1.35 mm	33 psi
Fe(spherical particle)	0.41mm	0.31 mm	45 psi

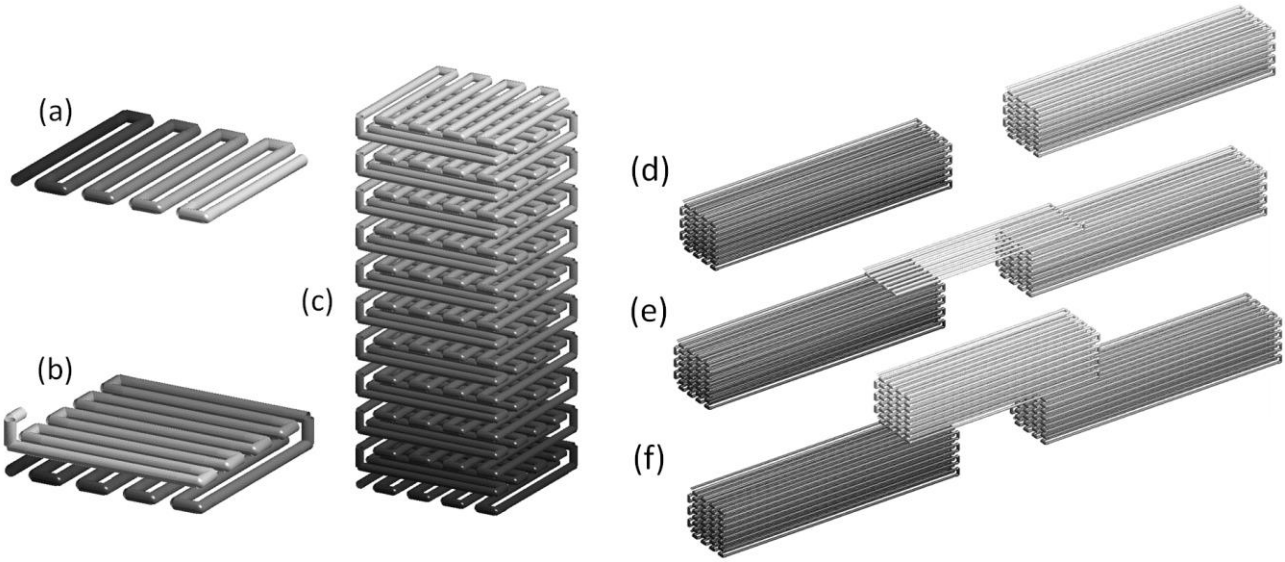

Figure 3.4: (a) Write path for first layer of tower. (b) Write path for second layer of tower. (c) Write path for entire tower. Shading of gray conveys order of print, dark to light. (d) Write path for the two supports. (e) Write path for first layer of bridge on supports. (f) Write path for entire bridge structure. Shading of gray conveys order of print, dark to light.

The micro dispensing parameters to print a bridge structure were identical to the tower structure. However, the write path was modified so that the lines were printed along the length of the bridge structure instead of alternating the pattern as in the log stacking technique. This was done to minimize sagging in the overhanging structure and is illustrated in Figure 3.4. The bridge was built without using any support material under the overhang section. The material mixture proved to be viscous enough to form a beam that held its shape until the bridge printing was completed and thermally cured.

The pen tip was chosen to print an optimal resolution given the dimensions of the structure as well as the particle size and shape that was loaded into the host silicone. A rule of thumb is to use a pen tip with inner diameter that is 10 times the size of the particles loaded into the resin. Spherical particles are ideal from a printing perspective because they are least likely to agglomerate. Irregular shaped particles require larger tip diameters in order to print reliably because the particles agglomerate easily.

Figure 3.5: (Left) micro-dispensing dielectric structures. (Center) 3D printed bridge with dielectric material. (Right) 3D printed towers with dielectric material. Both structures were printed with 75/100 μm ceramic pen tip.

For our initial work with the dielectric powders, 75/125 μm ceramic tips (inner/outer diameter) provided by nScrypt (801-0025-000 Ceramic ηTip) were used. The particles were on the order of 5 μm so the pen choice depended more on the desired feature than the powder itself. This choice gave us excellent feature size and the printing process was fast, simple, and consistent.

Photographs of 3D printed structures are shown in Figure 3.5. After optimizing the process, a small taper from bottom to top was observed. During dispensing, the structure is not yet cured and therefore not rigid. Then, it is pushed and pulled from side to side during the print resulting in slightly narrower dimensions near the top.

4.3.4 3D Printed Magnetic Structures

Realizing the target dimensions for the magnetic structures was more difficult. The larger and more irregularly shaped particle sizes required a larger pen tip that limited how small a structure can be printed. As such, tips from EFD Nordson (PN: 7024243, Rigid Tapered Tip) were used. Further, the size and shape of the particles resulted in a higher viscosity resin making it more difficult to achieve continuous flow for reliable printing. For these reasons, high viscosity needles with a tapered profile and nonstick Polyethylene material helped ease the flow control of materials and achieve the best structures. For the spherical ferrite and flake, ferrite powders a 0.64 mm and 0.84 mm high viscosity pen tips were used respectively. A larger pen tip was used for the flake powder to reduce the chance of agglomeration.

Photographs of the final magnetic structures are provided in Figure 3.6. The resolution of the ferrite structures was coarser than the dielectric structures due to having used larger pen tips. Even with the larger tips, some clogging due to agglomeration of the particles was occasionally experienced. This made the ferrite structures far more difficult to realize with the same resolution and percent loading as the dielectric structures.

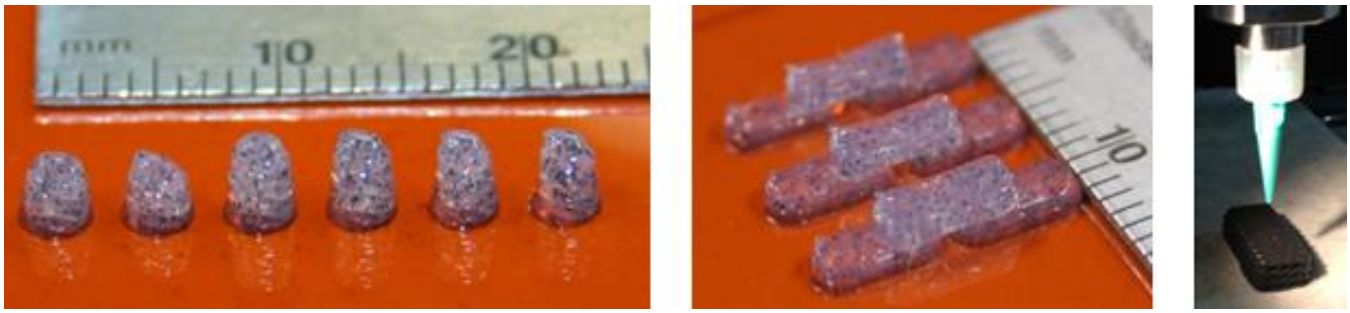

Figure 3.6: Final magnetic structures, towers printed through a 0.31 mm tip using silicon loaded with 10% 100 mm and ferrite powder bridge structure printed through 0.41 mm tip using silicon 10% loaded with 100 mm ferrite powder.

3.4 CONCLUSION

In order for 3D printing to manufacture products with electrical functionality, materials compatible with 3D printing with controllable electrical properties must be developed. In addition, 3D printing technologies capable of producing 3D parts with multiple materials must also be developed. Micro-dispensing is one of the first 3D printing techniques to produce multi-material parts with tailored electrical properties, but producing 3D structures by micro dispensing is relatively unexplored.

In this chapter, manufacturing of simple 3D structures by micro-dispensing is reported that were loaded with dielectric and magnetic powders to tailor the permittivity and permeability. Procedures for mixing materials and printing 3D structures were developed and summarized. As a proof of concept, simple towers and bridge structures with overall sizes on the order of 1 mm. Our host silicone material was sufficiently viscous for the structures to hold their shape during printing until they could be cured

afterward. Loading silicone with small spherical particles is ideal for printing, but larger irregular shaped particles provides a stronger electromagnetic response. This chapter shows the measured values for permittivity, permeability, and loss tangent for 3D printed structures at 10 GHz.

Chapter 4: 3D Printed High Frequency Filters

Mason and Sykes first introduced stepped impedance element filters in 1937 [42]. Then, the military desired this technology for use in radar, band limiting, multiplexing, and electronic counter measures on their attempt to step up from the analogue lumped filters used at the beginning of WWII. The Radio Research Laboratory did much of the early work on band-pass distributed impedance filter to develop coaxial filters for ECM applications [43]. Telecommunication companies and other organizations with large data networks applied the microwave filters to their data broadcasting [43]. Nowadays, both technologies are found over most high frequency devices including satellite dish receivers, cellphones, as well as sensitive measuring equipment.

Stepped and coupled-line impedance filters require no lumped elements, only two materials for manufacturing, and simple designs with breaks, stubs, holes, steps, and/or slits. These attributes make distributed element filters ideally suited to be 3D printed. Our two filter designs were: (1) a coupled-line bandpass filter, and (2) a stepped-impedance low pass filter. Both PCB and 3DP filter designs were based on microstrip transmission lines, but each was forced to use a different dielectric with different permittivity. For this reason, the substrate thicknesses were adjusted in order to achieve comparable performance at 2.4 GHz. We found that the microstrip patterns themselves did not require adjustment, only the thickness of the substrates.

When simulating the PCB microwave filters, copper with a sheet resistivity of ρ = 1.05 mΩ/sq/mil was used for the microstrip line and ground plane [44]. The substrate was FR4-Epoxy material, which has a permittivity of 4.35 at 2.5 GHz with a loss tangent of 0.018 [45]. The SMA connectors we installed on the PCB filters using standard silver solder. While the microstrip and ground of the 3D printed filters used conductive silver epoxy with a resistivity of ρ = 0.0004 cm·Ω/sq/mil. The microstrips were fabricated using DuPont's CB028 silver ink. This silver ink is mainly composed of nano and micro particle flakes that must come into intimate contact after curing in order to conduct. As a result, the resistivity of the silver ink (ρ = 10 mΩ/sq/mil) is considerably higher than pure copper [25]. The dielectric constant of the ABS was measured using a Damaskos split-cavity resonator and VNA to be 2.5 with a loss tangent of 0.005. We used optical epoxy (EPO-TEK 353ND) to fix the standard SMA connectors on the plastic part

of the substrates of the 3D printed filters to avoid connector breaks. In our simulations, wave ports were used to launch signals into the SMA connectors. Figure 4.1 shows the simulation model for the low pass filter. We included all the features needed to manufacture and measure our 3D printed and PCB filters into the simulation. We simulated the S_{11} and S_{21} parameters using ANSYS® HFSS software and compared them to the measurement results later on the testing section.

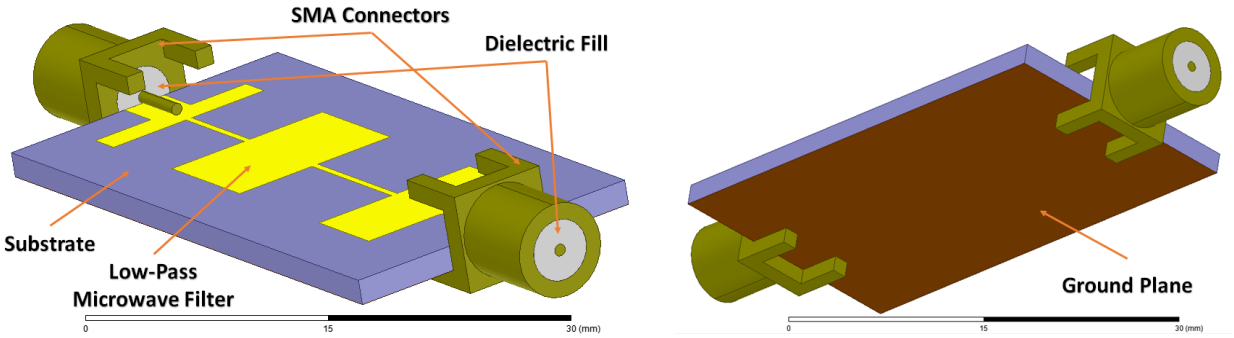

Figure 4.1: ANSYS simulation model for the low-pass filter

4.1 BANDPASS FILTER

The parallel coupled-line filter works by the frequency selectivity of directional coupling. It was found though simulation sweeps the impact of filter performance is negligible if features deviate less than 10 microns between the spacing of the microstrip lines [44]. Coupling was designed for microstrip lines separated 432 µm. Each line has a thickness of 25 µm thickness. The complete dimensions of the filter are shown in Figure 4.2. The filter was designed to operate at 2.4 GHz and provide a passband with fractional bandwidth of 10%. Thickness of the PCB substrate was 1.6 mm. SMA connectors were soldered onto the PCB boards using a lead-free silver solder compound. The 3DP filter used silver ink as the conductor and ABS thermoplastic as the dielectric substrate. The ABS had a different dielectric constant than the FR4. In order to get equivalent performance with as few changes as possible, the substrate thickness of the 3DP device was made 1.54 mm to maintain consistent line impedance. The only dimensional difference between the PCB and 3DP designs was the thickness of the substrate.

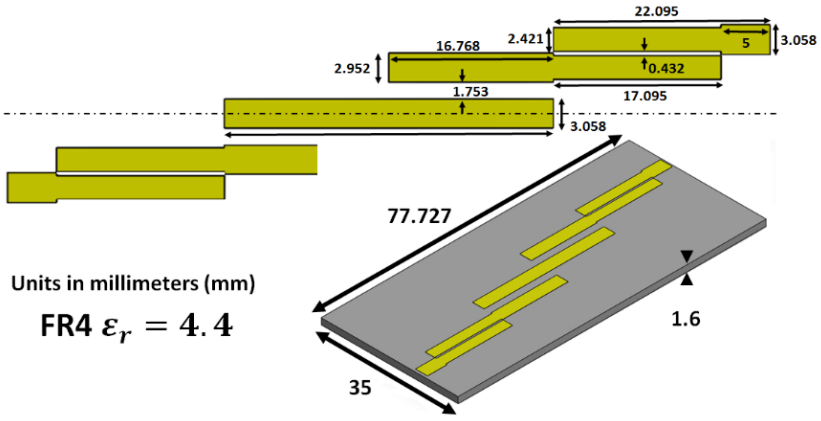

Figure 4.2: PCB design of the bandpass filter

4.2 LOW PASS FILTER

A low pass filter is designed that attenuates signals above its cutoff frequency of 2.4 GHz [44]. Figure 4.3 shows the design of the low pass filter as well as its dimensions. The features in this filter were easier to manufacture by 3D printing because the geometry had no breaks and no closely spaced lines. Still, the 3DP challenge is to achieve similar dimension features that deviate less than 12 μm as found in simulation sweeps for performance to be maintained. The same substrate thicknesses of 1.54 mm was used for the stepped-impedance filter. That was the only dimensional difference between the PCB and 3DP design.

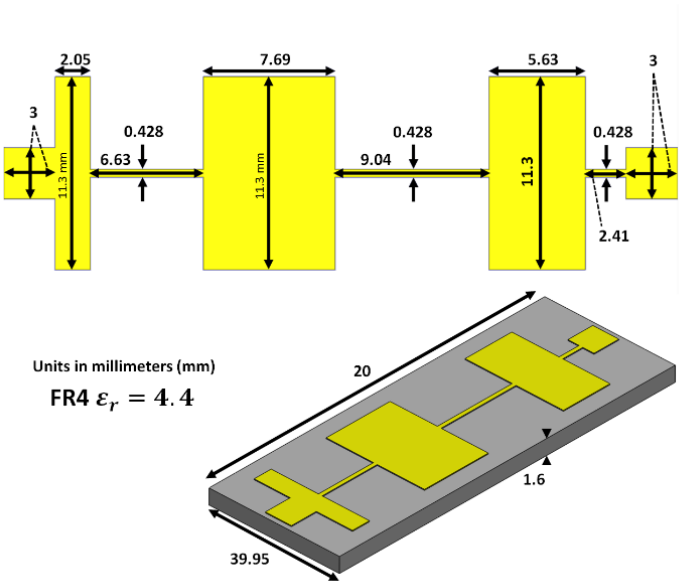

Figure 4.3: Filter design for the low pass filter

4.3 MANUFACTURING

To manufacture the 3D printed versions of the filters, an nScrypt Tabletop series 3D printer was used, a hybrid 3D printer that is capable of depositing filaments via FFF and depositing pastes via microdispensing [13]. For microdispensing the silver conductive ink, we used nScrypt's second-generation SmartPump™ 100 system and the ABS dielectric was deposited using nScrypt's nFD™ pump. In addition, there was a need to cure the silver ink with heat at 90℃ using a heat blower.

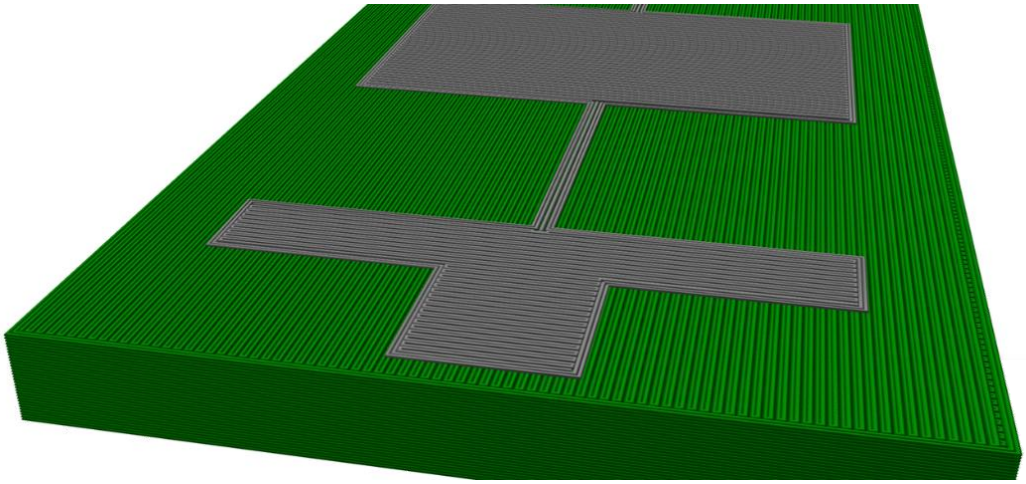

Figure 4.4: Tool path for 3D printed bandpass filter

Different software tools were used in order to process our design files for the 3D printed filters. First, Solidworks was used to design the geometry of the filters. We then divided the design into separate STL files for the dielectrics and conductors. These STL file for the dielectric portion was processed using Slic3r, a free software tool that generates g-code from the STL file to drive the 3D printer [46]. Figure 4.4 shows the write path for 3DP. The STL file for the conductor portion was processes using an nScrypt proprietary software called PCAD that creates dispensing lines for the SmartPump™ system [47]. Last, both file processes are interpreted into a single g-code file by the nScrypt Tabletop printer. The g-code file controls the microdispensing and fuse deposition pumps of the printer creating our filters. Table 4.1 summarizes the optimized process parameters for producing high-quality devices.

Table 4.1: Printing Parameters

	nTips	Dispense gap	Print ratio	Print speed
SmartPump™	100 µm	45 µm	1.06	60 mm/s
nFD ™	150 µm	110 µm	0.98	20 mm/s

There is a relation between the viscosity of the ink, velocity of the pen tip, and dispense rate that affects the build [31]. We adjusted the speeds to dispense the material with as close to zero momentum as possible. These adjustments were necessary to avoid printing mistakes, gaps between printed lines on our surfaces, and more importantly create continuous layers that ink would leak through. It took 1 hour 28 minutes to build the low pass filter, and 3 hours 6 minutes to build the bandpass filter since it is twice as large as the low pass filter. Figure 4.5 shows the finished PCB and 3D printed filters.

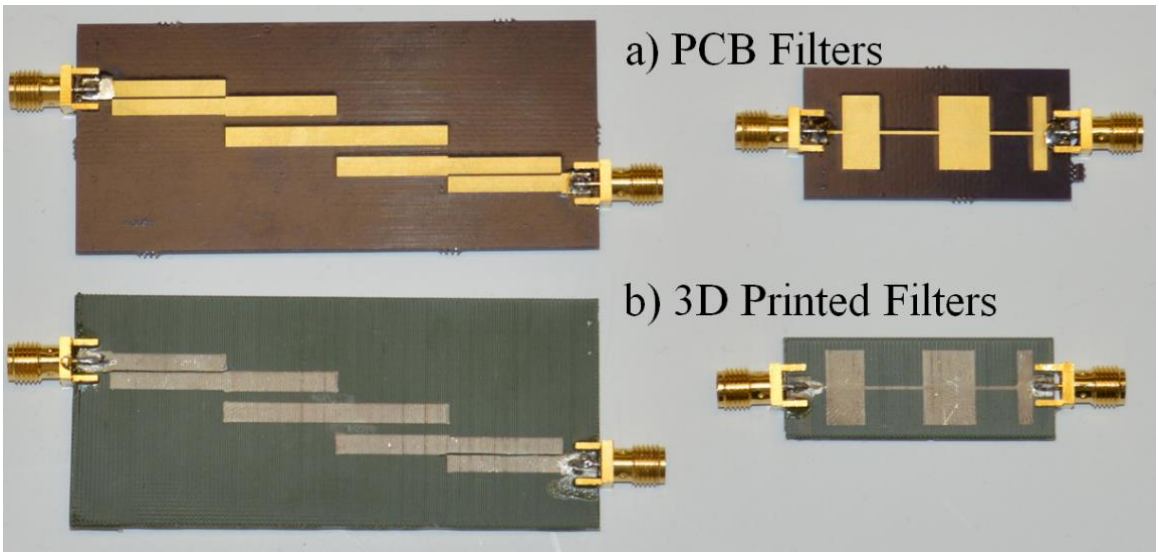

Figure 4.5: (a) PCB in contrast with (b) 3D Printed filters

4.4 TESTING

Overall, the test results show a slight frequency shift between the two different manufacturing methods. An Agilent N5245A PNA-X VNA with a 1601-point sweep from 1 GHz to 4 GHz was used to measure all microwave filters [29]. The VNA was calibrated by the use of an Ecal module that takes into

account the cables, SMA connectors, and the adaptors needed to launch the signal. The top graphs on Figure 4.6 show the band-pass filter results. The bottom part of the figure shows the results for the low-pass filter. The results for the filters are measured by the VNA and matched to their simulation. Part a) shows a similar response with a slight frequency shift to the left for the band-pass filter between simulated and measured results. The measured S_{21} in parts a) and c) contain standing waves and noise before and after the target frequency due to the SMA to microstrip transition. Part d) displays the simulated S_{11} curve lies around 2 dB under the measured S_{11}, indicating higher reflections from the PCB device. We noticed through simulation that the filters were mainly sensitive to the difference in filter microstrip dimensions and substrate thickness. A slight frequency shift was observed that we attributed to surface roughness, lower conductivity on the microstrip, and the increase in effective dielectric constant. These results are constant with 3DP antenna array results tested at 2.45 GHz previously published by T. P. Ketterl, et al [13]. Part d) in Figure 4.6 shows the measured filter exhibiting a 5 dB lower S_{11} than the simulated device, indicated that it outperformed our simulated device.

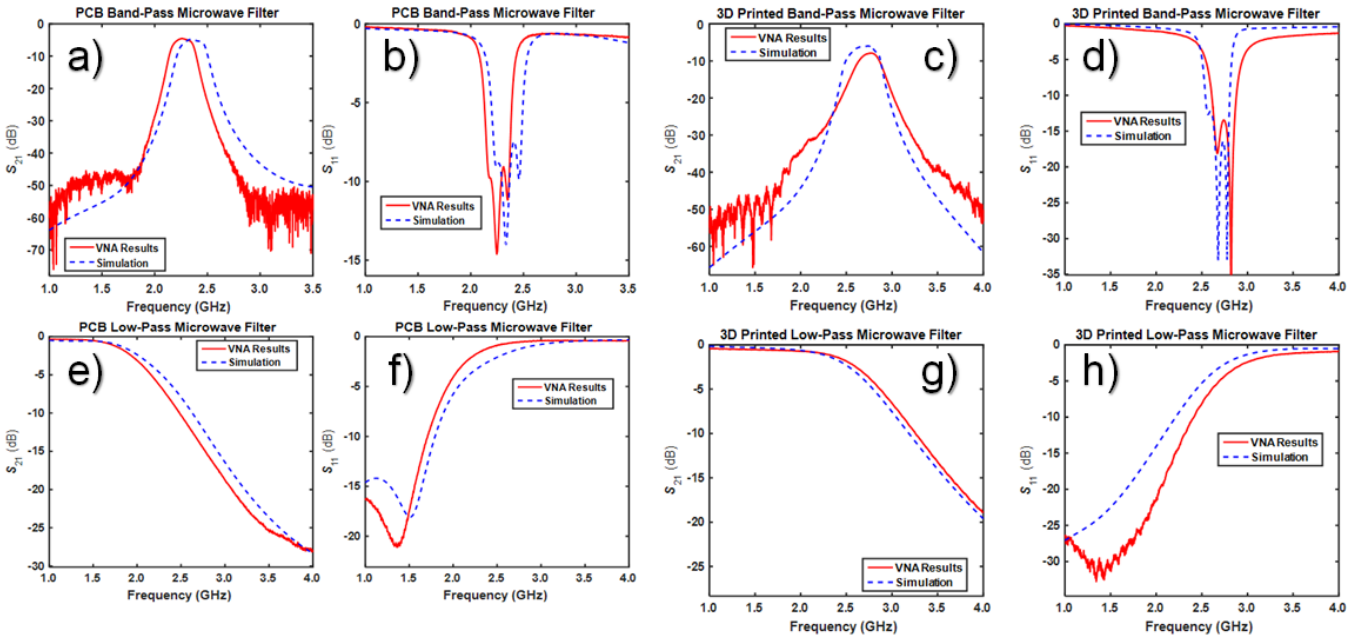

Figure 4.6: (Left) Results between manufactured PCB filters and their simulations. (Right). Results between 3D Printed filters and their simulations

4.5 DISCUSSION

Several factors contributed to the discrepancies between the performance of the PCB and 3DP filters. These factors include the conductivity of CB028 and the surface roughness of the 3D printed substrate. The temperature at which the silver paste is cured affects the conductivity of CB028 considerably. Thus, temperature needs to be controlled around the printing volume envelope to maintain precise control of conductivity. nFD produces relatively rough surfaces that in combination with microdispensed conductive pastes creates a rough path for high frequency signals [13]. There is also a need for methodologies that adjust the printing process while printing since the inks can change consistency throughout the process. We found that the lower permittivity of the ABS plastic lead to designs utilizing a thinner substrate. Considering that 3D printing can produce structures with part air, we think 3D printing 3D printing can produce circuits that are smaller, lighter, and use less material to manufacture. This could have significant impact in volume manufacturing. We found it helpful to use thin paint films like polyurethane or epoxy to protect the printed conductors from oxidation. We also found it useful to incorporate features in the substrate that provide mechanical support for SMA connectors. There is a need to develop materials with lower loss, higher conductivity, and that are able to create smoother surfaces as they are 3D printed. Figure 4.7 summarizes the key differences between manufactured filters for this discussion.

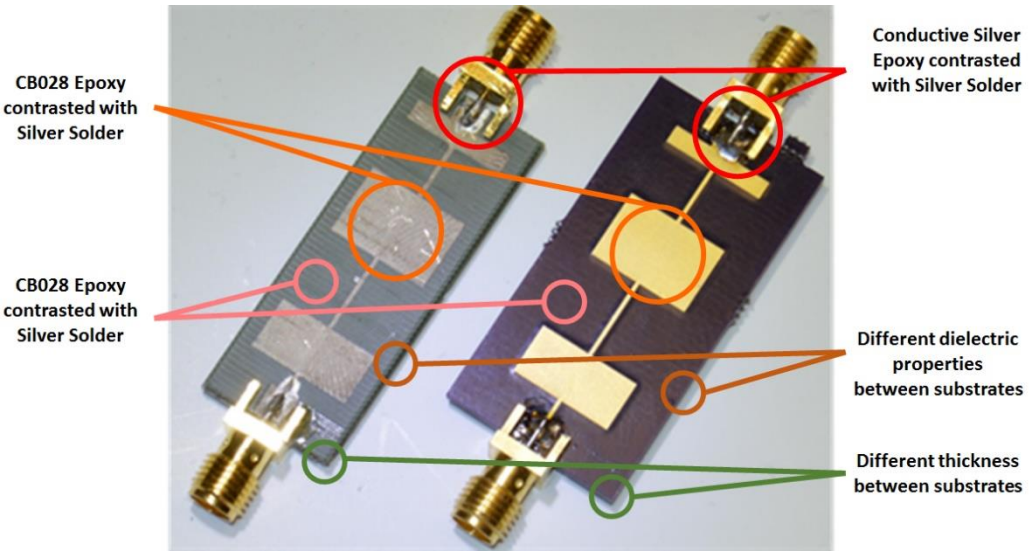

Figure 4.7: Points of comparisons between devices produced by different manufacturing processes

4.6 CONCLUSION

The goal of this filter research was to compare hybrid 3D printed high-frequency devices to conventional PCB devices in order to test the feasibility of producing more complex devices and systems. To do this, we designed two simple RF filters and manufactured each using both standard PCB technology and 3DP. Our 3D printed devices were manufactured using a hybrid 3D printer from nScrypt that combined nScrypt's microdispensing of conductive inks and fused deposition of dielectric substrates.

When comparing the PCB to the 3DP devices, we observed only small differences in performance between these devices. The most significant difference in transmission was 5 dB between 3DP and simulated Band Pass filters. This was due to the surface roughness effects that are not accounted for in the simulation. With further refinement in our 3D printing techniques, we conclude that direct-write 3D printing is a viable form of manufacturing for RF devices.

The goal of this research was to evaluate 3D printed high-frequency devices in order to identify the feasibility of producing more complex devices and systems. To do this, we designed two simple RF filters and manufactured each using both standard PCB technology and 3DP. Our 3D printed devices were manufactured using a hybrid 3D printer from nScrypt that combined nScrypt's microdispensing of conductive inks and fused deposition of dielectric substrates.

When comparing the PCB to the 3DP devices, we observed only small differences in performance between these devices. The most significant was around a 5 dB difference in transmission due to the effects of surface roughness. With further refinement in our 3D printing techniques, we conclude that direct-write 3D printing is a viable form of manufacturing for RF devices.

Chapter 5: Automated Hybrid 3DP Process of Meandering Interconnects

To demonstrate our process flow with a complicated 3D shape, an electrical trace was designed to meander in the shape of a pretzel. The geometry was generated using the open-source software Blender. While the pretzel shape was chosen for fun, it is representative of how interconnects may look in 3D circuits. Figure 5.1 shows the design realized in this research. Observe that the vertical meandering of the pretzel has been exaggerated in order to make it more 3D and a better exercise and demonstration of our process flow.

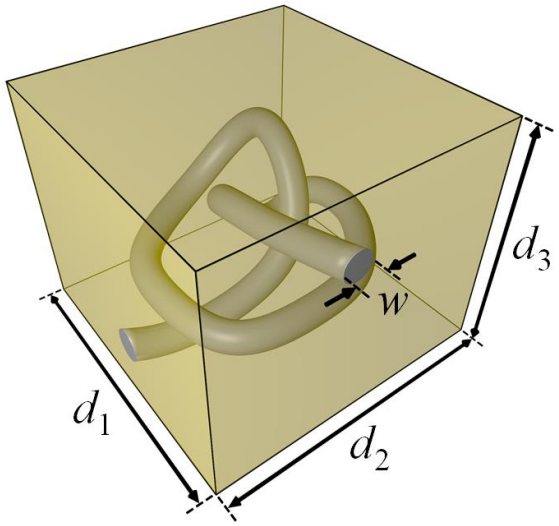

Figure 5.1: 3D design of a meandering electrical trace. Dimension are $d_1 = d_2 = d_3 =$ 1.0 cm and $w =$ 1.0 mm.

5.1 HYBRID SLICING

Two stereolighography (STL) files are generated where one represented the dielectric and the other the metal. These were generated so that no gaps or overlaps existed between the objects. These STL files were processed using Slic3r, an open-source software tool that generates g-code from STL files to drive a 3D printer [46]. Repetier-Host was used to load the files and call Slic3r to generate the g-code [48]. The process starts by loading the STL files into Repetier-Host and generating the g-code with two paths, both intended for FFF. In a later step, the g-code for one of the filament paths is converted to g-code that drives a micro-dispenser in an nScrypt hybrid direct-write 3D printer. One of the main problems of hybrid 3DP is combining different physics in a single process. Current slicing software can generate g-code for multi-

filament FFF, but the physics and g-code syntax is the same for all paths. This means the metal path of the pretzel line is initially generated with FFF build parameters. The present algorithm removes the FFF specific actions and inserts micro-dispensing actions for the metal path. The plastic path remains unchanged. Figure 5.2 shows a cross section of the sliced pretzel line.

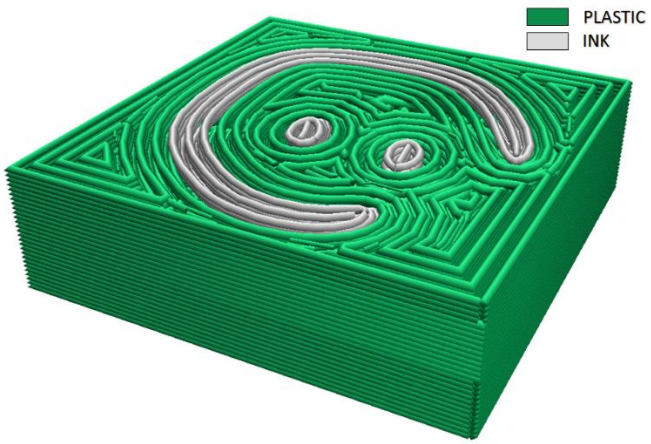

Figure 5.2: Cross sectional view of the dual-filament slicing of the pretzel line.

5.2 FILE PROCESSING

Our algorithm, shown in Figure 5.3, consists of three steps that converts Slic3r multi-material g-code into the language used by the nScrypt 3D printer. Step 1 reads the dual-filament g-code files along with header and closer files that initialize and close out the nScrypt 3D printer. Step 2 separates the individual tool paths and redefines one of them to be for micro-dispensing. FFF specific actions for this toolpath are removed and rewritten with micro-dispensing actions needed to control the nScrypt's SmartPump™ tool for micro-dispensing ink [22]. Finally, step three collects all of the changes and saves it as a text file with the instructions specific to the MPG Aerotech® A3200 Motion Composer Suite "pgm" file that drives our nScrypt Table Top machine [49].

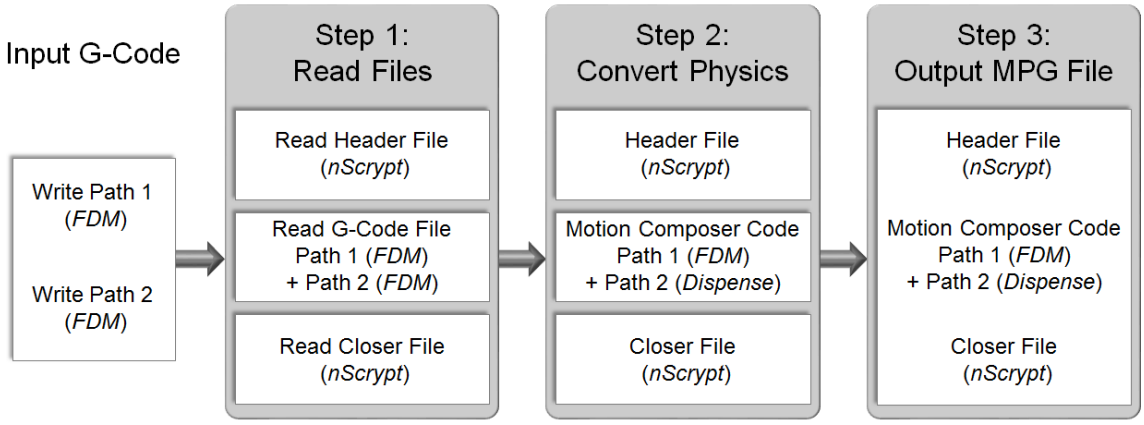

Figure 5.3: Hybrid pgm file generation tool

The first part of our software reads three files into memory, a header file that initializes all the fields needed to start the process of 3DP, a g-code file that contains the dual-filament printing sequence, and a closer file that has the closing commands for resetting the nScrypt machine for the next print job. It loads all three of these as text files. As the g-code is being read, it is parsed and saved in a structure in MATLAB so that it can be more easily manipulated. The header and closer files are stored as a simple sequence of text lines. Oversimplifying our algorithm, it proceeds one line of g-code at a time and converts it to pgm-code used by the nScrypt. Table 5.1 summarizes how the commands are translated.

Table 5.1: 3DP commands between g-code and pgm-code

Function	**g-code**	**pgm-code**
Motion x, y, z	G1	G1
Tool selection	T0, T1	A,B
Speed	F	F
Comments	;	//
Units	mm/min	mm/sec
Extrusion	T0 and E	B
Micro-dispensing	T1 and E	MOVE ABS A

Several g-code M and S commands are ignored because they are not needed in pgm-code like the fan speed, temperature setting, printing origin, and many others. At the start of our program, settings are defined for initializing the nScrypt machine such as the printing height floor value, values for closing and opening valves, travel speeds, and offset distance values between the Smart Pump™ and the nFD™ pump. Unfortunately, the conversion is not as simple as a one-to-one conversion of g-code to pgm-code. There are several places that look-ahead functions were needed to extract values, commands, and functions and used them to calculate new values for pgm-code. The first look-ahead scans the g-code to find the first G1 command that sets the *z* height. This is used to initialize the *z* height at the start of the pgm-code. As the g-code is scanned, T0 and T1 commands set which filament is being deposited. These correspond to the Smart Pump™ and nFD™ pump in the pgm-code. Here, additional pgm-code is inserted to handle switching between the pumps. This entails closing the previous pump, initializing the new pump, and offsetting the position between the pumps. It was necessary to look-ahead to identify stop-start printing on the same layer and insert pgm-code to raise the height of the pump during the non-printing movements in order to avoid collision with previously dispensed structures. Another look-ahead was needed to identify ramp-down for the filament path corresponding to the micro-dispenser. The g-code ramp-down was removed and replaced in the pgm-code with the ramp down specific to the nScrypt for micro-dispensing. If a G command is read, the g-code E extrusion command is converted to pgm B command for extruding nFD™ and an A command for changing the valve value to open or close dispensing accordingly. A unit conversion for the F command was necessary that takes the feed rate from Slic3r in mm/min and coverts it to mm/sec for the pgm-code. After all these steps, the algorithm converts the new set of commands to lines of text and then adds the header and closer text files to the beginning and end, respectively. This is saved as a single pgm file.

5.3 MANUFACTURING

To manufacture the pretzel line, we used an nScrypt Tabletop series 3D printer. This is a hybrid 3D printer capable of depositing plastic via FFF and depositing conductive inks via micro-dispensing. For micro-dispensing the conductive ink the SmartPump™ 100 system and the nScrypt's nFD™ pump dispensed the plastic. The pretzel line was made from silver ink (DuPont CB028) and its support plastic was ABS. Table 5.2 summarizes our printing parameters for the pretzel line.

Table 5.2: Printing parameters

	nTips	Dispense gap	Print ratio	Print speed
SmartPump™	360 µm	45 µm	1.06	60 mm/s
nFD™	370 µm	110 µm	0.98	20 mm/s

The process parameters were optimized so that long prints could be done without having to interrupt the process. This helped the repeatability of the prints to stay consistent. Initially, we experimented with different layer thicknesses and observed how the thickness affected the formation of ink making contact between layers. Ideally, layers with thickness of 25 µm are preferable, but the limit for us was 50 µm. Voids were intentionally left in the plastic regions to go back and fill with dispensed ink late. The plastic voids were set to 500 µm in cross section to be able to hold a uniform amount of ink. It was ensured that there was no conductive ink creeping between the printed ABS layers because this could cause short circuits or break the interconnect itself. We observed that thinner ink layers were more conductive, likely due to being better cured. We observed that our multi-material 3D printer required an extra 20 seconds of layer transition time between ink and plastic to allow enough time for in-site thermal curing. We found the heat produced by the printer was sufficient for curing the inks and no extra steps with lasers or heat lamps was needed.

Figure 5.4 shows a progression of samples that were manufactured for building electrical traces, which cross-different vertical layers. In part (a) of the figure, a single conductive line was sandwiched between two layers of ABS. In part (b), a second conductive line was added to the top layer to form a trace

that stepped one layer up and then stepped one layer down. Conductivity was measured between the two lines to ensure they were not shorted. The processes in part (b) was repeated in part (c), but the nozzle sizes for both ink and plastic were matched to make thinner layers with our algorithm. This helped the interconnects to be consistent through multiple layers. Finally, in part (d) an extra layer of plastic was added onto the top of the part with a window in the middle to inspect the printed line.

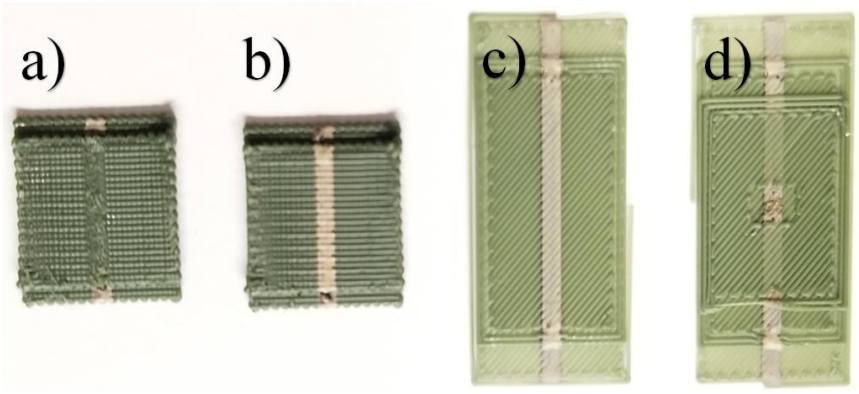

Figure 5.4: Progression of multi-layer prints.

As the printing parameters were optimized, a strong need was observed to keep the printing tools and area very clean though the whole process. The pen tips accumulate excess material that can be dropped on the part creating electrical continuity problems. Figure 5.5 shows a 3DP pretzel line imbedded in plastic.

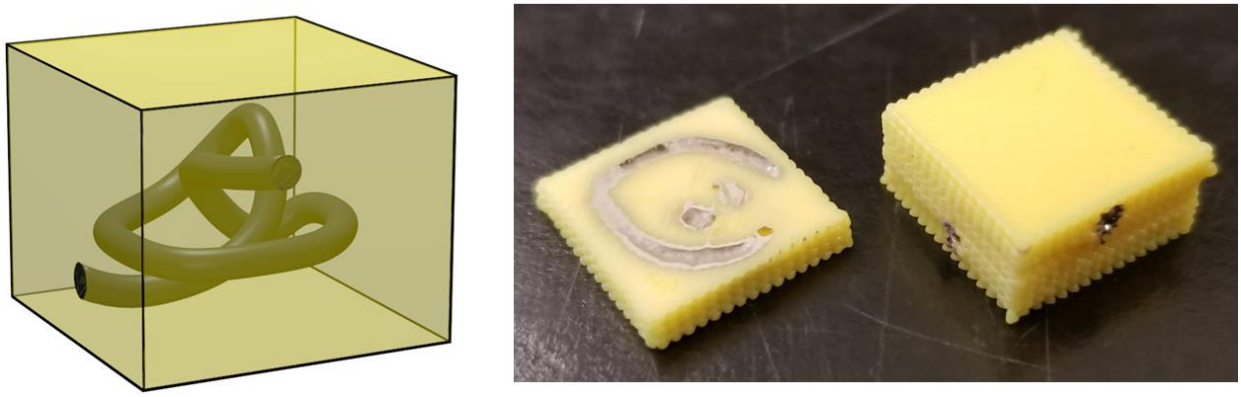

Figure 5.5: 3DP pretzel line using hybrid slicing tool. (Left) the CAD design for the pretzel. (Right) Hybrid 3DP partial build and full build.

5.4 TESTING

As the pretzel line was printed, results of 0.5 Ω resistance over the total length of 23 mm of line was measured. It took 1 hour and 28 minutes to execute the print job. Table 6.3 presents the final measurements for the 3D printed pretzel line using the hybrid 3D printing tool.

Table 5.3: Detailed results for the 3D printed pretzel line

Parameters	**Measured values**
Resistance	0.463 Ω
Length of line	23 mm
Printing time	1 hour 28 min
Layer count	19 layers
Total number of lines	5576
Filament extruded	292 mm
Ink dispensed	3.6 cu. mm

After printing an initial batch of pretzel lines, problems of inconsistent ink dispensing were observed that resulted in continuity breaks. The Army Research Lab (ARL) utilized x-ray micro computed tomography (micro-CT), measured via a Zeiss Xradia 520 micro-CT system, to detect ink continuity and porosity [50]. The sample was observed to have ink present throughout the length of the channel. Porosity was observed to be sufficient to make reliable electrical connections, but a few discontinuities were identified. Figure 5.6 shows the micro-CT ink pretzel on the left and the porosity and continuity readings on the right. The results suggest that the pen tip sizes should be reduced from 300 μm to 150 μm, or perhaps even 75 μm, to increase the resolution of the prints and solve the porosity and discontinuity problems observed in micro-CT.

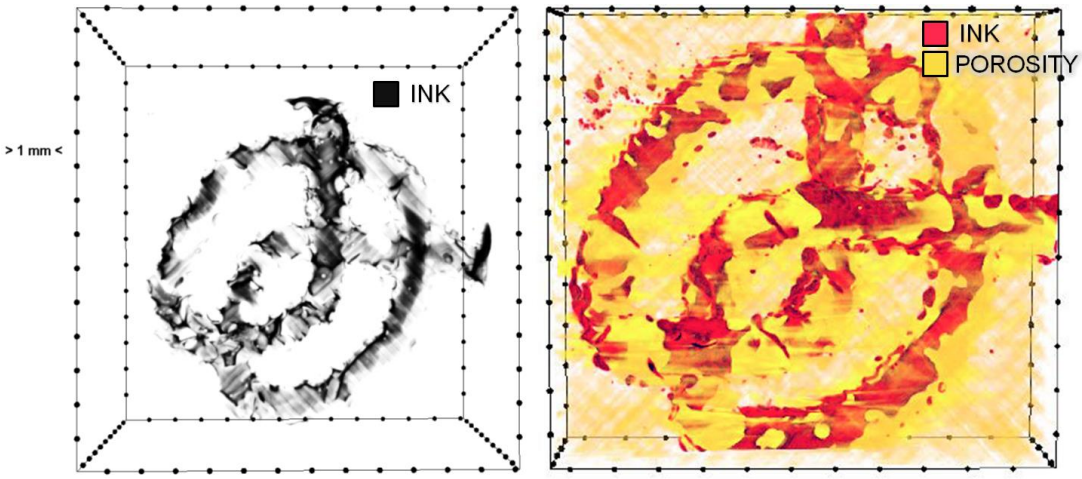

Figure 5.6: Micro-CT imaging from pretzel line. (Left) Metal layers of the line. (Right) Ink versus porosity.

5.5 DISCUSSION

Current slicing algorithms are not designed for multi-material devices in the same process. Despite the present work demonstrating a fully automated CAD-to-print process flow, there is a strong need to for improved slicing algorithms that are better suited for generating g-code that handles different types of materials and different printer tools in one print job. For more complicated circuits, we foresee long build times due to switching between tools and allowing for curing time. Better path planning and alternative methods of curing will shorten the build time considerably. We also see a need to maintain cleanliness of the print heads throughout the print if more materials and processes are added. One solution is to add cleaning tools for the printing nozzles. As the print progresses for several hours, the material residue can be periodically cleaned between layers to avoid adding material residue. Another solution is to add brims around the printed device so the printer has a chance of purging the nozzles as it dispenses materials outside the part. This also helps to push excess materials off the nozzles on the brims. However, it is not ensured that the excess material will fall on the brim lines. While some manufactured samples were not electrically conductive due to breaks in the line, others exhibited a total resistance of around 0.5 Ω. There is a need for improving the conductive materials in viscosity, density, and conductivity because the silver ink used in this work clogs the pen tips with diameters less than 75 μm. It will be very useful if the silver

particles inside the conductive ink are spherical and range in sizes between 50 nm to 1 μm. This will make the ink more fluid, as the particle shape will keep the clogging down, and the printing features can go even smaller. However, there are conductivity problems with spherical particles. Adding a post curing process with lasers or heaters might mitigate the conductivity problem.

5.6 FURTHER CIRCUIT WORK

After this research effort, the Electromagnetics Lab at the University of Texas at El Paso further improved this research by producing the first ever completely automated CAD-to-print process flow for hybrid direct-write 3DP [18]. We demonstrated a reliable automated process that requires no human intervention or manual coding of process steps. The process was demonstrated by manufacturing a device with an electrical trace meandering throughout three dimensions in the shape of a pretzel. Furthermore, this research enabled the realization of more geometrically complex 3D circuits like those that our 3D meandering timer circuit is shown in Figure 5.7. The device features a cube as a substrate with each of the components are positioned on each of the faces. Then, the team shifted the location of the electronics and the shape of the ABS plastic to display the capabilities of exploiting the third dimension. The entire model was designed as a timer based on the schematic of a 555-circuit design using the 3D Circuit Layout Tool and manufacturing it using our process described in previous sections. Each of the connecting traces were modeled to highlight the meandering nature of the lines and the feasibility of connecting components in any orientation. Then, the layout files were put through the slicing process already explained to obtained tool paths for 3D printing. Our fabricated 555-timer circuit is also demonstrated in Figure 6.7. The substrate dimensions for the square circuit are 13.36 mm × 14.89 mm × 8.88 mm. The power lines were connected to a nine-volt source to demonstrate the circuit functions properly. We used the following surface-mount components: NE555DR integrated circuit, 100 kΩ resistor, 51 kΩ resistor, 1 kΩ resistor, 1 μF capacitor, and an APD3224SURCK-F01 red LED. To secure the components to the device, we used EPOTEK H20 conductive epoxy.

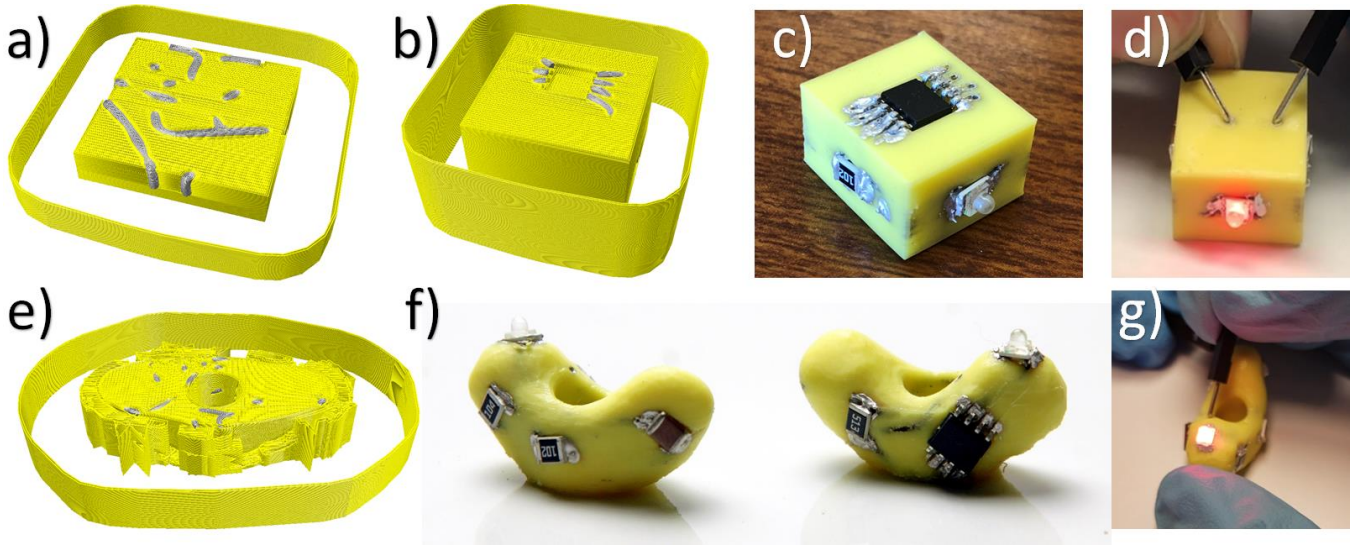

Figure 5.7: Sliced 3D 555-timer block circuit at (a) initial layer #26 and final (b) layer #280. Part (c) shows the 3DP model with electronic components and it is demonstrated in part d). The Holey Frijole mid slicing layer is shown in part e). Part f) displays the printed amorphous device, while part g) demonstrates it working.

During this particularly 555-timer circuit-working period, we were able to successfully print another working iteration of the circuit using the same tools and processes. The first version of the circuit work flawlessly, however, we felt that the block shape might mislead the circuit geometry was planar and not meandering. Then, we further tested the limits of our process by designing a second casing in the shape of a bean (frijole) with a hole in it, so we nicknamed the device "Holey Frijole." This new design implies that: (1) the circuit components can truly be placed in any non-orthogonal orientation, (2) the lines must truly be meandering in any formation, and (3) amorphous packaging shapes can be manufactured. The lower part of Figure 6.7 shows the sliced model after using the 3D Circuit Design Tool, two fabricated devices, and shows the working device. One major difference between the Frijole and the previous device is the use of support material. In the original 3D 555-timer circuit, support material was not needed because the print was structurally self-supported on its own. The Frijole on the other hand is not due to the steepness of the overhanging layers near the base. In the end, adding the support material increased the time by 75 minutes.

Chapter 6: Finite-Difference Analysis of Transmission Lines

Transmission lines are waveguides. Not all waveguides are transmission lines because not all can work down to DC. Transmission lines are usually used at the fundamental transverse electromagnetic (TEM) mode. The field inside a TL obeys Maxwell's equations. TLs work by confining energy in one or two transverse directions to guide the waves. Some of the characteristics of TLs are that they contain two or more conductors and have no low frequency cutoff. TLs are considered compact for low frequency signals and tend to be lossy at very high frequencies (>10 GHz) due to skin effects and dielectric loss.

Understanding PPTLs begins by deriving field solutions using Maxwell's equations. Once the static models are satisfactory, a more rigorous solution will come from ANSYS HFSS simulation package for different TL bends [28]. The methods used will build confidence on manufacturing and testing the 3D printed devices later on.

6.1 Analysis of Parallel Plate Transmission Lines

Analysis starts with Maxwell's equations. In this case, a static analysis was used to calculate the properties of the PPTLs. First, the TL is drawn to understand the analysis of the electromagnetic structure. Figure 6.1 shows the physical features of a PPTL where, w is the width of the plates, d is the distance between them, μ and ε correspond to the permeability and permittivity of the material. The geometry of the PPTL confines fields by containing most of the energy between the plates. The next steps is to manipulate the equations to find a governing equation, solve the equation in each homogeneous region, calculate the field solution, and find the TL parameters.

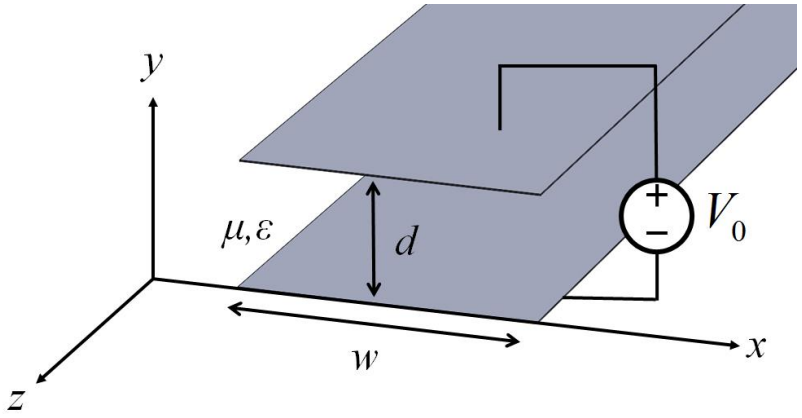

Figure 6.1: Geometry of a PPTL with a voltage across the plates.

6.1.1 Start with Maxwell's Equations

Let us start by introducing Maxwell's Equations in differential form in the frequency-domain.

$$\begin{aligned} \nabla \times \vec{E} &= -j\omega\vec{B} \\ \nabla \times \vec{B} &= \vec{J} + j\omega\vec{D} \\ \nabla \bullet \vec{D} &= \rho_v \\ \nabla \bullet \vec{B} &= 0 \end{aligned} \tag{0.13}$$

The constitutive relations in equations (0.14) describe the interaction of fields with materials. The permittivity ε is a measure of how well a medium stores electric energy and quantifies how much the electric fields will interact with the medium. The permeability μ is a measure of how well a medium stores magnetic energy and quantifies how much the magnetic fields will interact with the medium. The permittivity and/or permeability may be scalar quantifies for isotropic materials or tensors for anisotropic materials. The PPTLs in the present research are made exclusively from linear, homogeneous, and isotropic (LHI) materials. However, 3DP introduces a weak anisotropy as the material lines are dispensed and small air gaps are left and was ignored.

$$\begin{aligned} \vec{D} &= [\varepsilon]\vec{E} \\ \vec{B} &= [\mu]\vec{H} \end{aligned} \tag{0.14}$$

First, we assume there are no charges or current sources. This will make $\rho_v = 0$ and $\vec{J} = 0$. After substituting in the constitutive relations, we arrive at the following equations.

$$\begin{aligned} \nabla \times \vec{E} &= -j\omega\mu\vec{H} \\ \nabla \times \vec{H} &= j\omega\varepsilon\vec{E} \\ \nabla \bullet \vec{D} &= 0 \\ \nabla \bullet \vec{B} &= 0 \end{aligned} \tag{0.15}$$

6.1.2 Wave Equation

For convenience, the curl equations in equation (0.15) are repeated below. These new equations describe how electric fields induce magnetic fields and how magnetic fields induce electric fields.

$$\nabla \times \vec{E} = -j\omega\mu\vec{H} \tag{0.16}$$

$$\nabla \times \vec{H} = j\omega\varepsilon\vec{E} \tag{0.17}$$

In these equations ω is the angular frequency. The ordinary frequency *f* is measured in cycles per second and is related through $\omega = 2\pi f$. The wave equation for the electric field is derived by solving equation (0.16) for the electric field and substituting that result into equation (0.17) to eliminate the magnetic field.

$$\begin{aligned}
&\left.\begin{aligned}\nabla \times \vec{E} &= -j\omega\mu\vec{H}\\ \nabla \times \vec{H} &= j\omega\varepsilon\vec{E}\end{aligned}\right\} \rightarrow \text{Solve for } \vec{H} \rightarrow \vec{H} = \frac{1}{-j\omega\mu}\nabla \times \vec{E}\\
&\nabla \times \left(\frac{1}{-j\omega\mu}\nabla \times \vec{E}\right) = j\omega\varepsilon\vec{E} \rightarrow \frac{1}{-j\omega}\nabla \times \left(\frac{1}{\mu}\nabla \times \vec{E}\right) = j\omega\varepsilon\vec{E}\\
&\nabla \times \left(\frac{1}{\mu}\nabla \times \vec{E}\right) = (-j\omega)\, j\omega\varepsilon\vec{E}\\
&\nabla \times \left(\mu^{-1}\nabla \times \vec{E}\right) = \omega^2\varepsilon\vec{E}
\end{aligned} \tag{0.18}$$

$$\nabla \times \mu^{-1}\nabla \times \vec{E} = \omega^2\varepsilon\vec{E} \tag{0.19}$$

Similarly, an analogous wave equation for the magnetic field is derived by solving equation (0.17) for the magnetic field and substituting that result into equation (0.16) to eliminate the electric field.

$$\nabla \times \varepsilon^{-1}\nabla \times \vec{H} = \omega^2\mu\vec{H} \tag{0.20}$$

Assuming the materials are LHI, the wave equations simplify considerably. Since the materials are isotropic, μ and ε become constants. Then, the permeability μ can be moved to the right hand side of the equation. The general vector identity for the double curl operation $\nabla \times \nabla \times \vec{E}$ needs to applied as the gradient of a divergence minus a vector Laplacian as shown in equation (0.21) .

$$\nabla \times \nabla \times \vec{E} = \nabla\left(\nabla \bullet \vec{E}\right)^2 - \nabla^2 \vec{E} \tag{0.21}$$

In LHI media, the divergence equation can be explain in terms of the electric field and becomes zero as the homogeneous medium sets permittivity to be a constant.

$$\begin{aligned} \nabla \bullet \vec{D} &= \nabla \bullet \left(\varepsilon \vec{E}\right) = 0 \\ \nabla \bullet \vec{E} &= 0 \end{aligned} \tag{0.22}$$

Equation (0.24) is the LHI case of the wave equation.

$$\begin{aligned} \nabla \times \mu^{-1} \nabla \times \vec{E} &= \omega^2 \varepsilon \vec{E} \\ \nabla \times \nabla \times \vec{E} &= \omega^2 \mu \varepsilon \vec{E} \\ \cancel{\nabla\left(\nabla \bullet \vec{E}\right)^2} - \nabla^2 \vec{E} &= \omega^2 \mu \varepsilon \vec{E} \end{aligned} \tag{0.23}$$

$$\nabla^2 \vec{E} + \omega^2 \mu \varepsilon \vec{E} = 0 \tag{0.24}$$

Historically, the wave equation has been known since at least the 1700's [20]. This was

$$\nabla^2 \psi + \left(\frac{\omega}{v}\right)^2 \psi = 0 \tag{0.25}$$

In this equation, v is the speed of the wave. Comparing equation (0.24) to equation (0.25) shows that the speed of an electromagnetic wave is

$$v = \frac{1}{\sqrt{\mu \varepsilon}} \tag{0.26}$$

The speed of light is dependent on the medium that the wave travels. In equation (0.27), the permittivity of free space is related to the relative permittivity by $\varepsilon = \varepsilon_0 \varepsilon_r$. Alternatively, the permittivity and permeability become $\mu = \mu_0$ and $\varepsilon = \varepsilon_0$ in a vacuum. The velocity becomes the speed of light as the wave moves in a vacuum.

$$v = \frac{1}{\sqrt{\mu\varepsilon}} = \frac{1}{\sqrt{\mu_0\mu_r\varepsilon_0\varepsilon_r}} = \frac{1}{\sqrt{\mu_0\varepsilon_0}}\frac{1}{\sqrt{\mu_r\varepsilon_r}} \tag{0.27}$$

$$c_0 = \frac{1}{\sqrt{\varepsilon_0\mu_0}} = \frac{1}{\sqrt{\left(8.85\times10^{-12}\ \mathrm{F/m}\right)\left(4\pi\times10^{-7}\ \mathrm{H/m}\right)}} = 299792458\ \mathrm{m/s} \tag{0.28}$$

To get the velocity of the wave we have that; $v = c_0/\sqrt{\varepsilon_r\mu_r}$ where $\sqrt{\varepsilon_r\mu_r}$ is the refractive index.

$$n = \sqrt{\varepsilon_r\mu_r} \tag{0.29}$$

The wave number *k* relates to the angular frequency and the material properties by $k = \omega\sqrt{\mu\varepsilon}$, which reduces the equation (0.24) to the following form.

$$\nabla^2\vec{E} + k^2\vec{E} = 0 \tag{0.30}$$

Now, we can expand the curl equations (0.16) in six coupled partial differential equations.

$$\begin{aligned}
\frac{\partial E_z}{\partial y} - \frac{\partial E_y}{\partial z} &= -j\omega\mu H_x & \frac{\partial H_z}{\partial y} - \frac{\partial H_y}{\partial z} &= j\omega\varepsilon E_x \\
\frac{\partial E_x}{\partial z} - \frac{\partial E_z}{\partial x} &= -j\omega\mu H_y & \frac{\partial H_x}{\partial z} - \frac{\partial H_z}{\partial x} &= j\omega\varepsilon E_y \\
\frac{\partial E_y}{\partial x} - \frac{\partial E_x}{\partial y} &= -j\omega\mu H_z & \frac{\partial H_y}{\partial x} - \frac{\partial H_x}{\partial y} &= j\omega\varepsilon E_z
\end{aligned} \tag{0.31}$$

The general form for a mode solution comes by analyzing the cross section in an *x*-*y* plane. This is $\vec{E}(x,y,z) = \vec{E}_0(x,y)e^{-j\beta z}$, where the phase is constant is β. For a mode propagating uniform in the *z* direction, the solution takes the form.

$$\begin{aligned}
\vec{E}(x,y,z) &= \vec{E}_0(x,y)e^{-j\beta z} \\
\vec{H}(x,y,z) &= \vec{H}_0(x,y)e^{-j\beta z}
\end{aligned} \tag{0.32}$$

Substituting the solution into the six partial differential equations yields the following set of equations.

$$\frac{\partial E_{0,z}}{\partial y}+j\beta E_{0,y}=-j\omega\mu H_{0,x} \quad \text{eq.(a)} \qquad \frac{\partial H_{0,z}}{\partial y}+j\beta H_{0,y}=j\omega\varepsilon E_{0,x} \quad \text{eq.(d)}$$

$$-j\beta E_{0,x}-\frac{\partial E_{0,z}}{\partial x}=-j\omega\mu H_{0,y} \quad \text{eq.(b)} \qquad -j\beta H_{0,x}-\frac{\partial H_{0,z}}{\partial x}=j\omega\varepsilon E_{0,y} \quad \text{eq.(e)} \qquad (0.33)$$

$$\frac{\partial E_{0,y}}{\partial x}-\frac{\partial E_{0,x}}{\partial y}=-j\omega\mu H_{0,z} \quad \text{eq.(c)} \qquad \frac{\partial H_{0,y}}{\partial x}-\frac{\partial H_{0,x}}{\partial y}=j\omega\varepsilon E_{0,z} \quad \text{eq.(f)}$$

The equations are ready to be solved for the cross section of the mode in *x*-*y* plane. Take Eq. (2.18e) from the previous set of equations and solve for $E_{0,y}$.

$$E_{0,y}=\frac{1}{j\omega\varepsilon}\left(-j\beta H_{0,x}-\frac{\partial H_{0,z}}{\partial x}\right) \qquad (0.34)$$

Eliminate the term $E_{0,y}$ by substituting equation (0.34) into eq. (2.18a). Solve the expression for $H_{0,x}$. Recall that $k^2=\omega^2\mu\varepsilon$.

$$\frac{\partial E_{0,z}}{\partial y}+j\beta\left[\frac{1}{j\omega\varepsilon}\left(-j\beta H_{0,x}-\frac{\partial H_{0,z}}{\partial x}\right)\right]=-j\omega\mu H_{0,x}$$

$$H_{0,x}=\frac{j}{k^2-\beta^2}\left(\omega\varepsilon\frac{\partial E_{0,z}}{\partial y}-\beta\frac{\partial H_{0,z}}{\partial x}\right) \qquad (0.35)$$

The term $H_{0,x}$ is expressed in terms of the longitudinal components across the *z*-direction. If the following equations are derived in a similar way, all the transverse field components can be expressed in terms of just the longitudinal components.

$$H_{0,x}=\frac{j}{k^2-\beta^2}\left(\omega\varepsilon\frac{\partial E_{0,z}}{\partial y}-\beta\frac{\partial H_{0,z}}{\partial x}\right) \qquad E_{0,x}=-\frac{j}{k^2-\beta^2}\left(\beta\frac{\partial E_{0,z}}{\partial x}+\omega\mu\frac{\partial H_{0,z}}{\partial y}\right)$$

$$H_{0,y}=-\frac{j}{k^2-\beta^2}\left(\omega\varepsilon\frac{\partial E_{0,z}}{\partial x}+\beta\frac{\partial H_{0,z}}{\partial y}\right) \qquad E_{0,y}=\frac{j}{k^2-\beta^2}\left(-\beta\frac{\partial E_{0,z}}{\partial y}+\omega\mu\frac{\partial H_{0,z}}{\partial x}\right) \qquad (0.36)$$

First, define the cutoff wave number k_c as $k_c=k^2-\beta^2$. Then the transverse components can be reduced by substituting k_c into equations (0.36)

$$H_{0,x} = \frac{j}{k_c^2}\left(\omega\varepsilon\frac{\partial E_{0,z}}{\partial y} - \beta\frac{\partial H_{0,z}}{\partial x}\right) \qquad E_{0,x} = -\frac{j}{k_c^2}\left(\beta\frac{\partial E_{0,z}}{\partial x} + \omega\mu\frac{\partial H_{0,z}}{\partial y}\right)$$
$$H_{0,y} = -\frac{j}{k_c^2}\left(\omega\varepsilon\frac{\partial E_{0,z}}{\partial x} + \beta\frac{\partial H_{0,z}}{\partial y}\right) \qquad E_{0,y} = \frac{j}{k_c^2}\left(-\beta\frac{\partial E_{0,z}}{\partial y} + \omega\mu\frac{\partial H_{0,z}}{\partial x}\right) \tag{0.37}$$

All there is to determine are the terms $E_{0,z}$ and $H_{0,z}$ to find the remaining filed components. When the transmission line has a homogeneous dielectric fill, the differential equations for E0z and H0z are decoupled and can be solved independently.

If $E_{0,z} = H_{0,z} = 0$, the transverse electromagnetic (TEM) solution is obtained because all of the field components are transverse of the direction of the propagation. This analysis is reduced to an electrostatic problem. However, the nature of the wave needs to be accounted for by incorporating the term that accumulates phase in the z direction. If $E_{0,z} = 0$ but $H_{0,z} \neq 0$, the transverse electric (TE) solution is obtained because the electric field has no longitudinal component. If $E_{0,z} \neq 0$ but $H_{0,z} = 0$, the transverse magnetic (TM) solution is obtained because the magnetic field has no longitudinal component. This explains the origins of the TEM, TE, and TM modes for PPTLs.

6.1.3 Nature of the Wave

The solution to the wave equation in LHI is complex exponentials. Complex exponentials can only oscillate, decay, or both so it can be concluded that waves can only oscillate, decay, or both.

$$\vec{E}\left(\vec{r},t\right) = \vec{P}\cos\left(\omega t - \vec{k}\cdot\vec{r}\right)$$
$$\vec{r} \equiv \text{ vector position } \left(x\hat{a}_x + y\hat{a}_y + z\hat{a}_z\right)$$
$$t \equiv \text{ time}$$
$$\omega \equiv \text{ angular frequency}$$
$$\vec{k} \equiv \text{ wave vector}$$
$$\vec{P} \equiv \text{ polarization vector} \tag{0.38}$$

Recall that the angular frequency is related to the ordinary frequency through,

$$\omega = 2\pi f \tag{0.39}$$

The wave vector $\vec{k}$ defines the direction of the wave and conveys the wavelength of the wave

$$\begin{aligned} \left|\vec{k}\right| &= \frac{2\pi}{\lambda} \\ \lambda &= \frac{\lambda_0}{n} \end{aligned} \tag{0.40}$$

When the frequency is known then $\vec{k}$ conveys the refractive index

$$\begin{aligned} \left|\vec{k}\right| &= k_0 n \\ k_o &= \frac{2\pi}{\lambda_0} = \frac{\omega}{c_0} \end{aligned} \tag{0.41}$$

6.1.4 PPTL TE Analysis

For TE waves, recall $E_{0,z} = 0$ and $H_{0,z} \neq 0$. Under this condition, the curl equations (0.33) are reduced by dropping the $E_{0,z}$ terms that are equal to zero and keeping the $H_{0,z}$ terms.

$$\begin{aligned} \cancel{\nabla^2 E_{0,z} + k^2 E_{0,z} = 0} \\ \nabla^2 H_{0,z} + k^2 H_{0,z} = 0 \end{aligned} \tag{0.42}$$

This solution takes all boundaries to be tangential in the TL. The other field components from equation (0.37) are calculated from $H_{0,z}$.

$$\begin{aligned} H_{0,x} &= -\frac{j\beta}{k_c^2}\frac{\partial H_{0,z}}{\partial x} & E_{0,x} &= -\frac{j\omega\mu}{k_c^2}\frac{\partial H_{0,z}}{\partial y} \\ H_{0,y} &= -\frac{j\beta}{k_c^2}\frac{\partial H_{0,z}}{\partial y} & E_{0,y} &= \frac{j\omega\mu}{k_c^2}\frac{\partial H_{0,z}}{\partial x} \end{aligned} \tag{0.43}$$

After reducing the equations, the impedance Z_{TE} can be calculated. However, the phase must be determined by solving the wave equation.

$$Z_{\mathrm{TE}} = \frac{E_{0,x}}{H_{0,y}} = \frac{-\frac{j\omega\mu}{k_c^2}\frac{\partial H_{0,z}}{\partial y}}{-\frac{j\beta}{k_c^2}\frac{\partial H_{0,z}}{\partial y}} = \frac{\omega\mu}{\beta} = \eta\frac{k}{\beta} \tag{0.44}$$

The general solution to the governing equation is reduced since the TL is uniform in the *x*-direction.

$$0 + \frac{\partial^2 H_{0,z}}{\partial y^2} - k_c^2 H_{0,z} = 0 \;\rightarrow\; \frac{\partial^2 H_{0,z}}{\partial y^2} - k_c^2 H_{0,z} = 0 \;\rightarrow\; H_{0,z} = A\sin\left(k_c y\right) + B\cos\left(k_c y\right) \tag{0.45}$$

The boundary conditions for the fields must be zero at the plates. The solution has to be in terms of the magnetic field. Thus, the only component of the electric field tangential to the interface is $E_{0,x}$.

$$\begin{aligned} E_{0,x} &= -\frac{j\omega\mu}{k_c^2}\frac{\partial H_{0,z}}{\partial y} = -\frac{j\omega\mu}{k_c^2}\frac{\partial\left[\, A\sin\left(k_c y\right) + B\cos\left(k_c y\right) \,\right]}{\partial y} \\ &= -\frac{j\omega\mu}{k_c^2}\left[\, A\sin\left(k_c y\right) + B\cos\left(k_c y\right) \,\right] \end{aligned} \tag{0.46}$$

To calculate the first boundary condition the term needs to be equal to zero and the governing equation solved for *A*.

$$\begin{aligned} &E_{0,x}\left(x,0\right) = 0 \\ &E_{0,x}\left(x,0\right) = -\frac{j\omega\mu}{k_c}\left[\, A\cos\left(0\right) + B\sin\left(0\right) \,\right] = -\frac{j\omega\mu}{k_c}A = 0 \\ &A = 0 \end{aligned} \tag{0.47}$$

The second boundary condition is set at the distance *d* and the governing equation solved for *B*.

$$\begin{aligned} &E_{0,x}\left(x,d\right) = 0 \\ &E_{0,x}\left(x,d\right) = -\frac{j\omega\mu}{k_c}\left[\, -B\sin\left(k_c d\right) \,\right] = B\frac{j\omega\mu}{k_c}\sin\left(k_c d\right) \end{aligned} \tag{0.48}$$

Notice how the sine term can be zero at $y = d$ but not at $B = 0$, this will lead to a trivial solution.

$$\sin\left(k_c d\right) = 0 \;\rightarrow\; k_c d = n\pi \quad n = 1, 2, 3, \ldots \tag{0.49}$$

The cutoff wave number is when the following happens in equation (0.50). Beware that if $n=0$ the entire field will be zero.

$$k_c = \frac{n\pi}{d} \qquad n = 1, 2, 3, \ldots \tag{0.50}$$

Recall the definition of the cutoff wave number from equation (0.71) . Solve this for β .

$$\beta = \sqrt{k^2 - k_c^2} \tag{0.51}$$

Now substitute the previously derived expression from equation (0.50) that was produced from the boundary conditions and substitute it into equation (0.51).

$$\beta = \sqrt{k^2 - \left(\frac{n\pi}{d}\right)^2} \qquad n = 1, 2, 3, \ldots \tag{0.52}$$

There are an infinite number of discrete solutions where the order of the mode is *n*. Now, the final solution can be calculated as a result from the general solution, but now we understand that $A=0$ and $k_c = n\pi / d$.

$$H_{0,z}(x,y) = B_n \cos\left(\frac{n\pi y}{d}\right) \;\rightarrow\; H_z(x,y,z) = B_n \cos\left(\frac{n\pi y}{d}\right) e^{-j\beta_n z} \tag{0.53}$$

Therefore, the field components can be calculated from this result based on equation (0.53).

$$\begin{aligned}
H_x &= -\frac{j\beta}{k_c^2}\frac{\partial H_{0,z}}{\partial x} = -\frac{j\beta}{k_c^2}\frac{\partial}{\partial x}\left[B_n \cos\left(\frac{n\pi y}{d}\right) e^{-j\beta_n z}\right] = 0 \\
H_y &= -\frac{j\beta}{k_c^2}\frac{\partial H_{0,z}}{\partial y} = -\frac{j\beta}{k_c^2}\frac{\partial}{\partial y}\left[B_n \cos\left(\frac{n\pi y}{d}\right) e^{-j\beta_n z}\right] = -\frac{j\beta}{k_c} B_n \sin\left(\frac{n\pi y}{d}\right) e^{-j\beta_n z} \\
E_x &= -\frac{j\omega\mu}{k_c^2}\frac{\partial}{\partial y}\left[B_n \cos\left(\frac{n\pi y}{d}\right) e^{-j\beta_n z}\right] = -\frac{j\omega\mu}{k_c} B_n \sin\left(\frac{n\pi y}{d}\right) e^{-j\beta_n z} \\
E_y &= \frac{j\omega\mu}{k_c^2}\frac{\partial}{\partial x}\left[B_n \cos\left(\frac{n\pi y}{d}\right) e^{-j\beta_n z}\right] = 0 \\
E_z &= 0
\end{aligned} \tag{0.54}$$

The cutoff conditions for the modes come from the phase constant in equation (0.52). If $k_c > k$ then this becomes imaginary. The values of *n* that cause this condition correspond to the modes that are

"cutoff". These modes are still functional but they decay very quickly so they are rarely used. The cutoff frequency for the TM ode can be calculated as follows.

$$\begin{aligned} k_c &= \omega_c\sqrt{\mu\varepsilon} = \frac{n\pi}{d} \\ 2\pi f_c\sqrt{\mu\varepsilon} &= \frac{n\pi}{d} \\ f_c &= \frac{n}{2d\sqrt{\mu\varepsilon}} = \frac{k_c}{2\pi\sqrt{\mu\varepsilon}} \end{aligned} \tag{0.55}$$

6.1.5 PPTL TM Analysis

For TM waves, recall $E_{0,z} \neq 0$ and $H_{0,z} = 0$. Under this condition, the curl equations (0.33) are reduced by dropping the $H_{0,z}$ terms that are equal to zero and keeping the $E_{0,z}$ terms.

$$\begin{aligned} &\nabla^2 E_{0,z} + k^2 E_{0,z} = 0 \\ &\cancel{\nabla^2 H_{0,z} + k^2 H_{0,z} = 0} \end{aligned} \tag{0.56}$$

This solution takes all boundaries to be tangential in the TL. The other field components from equation (0.37) are calculated from $E_{0,z}$.

$$\begin{aligned} H_{0,x} &= \frac{j\omega\varepsilon}{k_c^2}\frac{\partial E_{0,z}}{\partial y} & E_{0,x} &= -\frac{j\beta}{k_c^2}\frac{\partial E_{0,z}}{\partial x} \\ H_{0,y} &= -\frac{j\omega\varepsilon}{k_c^2}\frac{\partial E_{0,z}}{\partial x} & E_{0,y} &= -\frac{j\beta}{k_c^2}\frac{\partial E_{0,z}}{\partial y} \end{aligned} \tag{0.57}$$

After reducing the equations, the impedance Z_{TM} can be calculated. However, the phase must be determined by solving the wave equation.

$$Z_{\mathrm{TM}} = \frac{E_{0,x}}{H_{0,y}} = \frac{-\frac{j\beta}{k_c^2}\frac{\partial E_{0,z}}{\partial x}}{-\frac{j\omega\varepsilon}{k_c^2}\frac{\partial E_{0,z}}{\partial x}} = \frac{\beta}{\omega\mu} = \eta\frac{\beta}{k} \tag{0.58}$$

The general solution to the governing equation is reduced since the TL is uniform in the *x*-direction.

$$\frac{\partial^2 E_{0,z}}{\partial y^2} - k_c^2 E_{0,z} = 0 \;\rightarrow\; E_{0,z} = A\sin\left(k_c y\right) + B\cos\left(k_c y\right) \tag{0.59}$$

The boundary conditions for the fields must be defined to be $0 \le x \le d$ at the plates. The solution has to be in terms of the electric field. Thus, the only component of the magnetic field tangential to the interface is $E_{0,z}$. Thus, the first boundary condition is solved in equation (0.60) by substituting $x = 0$ and solving for B.

$$E_{0,z}\left(x,0\right) = A\cos\left(0\right) + B\sin\left(0\right) \;= B = 0 \tag{0.60}$$

To calculate the second boundary condition the term needs to be equal to zero and the governing equation solved for A over the distance d.

$$E_{0,z}\left(x,d\right) = -A\sin\left(k_c d\right) = 0 \tag{0.61}$$

Notice how the sine term can be zero at $y = d$ but not at $A = 0$, this will lead to a trivial solution.

$$\sin\left(k_c d\right) = 0 \;\rightarrow\; k_c d = n\pi \quad n = 1,2,3,\ldots \tag{0.62}$$

The cutoff wave number is when anything but zero happens in equation (0.62). Beware that if $n = 0$ the entire field will be zero.

$$k_c = \frac{n\pi}{d} \quad n = 1,2,3,\ldots \tag{0.63}$$

Recall the definition of the cutoff wave number from equation (0.71) . Solve this for β .

$$\beta = \sqrt{k^2 - k_c^2} \tag{0.64}$$

Now substitute the previously derived expression from equation (0.63) that was produced from the boundary conditions and substitute it into equation (0.64).

$$\beta = \sqrt{k^2 - \left(\frac{n\pi}{d}\right)^2} \quad n = 1,2,3,\ldots \tag{0.65}$$

There are an infinite number of discrete solutions where the order of the mode is *n*. Now, the final solution can be calculated as a result from the general solution, but now is understood that $B=0$ and $k_c = n\pi / d$.

$$E_{0,z}(x,y) = A_n \sin\left(\frac{n\pi y}{d}\right) \rightarrow \mathrm{E}_z(x,y,z) = A_n \sin\left(\frac{n\pi y}{d}\right) e^{-j\beta_n z} \tag{0.66}$$

Therefore, the field components can be calculated from this result based on equation (0.53).

$$\begin{aligned}
H_x &= -\frac{j\omega\varepsilon}{k_c^2}\frac{\partial E_z}{\partial y} = -\frac{j\omega\varepsilon}{k_c^2}\frac{\partial}{\partial y}\left[A_n \sin\left(\frac{n\pi y}{d}\right) e^{-j\beta_n z}\right] = \frac{j\omega\varepsilon}{k_c} A_n \cos\left(\frac{n\pi y}{d}\right) e^{-j\beta_n z} \\
H_y &= -\frac{j\omega\varepsilon}{k_c^2}\frac{\partial E_z}{\partial x} = -\frac{j\omega\varepsilon}{k_c^2}\frac{\partial}{\partial x}\left[A_n \sin\left(\frac{n\pi y}{d}\right) e^{-j\beta_n z}\right] = 0 \\
H_z &= 0 \\
E_x &= -\frac{j\beta}{k_c^2}\frac{\partial}{\partial y}\left[A_n \sin\left(\frac{n\pi y}{d}\right) e^{-j\beta_n z}\right] = 0 \\
E_y &= \frac{j\beta}{k_c^2}\frac{\partial}{\partial x}\left[A_n \sin\left(\frac{n\pi y}{d}\right) e^{-j\beta_n z}\right] = \frac{j\beta}{k_c} A_n \cos\left(\frac{n\pi y}{d}\right) e^{-j\beta_n z}
\end{aligned} \tag{0.67}$$

The cutoff conditions for the modes come from the phase constant in equation (0.65). If $k_c > k$ then this becomes imaginary. The values of *n* that cause this condition correspond to the modes that are "cutoff". These modes are still functional but they decay very quickly so they are rarely used. The cutoff frequency for the TM mode can be calculated as follows.

$$\begin{aligned}
k_c &= \omega_c \sqrt{\mu\varepsilon} = \frac{n\pi}{d} \\
2\pi f_c \sqrt{\mu\varepsilon} &= \frac{n\pi}{d} \\
f_c &= \frac{n}{2d\sqrt{\mu\varepsilon}} = \frac{k_c}{2\pi\sqrt{\mu\varepsilon}}
\end{aligned} \tag{0.68}$$

6.1.4 PPTL TEM Analysis

If $E_{0,z} = H_{0,z} = 0$ all the field components are transverse to the direction of propagation. This is the TM solution at $n = 0$, otherwise called the TEM mode solution, and its analysis reduces to an electrostatics

problem. Under this condition, the curl equations (0.33) are reduced by dropping the terms that are equal to zero.

$$\begin{aligned}
\cancel{\frac{\partial E_{0,z}}{\partial y}} + j\beta E_{0,y} &= -j\omega\mu H_{0,x} & \cancel{\frac{\partial H_{0,z}}{\partial y}} + j\beta H_{0,y} &= j\omega\varepsilon E_{0,x} \\
-j\beta E_{0,x} - \cancel{\frac{\partial E_{0,z}}{\partial x}} &= -j\omega\mu H_{0,y} & -j\beta H_{0,x} - \cancel{\frac{\partial H_{0,z}}{\partial x}} &= j\omega\varepsilon E_{0,y} \\
\frac{\partial E_{0,y}}{\partial x} - \frac{\partial E_{0,x}}{\partial y} &= \cancel{-j\omega\mu H_{0,z}} & \frac{\partial H_{0,y}}{\partial x} - \frac{\partial H_{0,x}}{\partial y} &= \cancel{j\omega\varepsilon E_{0,z}}
\end{aligned} \tag{0.69}$$

Here is the reduced form of the equations for the TEM case.

$$\begin{aligned}
j\beta E_{0,y} &= -j\omega\mu H_{0,x} & j\beta H_{0,y} &= j\omega\varepsilon E_{0,x} \\
-j\beta E_{0,x} &= -j\omega\mu H_{0,y} & -j\beta H_{0,x} &= j\omega\varepsilon E_{0,y} \\
\frac{\partial E_{0,y}}{\partial x} - \frac{\partial E_{0,x}}{\partial y} &= 0 & \frac{\partial H_{0,y}}{\partial x} - \frac{\partial H_{0,x}}{\partial y} &= 0
\end{aligned} \tag{0.70}$$

After reducing the equations, $H_{0,y}$ can be substituted into $-j\beta E_{0,x} = -j\omega\varepsilon H_{0,y}$ to solve for β.

$$\begin{aligned}
j\beta H_{0,y} &= j\omega\varepsilon E_{0,x} \\
H_{0,y} &= \frac{\omega\varepsilon}{\beta} E_{0,x}
\end{aligned}$$

$$\begin{aligned}
-j\beta E_{0,x} &= -j\omega\mu H_{0,y} \\
-j\beta E_{0,x} &= -j\omega\mu\left(\frac{\omega\varepsilon}{\beta} E_{0,x}\right) \\
\beta^2 E_{0,x} &= \omega^2\varepsilon\mu\left(E_{0,x}\right) \\
\beta^2 E_{0,x} &= k^2 E_{0,x} \\
\beta &= k
\end{aligned} \tag{0.71}$$

If β equals k, then the cutoff frequency k_c is zero. This implies there is no cutoff frequency for the TEM mode. Recall the wave equation in LHI media for the electric component from equation (0.24). For the TEM mode, the second term is zero because there is no cutoff frequency. Then the wave equation reduces to Laplace's equation from electrostatics.

$$\begin{aligned} \nabla^2 E_{0,z} + k^2 E_{0,z} &= 0 \\ \nabla^2 E_{0,z} + \cancel{k^2 E_{0,z}} &= 0 \\ \nabla^2 E_{0,z} &= 0 \end{aligned} \tag{0.72}$$

Laplace's equation is a second-order partial differential equation.

$$\Delta^2 V(x,y,z) = \frac{\partial^2 V}{\partial x^2} + \frac{\partial^2 V}{\partial y^2} + \frac{\partial^2 V}{\partial z^2} = 0 \tag{0.73}$$

At the frontal cross section of the PPTL, the fields are uniform in the *z* and *x* directions. Since *y* is the only variable left, the derivative becomes ordinary.

$$\cancel{\frac{\partial^2 V}{\partial x^2}} + \frac{\partial^2 V}{\partial y^2} + \cancel{\frac{\partial^2 V}{\partial z^2}} = 0 \tag{0.74}$$

Our governing equation has a solution interpreted for the diagram in Figure 2.1, where the variable *y* goes over the distance between the two parallel plates. The final solution to the ordinary governing equation is shown in equation (0.75).

$$\frac{d^2 V}{dy^2} = 0 \tag{0.75}$$

The solution to this gives the electric potential across distance *y*.

$$\frac{d^2 V}{dy^2} = 0 \;\rightarrow\; \frac{dV}{dy} = A \;\rightarrow\; V(y) = Ay + B \tag{0.76}$$

If voltage V_0 is applied between the plates, the boundary conditions for the differential equation across the distance *y* are $0 \le y \le d$. If equation (0.76) is the general solution, then the boundary conditions set by the cross section of the TL geometry need to be applied to find the final solution of the governing equation.

$$V(y)=Ay+B \quad 0\le y\le d \;\rightarrow\; \begin{matrix} V(0)=A(0)+B=0 \\ V(d)=A(d)+B=V_0 \end{matrix} \;\rightarrow\; \begin{matrix} B=0 \\ A=\dfrac{V_0}{d} \end{matrix} \tag{0.77}$$

$$V(y)=\frac{V_0}{d}y \tag{0.78}$$

The electric field can be calculated from the electric potential.

$$\begin{aligned} \vec{E} &= -\Delta V-\hat{a}_x\frac{\partial V}{\partial x}-\hat{a}_y\frac{\partial V}{\partial y}-\hat{a}_z\frac{\partial V}{\partial z} \\ &= -\hat{a}_x\frac{\partial}{\partial x}\left(\frac{V_0}{d}y\right)-\hat{a}_y\frac{\partial}{\partial y}\left(\frac{V_0}{d}y\right)-\hat{a}_z\frac{\partial}{\partial z}\left(\frac{V_0}{d}y\right) \\ &= 0-\hat{a}_y\frac{\partial}{\partial y}\left(\frac{V_0}{d}y\right)-0 \\ &= -\hat{a}_y\frac{V_0}{d} \end{aligned} \tag{0.79}$$

$$\vec{E}=-\hat{a}_y\frac{V_0}{d} \tag{0.80}$$

To calculate the electric field between the plates $0\le y\le d$, one can take equation (0.80) and substitute it over the width and height of the PPTL. Recall the general form from the mode solution from equation (0.32) and substitute it into the field components. Since the answer only applies to the *y*-direction, the electric field is solved with the mode solution in one direction between the parallel plates.

$$\vec{E}(x,y,z)=\begin{cases} -\hat{a}_y\dfrac{V_0}{d}e^{-j\beta z} & \text{for } 0\le x\le w \text{ and } 0\le y\le d \\ 0 & \text{otherwise} \end{cases} \tag{0.81}$$

The TEM solution describes all of the field components to be transverse of the direction of the propagation. However, the nature of the wave in the mode needs to be accounted for by incorporating the term $e^{-j\beta z}$ that accumulates phase in the *z* direction. Now, to define the magnetic field, start from the curl equations in equation (0.16). The magnetic component for this particular TL is derived from the electric field. Where the TEM mode has no cutoff frequency ($\beta=k$ and $k_c=0$). The phase constant is represented by β and the impedance of the dielectric is represented by η.

$$\begin{aligned}\nabla\times\vec{E} &= -j\omega\mu\vec{H}\\ \nabla\times\vec{H} &= j\omega\varepsilon\vec{E}\end{aligned}\rightarrow \text{Solve for } \vec{H}\rightarrow \vec{H}=\frac{1}{-j\omega\mu}\nabla\times\vec{E}$$

$$\vec{H}(x,y,z)=\frac{1}{-j\omega\mu}\nabla\times\vec{E} \tag{0.82}$$

$$\vec{H}(x,y,z)=\frac{\hat{a}_z\times\vec{E}}{Z_{\text{TEM}}}=\frac{\hat{a}_z\times\left(-\hat{a}_y\frac{V_0}{d}e^{-j\beta z}\right)}{\eta}=-\left(\hat{a}_z\times\hat{a}_y\right)\frac{V_0}{\eta d}e^{-j\beta z}$$
$$=\hat{a}_x\frac{V_0}{\eta d}e^{-j\beta z}$$

To calculate the magnetic field between the plates, one can take equation (0.82) and apply it over the *xyz*-components over the width and height of the PPTL.

$$\vec{H}(x,y,z)=\begin{cases}\hat{a}_x\dfrac{V_0}{\eta d}e^{-j\beta z} & \text{for } 0\le x\le w \text{ and } 0\le y\le d\\ 0 & \text{otherwise}\end{cases} \tag{0.83}$$

The impedance Z_{TEM} experienced by the TEM wave is defined by the voltage V_0 and the current distributed at any point along the TL.

$$Z_{\text{TEM}}=\frac{V_0}{I} \tag{0.84}$$

The magnetic field can determine the current term *I.* Recall the magnetic field above one infinite current sheet.

$$\vec{H}=\frac{\vec{K}\times\hat{n}}{2} \qquad \begin{array}{c}\vec{K}\equiv \text{ surface current density (A/m)}\\ \hat{n}=-\hat{a}_y\end{array} \tag{0.85}$$

Then, since we have two plates going parallel to each other, the magnetic field equation is doubled.

$$\vec{H}=\vec{K}\times\hat{n} \tag{0.86}$$

Solving this equation for the surface current density term yields,

$$\vec{K} \times \hat{n} = \left(-\hat{a}_y\right) \times \vec{H} = \vec{H} \times \hat{a}_y \tag{0.87}$$

The total current I is found by integrating the surface current across a plate over the distance w of the plate.

$$I = \int_0^w \left(\vec{K} \bullet \hat{a}_z\right) dx = \int_0^w \left[\left(\vec{H} \times \hat{a}_y\right) \bullet \hat{a}_z\right] dx = \int_0^w H_x dx \tag{0.88}$$

Substituting the previous answer from the magnetic field across the plates produces a simpler integral.

$$I = \int_0^w \left(\frac{V_0}{\eta d}\right) dx = \frac{V_0}{\eta d} \int_0^w dx = \frac{V_0}{\eta d} w = \frac{w}{d} \frac{V_0}{\eta} \tag{0.89}$$

The characteristic impedance Z_{TEM} is found by substituting this into the original definition in equation (0.84).

$$\begin{aligned} Z_{\text{TEM}} &= \frac{V_0}{\left(\frac{w}{d} \frac{V_0}{\eta}\right)} = \eta \frac{d}{w} \\ Z_{\text{TEM}} &= \eta \frac{d}{w} \end{aligned} \tag{0.90}$$

An electrostatic approximation cannot calculate a propagation constant β_{TEM}. However, TEM waves propagate nearly the same speed as a plane wave in an infinite medium made from dielectric between the two plates [21].

$$\beta_{\text{TEM}} \cong w\sqrt{\mu\varepsilon} \tag{0.91}$$

Parallel plate TLs support TEM modes because they have two conductors, have a homogeneous medium, TE and TM modes are supported. The lowest order mode is the zero order mode, which is the

TEM mode. The distributed capacitance C can be estimated as $C = \varepsilon \frac{w}{d}$ and the distributed inductance L can be solved by using the characteristic impedance equation (0.90).

$$Z_{\text{TEM}} = \eta \frac{d}{w} = \sqrt{\frac{L}{C}} = \sqrt{\frac{L}{\varepsilon \frac{w}{d}}}$$

$$L = \frac{\varepsilon d \left(Z_{\text{TEM}}\right)^2}{w} = \frac{\varepsilon \left(\eta \frac{d}{w}\right)^2}{\frac{d}{w}} = \mu \frac{d}{w} \tag{0.92}$$

$$L = \mu \frac{d}{w}$$

This concludes the STATIC approach to PPTL analysis. This approach works for wide plates and it does not consider finding fields at the end of the plates. There is a need to move onto a finite differences analysis to add the effects of the fringing fields to the PPTL analysis. The plates envisioned in this research need to be narrower than capacitor plates or planar PPTLs since they are intended for meandering in arbitrary form factors.

6.2 FINITE DIFFERENCES FOR PPTL

A transmission line propagates an electromagnetic signal across the line. In this analysis, the fields extend over the plates of the PPTLs because it takes into account the distributed capacitance and inductance of the line across itself and over the edges. There is a specially interest on the characteristic impedance for matching the impedance of the lines to avoid reflections and scattering when the line is connected to a measurement rig or device. For this analysis, an electrostatic approximation is needed since it happens at DC (zero frequency). Transmission lines are small relative to the wavelength of the signal that the wave nature cannot manifest itself on the scale of the transmission line. Therefore, the derivative becomes zero at the time domain equations. For this analysis, the LHI case still applies. Recall the electrostatic equations from (0.14) and (2.3), where the divergence condition for the electric field is zero and the vector electric field is described by the negative scalar electric potential.

$$\begin{aligned}\vec{E} &= -\nabla V \\ \nabla \bullet \vec{D} &= 0 \\ \vec{D} &= [\varepsilon]\vec{E}\end{aligned} \tag{0.93}$$

The equations can be expanded into a matrix form. The constitutive relation can have its off-diagonal tensor terms set to zero since this is a LHI material.

$$\begin{aligned}\vec{E} = -\nabla V \rightarrow \begin{bmatrix} E_x \\ E_y \\ E_z \end{bmatrix} &= -\begin{bmatrix} \frac{\partial}{\partial x} \\ \frac{\partial}{\partial y} \\ \frac{\partial}{\partial z} \end{bmatrix} V \\ \nabla \bullet \vec{D} = 0 \rightarrow \begin{bmatrix} \frac{\partial}{\partial x} & \frac{\partial}{\partial y} & \frac{\partial}{\partial z} \end{bmatrix} \begin{bmatrix} D_x \\ D_y \\ D_z \end{bmatrix} &= 0 \\ \vec{D} = [\varepsilon]\vec{E} \rightarrow \begin{bmatrix} D_x \\ D_y \\ D_z \end{bmatrix} = \begin{bmatrix} \varepsilon_{xx} & 0 & 0 \\ 0 & \varepsilon_{yy} & 0 \\ 0 & 0 & \varepsilon_{zz} \end{bmatrix} &\begin{bmatrix} E_x \\ E_y \\ E_z \end{bmatrix} = 0\end{aligned} \tag{0.94}$$

PPTLs are uniform in the *z*-direction the wave propagates. Since nothing changes in that direction, it is assumed that the derivative of anything in that direction is zero. This reduces the equations to the *x* and *y* directions.

$$\begin{aligned}\vec{E} = -\nabla V \quad \rightarrow \quad \begin{bmatrix} E_x \\ E_y \\ E_z \end{bmatrix} &= -\begin{bmatrix} \frac{\partial}{\partial x} \\ \frac{\partial}{\partial y} \\ \frac{\partial}{\partial z} \end{bmatrix} V \qquad \rightarrow \begin{bmatrix} E_x \\ E_y \end{bmatrix} = -\begin{bmatrix} \frac{\partial}{\partial x} \\ \frac{\partial}{\partial y} \end{bmatrix} V \\ \nabla \bullet \vec{D} = 0 \quad \rightarrow \quad \begin{bmatrix} \frac{\partial}{\partial x} & \frac{\partial}{\partial y} & \frac{\partial}{\partial z} \end{bmatrix} \begin{bmatrix} D_x \\ D_y \\ D_z \end{bmatrix} &= 0 \qquad \rightarrow \begin{bmatrix} \frac{\partial}{\partial x} & \frac{\partial}{\partial y} \end{bmatrix} \begin{bmatrix} D_x \\ D_y \end{bmatrix} = 0 \\ \vec{D} = [\varepsilon]\vec{E} \quad \rightarrow \quad \begin{bmatrix} D_x \\ D_y \\ D_z \end{bmatrix} = \begin{bmatrix} \varepsilon_{xx} & 0 & 0 \\ 0 & \varepsilon_{yy} & 0 \\ 0 & 0 & \varepsilon_{zz} \end{bmatrix} &\begin{bmatrix} E_x \\ E_y \\ E_z \end{bmatrix} = 0 \quad \rightarrow \begin{bmatrix} D_x \\ D_y \end{bmatrix} = \begin{bmatrix} \varepsilon_{xx} & 0 & 0 \\ 0 & \varepsilon_{yy} & 0 \\ 0 & 0 & \varepsilon_{zz} \end{bmatrix} \begin{bmatrix} E_x \\ E_y \end{bmatrix} = 0\end{aligned} \tag{0.95}$$

These equations are the final governing equations. The next step is to approximate the governing equations using the Finite-Difference method. The matrix equations can be written in a block matrix form by identifying the five-coupled equations that are staggered across the grid. From the constitutive relations one can see that D_x and ε_{xx} lie at the same points as E_x. Similarly, D_y and ε_{yy} lie at the same points as E_y. Then the constitutive relations need no staggering. However, V needs to be staggered around E_x in the x direction and around E_y in the y direction.

$$\begin{bmatrix} E_x \\ E_y \end{bmatrix} = -\begin{bmatrix} \dfrac{\partial}{\partial x} \\ \dfrac{\partial}{\partial y} \end{bmatrix} V \quad \rightarrow \quad \begin{bmatrix} \mathbf{e}_x \\ \mathbf{e}_y \end{bmatrix} = -\begin{bmatrix} \mathbf{D}_x^v \\ \mathbf{D}_y^v \end{bmatrix} \mathbf{V}$$

$$\begin{bmatrix} \dfrac{\partial}{\partial x} & \dfrac{\partial}{\partial y} \end{bmatrix} \begin{bmatrix} D_x \\ D_y \end{bmatrix} = 0 \quad \rightarrow \begin{bmatrix} \mathbf{D}_x^e & \mathbf{D}_x^e \end{bmatrix} \begin{bmatrix} \mathbf{d}_x \\ \mathbf{d}_y \end{bmatrix} \mathbf{V} = 0 \tag{0.96}$$

$$\begin{bmatrix} D_x \\ D_y \end{bmatrix} = \begin{bmatrix} \varepsilon_{xx} & 0 & 0 \\ 0 & \varepsilon_{yy} & 0 \\ 0 & 0 & \varepsilon_{zz} \end{bmatrix} \begin{bmatrix} E_x \\ E_y \end{bmatrix} = 0 \quad \rightarrow \quad \begin{bmatrix} \mathbf{d}_x \\ \mathbf{d}_y \end{bmatrix} = \varepsilon_0 \begin{bmatrix} \varepsilon_{xx} & 0 \\ 0 & \varepsilon_{yy} \end{bmatrix} \begin{bmatrix} \mathbf{e}_x \\ \mathbf{e}_y \end{bmatrix}$$

The D field can be algebraically eliminated by substituting equations the following way,

$$\begin{bmatrix} \mathbf{d}_x \\ \mathbf{d}_y \end{bmatrix} = \varepsilon_0 \begin{bmatrix} \varepsilon_{xx} & 0 \\ 0 & \varepsilon_{yy} \end{bmatrix} \begin{bmatrix} \mathbf{e}_x \\ \mathbf{e}_y \end{bmatrix} \rightarrow \begin{bmatrix} \mathbf{D}_x^e & \mathbf{D}_x^e \end{bmatrix} \begin{bmatrix} \mathbf{d}_x \\ \mathbf{d}_y \end{bmatrix} \mathbf{V} = 0$$

$$\begin{bmatrix} \mathbf{D}_x^e & \mathbf{D}_x^e \end{bmatrix} \left(\varepsilon_0 \begin{bmatrix} \varepsilon_{xx} & 0 \\ 0 & \varepsilon_{yy} \end{bmatrix} \begin{bmatrix} \mathbf{e}_x \\ \mathbf{e}_y \end{bmatrix} \right) = 0 \tag{0.97}$$

$$\begin{bmatrix} \mathbf{D}_x^e & \mathbf{D}_x^e \end{bmatrix} \begin{bmatrix} \varepsilon_{xx} & 0 \\ 0 & \varepsilon_{yy} \end{bmatrix} \begin{bmatrix} \mathbf{e}_x \\ \mathbf{e}_y \end{bmatrix} = 0$$

The E field can be eliminated for one final single scalar differential equation in matrix for that becomes the inhomogeneous Laplace's equation as shown in equation (0.99).

$$\begin{bmatrix}\mathbf{e}_x\\ \mathbf{e}_y\end{bmatrix} = -\begin{bmatrix}\mathbf{D}_x^v\\ \mathbf{D}_y^v\end{bmatrix}\mathbf{V} \rightarrow \begin{bmatrix}\mathbf{D}_x^e & \mathbf{D}_x^e\end{bmatrix}\begin{bmatrix}\varepsilon_{xx} & 0\\ 0 & \varepsilon_{yy}\end{bmatrix}\begin{bmatrix}\mathbf{e}_x\\ \mathbf{e}_y\end{bmatrix} = 0$$
$$\begin{bmatrix}\mathbf{D}_x^e & \mathbf{D}_x^e\end{bmatrix}\begin{bmatrix}\varepsilon_{xx} & 0\\ 0 & \varepsilon_{yy}\end{bmatrix}\left(-\begin{bmatrix}\mathbf{D}_x^v\\ \mathbf{D}_y^v\end{bmatrix}\mathbf{V}\right) = 0 \tag{0.98}$$
$$\begin{bmatrix}\mathbf{D}_x^e & \mathbf{D}_x^e\end{bmatrix}\begin{bmatrix}\varepsilon_{xx} & 0\\ 0 & \varepsilon_{yy}\end{bmatrix}\begin{bmatrix}\mathbf{D}_x^v\\ \mathbf{D}_y^v\end{bmatrix}\mathbf{V} = 0$$

Inhomogeneous Laplace's equation becomes the homogeneous case by replacing $\varepsilon_r = 1$ everywhere.

$$\nabla \bullet \left[\varepsilon_r \left(\nabla V\right)\right] = 0 \rightarrow \begin{bmatrix}\mathbf{D}_x^e & \mathbf{D}_x^e\end{bmatrix}\begin{bmatrix}\varepsilon_{xx} & 0\\ 0 & \varepsilon_{yy}\end{bmatrix}\begin{bmatrix}\mathbf{D}_x^v\\ \mathbf{D}_y^v\end{bmatrix}\mathbf{V} = 0$$
$$\begin{bmatrix}\mathbf{D}_x^e & \mathbf{D}_x^e\end{bmatrix}\begin{bmatrix}1 & 0\\ 0 & 1\end{bmatrix}\begin{bmatrix}\mathbf{D}_x^v\\ \mathbf{D}_y^v\end{bmatrix}\mathbf{V} = \begin{bmatrix}\mathbf{D}_x^e & \mathbf{D}_x^e\end{bmatrix}\begin{bmatrix}\mathbf{D}_x^v\\ \mathbf{D}_y^v\end{bmatrix} = 0 \tag{0.99}$$

At this point, the matrix equations are ready to be solved for **V**. The metals for the TL must be set to a voltage by means of an excitation **b**. The solution comes from the excitation for the voltages. However, the solution for **b** needs to be constructed at the same time **L** needs to be modified. For each point where there is a forced potential: the row in **L** needs to be replaced with zeros, then place ones along the diagonal element, and place the forced potential in **b.**

$$\begin{aligned}&\mathbf{Lv = 0}\\ &\mathbf{L'v = b}\\ &\mathbf{v = L'^{-1}b}\end{aligned} \tag{0.100}$$

Constructing **b** is built by creating a force matrix **F** and forced potentials $\mathbf{v}_f$. The force matrix is a diagonal matrix containing ones in the diagonal positions corresponding to the values that need to be forced, or where the metals are. The forced potential functions is a column vector containing the forced potentials. Any number in positions not being forced are ignored. First, to build **b** the rows in **L** need to be replaced with all zeroes that correspond to metals on the grid. Then place a one in the diagonal element by adding

F to **L**. finally, pace the forced potentials in **b**. The remaining elements in **b** must be zero to keep Laplace's equation consistent.

$$\begin{aligned}\mathbf{L}'' &= (\mathbf{I}-\mathbf{F})\mathbf{L} \\ \mathbf{L}''+\mathbf{F} &= \mathbf{F}+(\mathbf{I}-\mathbf{F})\mathbf{L} = \mathbf{L}' \\ \mathbf{b} &= \mathbf{F}\mathbf{v}_f\end{aligned} \tag{0.101}$$

The problem can be solved to find the scalar potential.

$$\mathbf{v} = (\mathbf{L}')^{-1}\mathbf{b} \tag{0.102}$$

The *E* field can be calculated from *V*. Then the D field can be calculated from the *E* field and the permittivity tensor.

$$\begin{aligned}\begin{bmatrix}\mathbf{e}_x \\ \mathbf{e}_y\end{bmatrix} &= -\begin{bmatrix}\mathbf{D}_x^v \\ \mathbf{D}_y^v\end{bmatrix}\mathbf{V} \\ \begin{bmatrix}\mathbf{d}_x \\ \mathbf{d}_y\end{bmatrix} &= \begin{bmatrix}\varepsilon_{xx} & 0 \\ 0 & \varepsilon_{yy}\end{bmatrix}\begin{bmatrix}\mathbf{e}_x \\ \mathbf{e}_y\end{bmatrix}\end{aligned} \tag{0.103}$$

Recall that there was an ε_0 in the equation. It was removed to keep the functions normalized. It will be incorporated in the distributed capacitance. Finally, the TL parameters can be calculated by finite differences. The distributed capacitance C is calculated by numerical integration and assuming that $V_0 = 1$.

$$C = \frac{\varepsilon_0}{V_0^2}\iint_A \left(\vec{D}\bullet\vec{E}\right)dA \rightarrow C = \mathbf{d}^T\mathbf{e}\left(\varepsilon_0\Delta x\Delta y\right) \tag{0.104}$$

The distributed inductance L is calculated from the capacitance for the homogeneous case.

$$L = \frac{\mu_{r,h}}{c_0^2 C_h} \tag{0.105}$$

The characteristic impedance Z_0 and the effective refractive index n_{eff} is given by the distributed inductance and distributed capacitance.

$$Z_{0.} = \sqrt{\frac{L}{C}} \tag{0.106}$$

$$n = c_0\sqrt{LC} \tag{0.107}$$

The static approximation is calculated very fast, but it does not include the fringing fields at the edges of the TLs. Normally, parallel plate designs used for capacitors are very thin and very wide. The fields in these plates concentrate in the middle of the plates. In those cases, the fringing fields can be omitted. The PPTLs designed for this research are narrower, making the fringing fields more pronounced. This was the reason for using the Finite-Difference method to calculate the PPTL parameters more accurately. Figure 6.2 describes the results from finite differences for implementing the solution for the fields for the TLs. In this calculation, a microstrip, coplanar, and stripline TLs were solved. It can be observed that the distribution of the fields is contained by their ground planes. However, the large planes represent a problem for bending these geometries into a 3D meandering TL. Figure 6.3 presents a slotline, open two-wire, and coaxial TL designs. The slotline has the same problems as the previous TLs. The open two-wire TL is a good candidate but the fields are not contained as good as the other TLs.

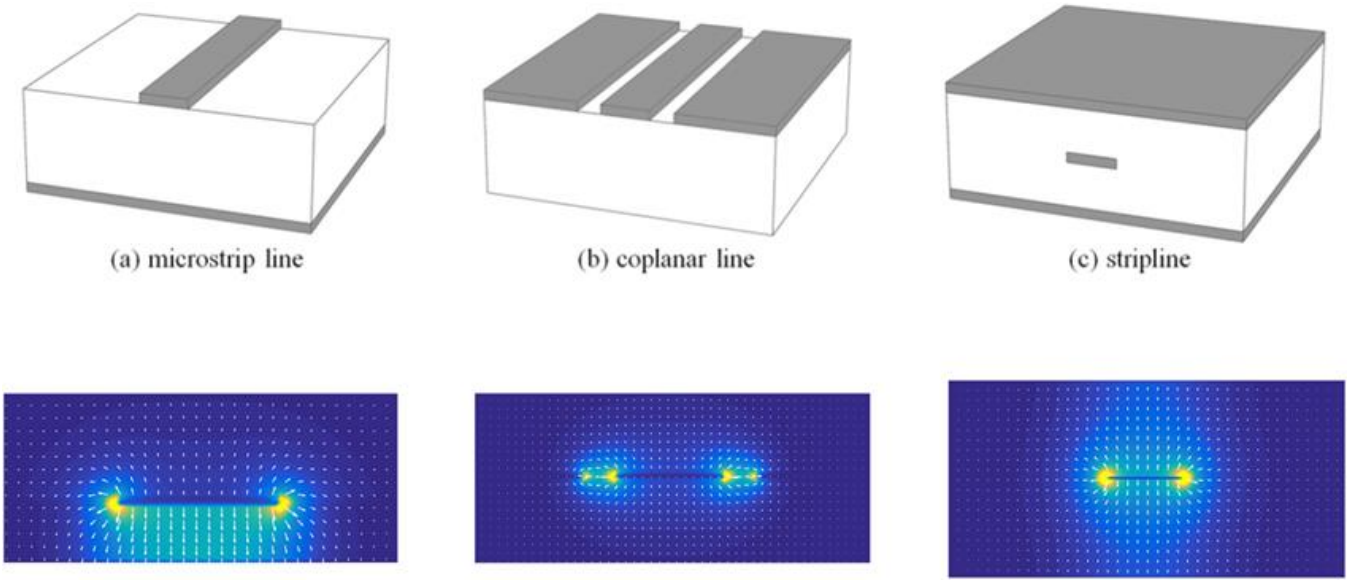

Figure 6.2: Finite-Difference method implementation for microstrip, coplanar, and stripline designs

The coaxial is a great candidate since it contains the fields completely; however, its manufacturing in 3D space brings more questions than the other TLs.

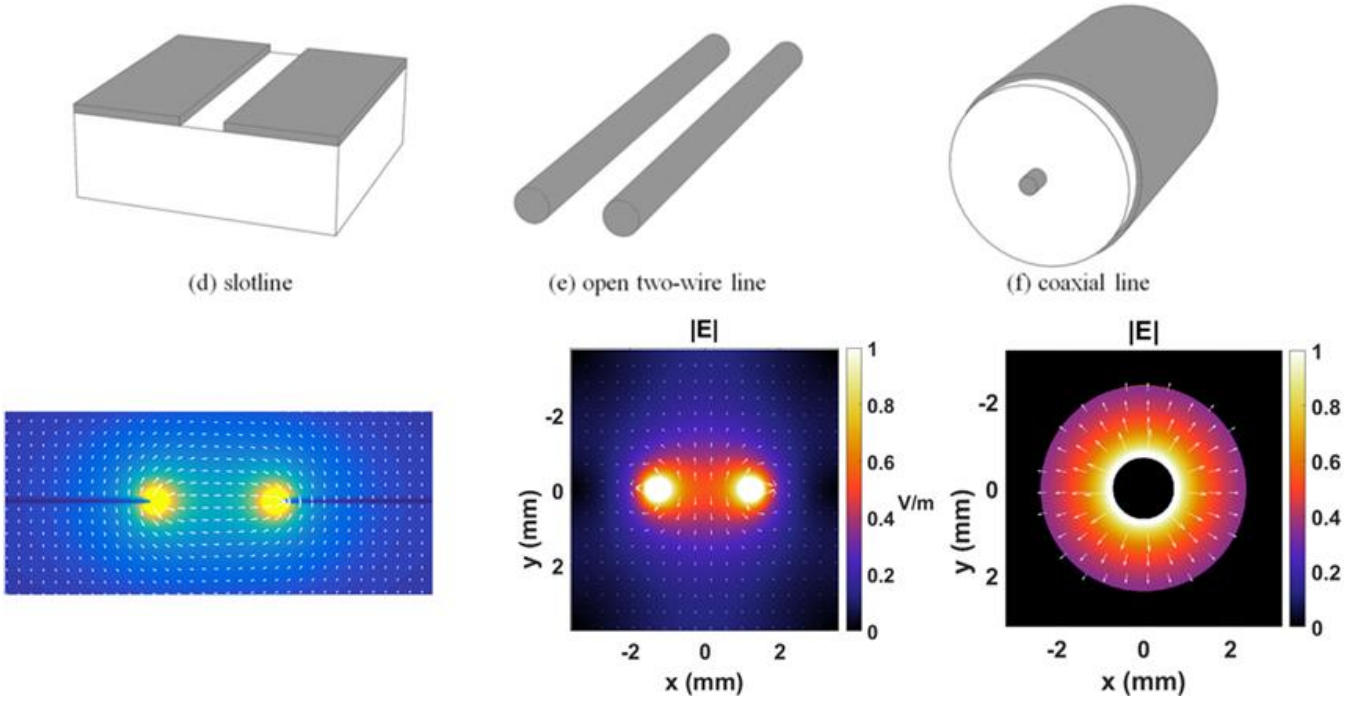

Figure 6.3: Finite-Difference method implementation for slotline, open two-wire, and coaxial designs

The next step is to calculate the ratio between the width of the plates *w* and the separation between them *h* in order to see what ratios produce a 50 Ω TL. This was done by running the same solution inside a script using finite differences in MATLAB. The script calculates the fields and the characteristic impedance for one design of PPTLs. Then, it runs a loop with a fixed $w = 4.4$ mm over a range of distances for *h*. The range of distances has 500 points to calculate the distance between the plates. The distance starts at 500 μ and it ends at 2 mm. Then, each point produces one simulation that outputs a ratio and a characteristic impedance value. Figure 6.4 shows the simulation results for the w/d ratio versus the results of the characteristic impedance. The results show that a PPTL with a ratio of 3.5 will yield a 50 Ω PPTL. This answer is very helpful to design any size PPTLs with 50 Ω impedance. Then, as long as the ratio is kept, the width and height of the PPTL can vary in size. Notice there are three distinctive values for the permeability in the study. The calculation uses three well-known materials: Air, ABS plastic, and

FR4. In this study, FR4 has the lower ratio since its permeability is lower. Then, air needs a larger ratio to create a 50 Ω PPTL. ABS is the best choice for 3DP since it has a lower ratio.

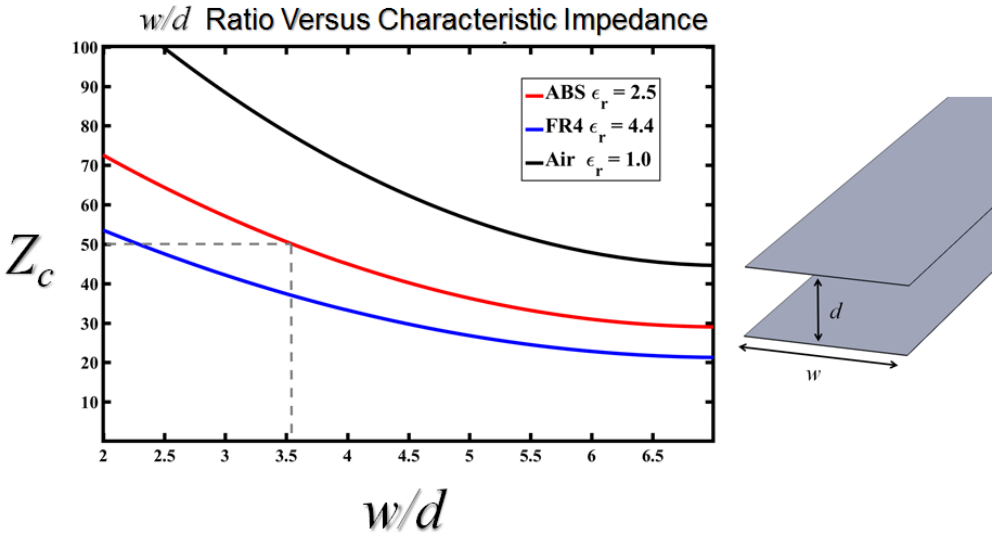

Figure 6.4: w/d Ratio versus characteristic impedance.

6.3 CALCULATE PROPERTIES AND VALUES FOR PPTL

Once Maxwell's equations are solved into wave solutions, the properties of PPTLs can be calculated. Physical dimensions, material properties, and geometry attributes are all essential to designing functional TLs. The first step is to find the variables needed given by our previous derivations that calculate the physical properties and define a working model of a PPTL. Figure 6.1 covers the variables needed to calculate a working PPTL of desired 50 Ω TL attributes. Figure 6.5 attaches the variables and attributes to the geometrical design of the PPTL.

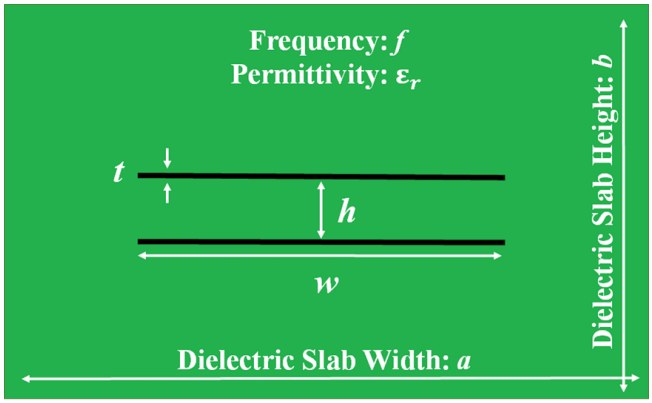

Figure 6.5: Geometrical features and parameters of a PPTL

6.3.1 PPTL Parameters

In order to calculate the parameters of the PPTL, we solve the equations in section 6.2.5 for 50 Ω TLs. The target impedance is 50 Ω in order to have a matched TL to connectors and measurements later on. Figure 6.6 shows the design and the calculated results.

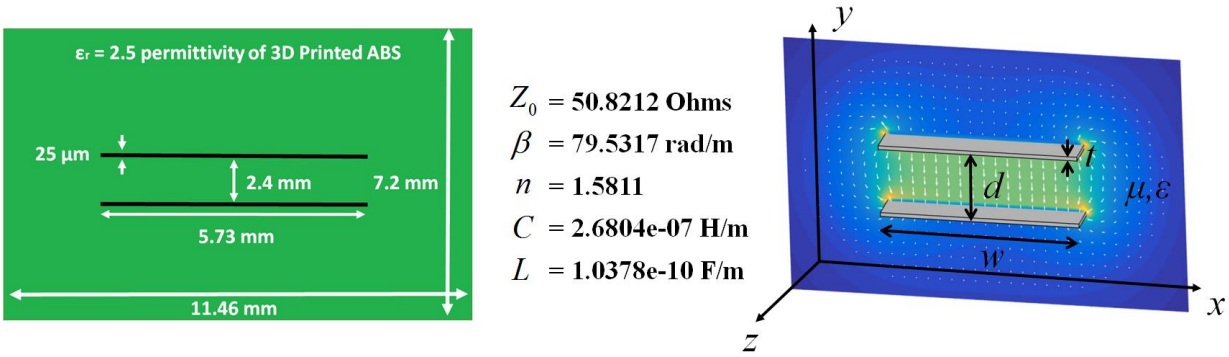

Figure 6.6: Design, results, and model for 50 Ω PPTL.

These dimensions are a combination of 3DP considerations from the manufacturing capabilities of the printer and results from simulations. The thickness of the parallel plates (25 µm) comes from the minimum height that can be dispensed using the SmartPump™. The width and height of the substrate comes from the minimum distance required to contain fields inside the dielectric. Later on, the parameters change according to the manufacturing changes needed for including SMA connectors, as bends take place out of the *xy*-plane, and the size of the pen tips is changed to accommodate printing.

Chapter 7: Design of 3D PPTLs and Test Coupons

The improvements seen from the dielectric structures, filters, antennas, and microstrips show the performance closing in to current industry devices [13][11][16][54]. Microstrips, striplines, and coplanar waveguides have been successfully fabricated using 3DP [55][56]. These TLs, however, are not as well suited for transmitting energy through arbitrary 3D shapes as PPTLs. This chapter will cover the details, processes, and methodologies of creating 3D bend designs that exploit the third dimension for PPTLs. This research is focusing on PPTLs since their design is simple, with two flat plates, they confine fields, they have freedom to be routed in 3D, and building PPTL using 3D printing is a logical first step to prove the capabilities for electronics to be implemented onto the third dimension.

7.1 Parallel Plate Transmission Line Designs

In this research, we identified design rules and best practices for routing PPTLs in 3D circuits. As PPTLs are routed, three basic bends were be studied: (1) in-plane bends, (2) out-of-plane bends, and (3) twists, or barrel rolls. Any type of meandering can be identified as some combination of these three bend types. Furthermore, sharp turns in PPTLs cause reflections and spurious scattering just like in microstrips [44]. Usually, these effects can be alleviated by mitering the edges, introducing tapers, or adding filters [9][42][51]. The slow transitions theoretically decrease unwanted effects that a sharp edge would cause.

ANSYS Electronics Desktop was used to design every meandering PPTL in this study. Initial designs used perfect electric conductors (PEC) to converge to preliminary designs more rapidly, and then realistic material properties were incorporated to finalize the designs. The designs also started with ABS boxes that encompassed the PPTLs then moved onto adding plastic enclosures that had the same dimensions intended for the end 3DP device. As a last step, SMA connectors were added to the input and output of the PPTL designs.

7.1.1 Straight PPTL

In section 2.1.5 of this dissertation, the initial design of the PPTL was described. The model used for simulation model is shown in Figure 7.1. The straight PPTL is fully embedded in acrylonitrile

butadiene styrene (ABS) plastic with a dielectric constant of $\varepsilon_r = 2.5$ shown in green. Passive rectangular wave ports were used as the source of excitation with red outlining the input wave port and blue outlining the output. The PPTL itself has a width of $w = 5.35$ mm and a height of $h = 1.58$ mm with a conductor thickness of $t = 25$ µm. Since this model is meant to be ideal (enclosed in a large ABS box containing no loss) it was only used to tune the dimensions of the PPTL in order to achieve 50 Ω impedance.

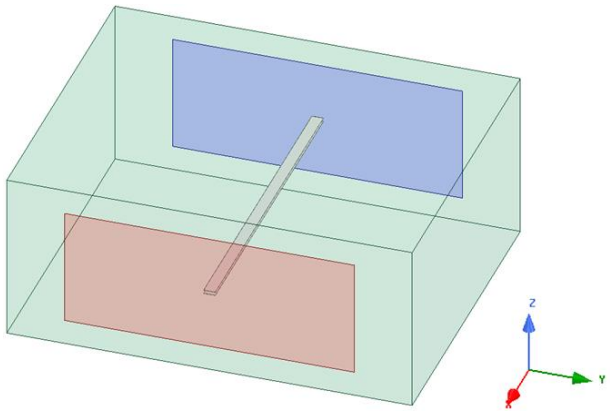

Figure 7.1: Simulation model of a straight PPTL

Then, a printable model based on the ideal model was designed. Figure 7.2 shows the simulated model, which is intended to more closely resemble the physical devices. It contained a smaller ABS box that extends $2w$ by $3h$. These dimensions were chosen as adequate enough to confine the propagating mode within the PPTL. The model is also outfitted with SMA connectors (Amphenol RF 132322) that are used as the source of excitation for this model [52]. The simulated results for our test set-up along with those from ideal simulations are shown in Figure 7.2. As seen, device performance significantly deviates from an ideal model to one that uses SMA connectors. Section 7.2 further explains the use of SMAs in our models. It was found that removing the top prongs of SMA connectors was the simplest way to obtain improved device performance. Other methods, such as tapers and other techniques for mode matching did not provide much improvement.

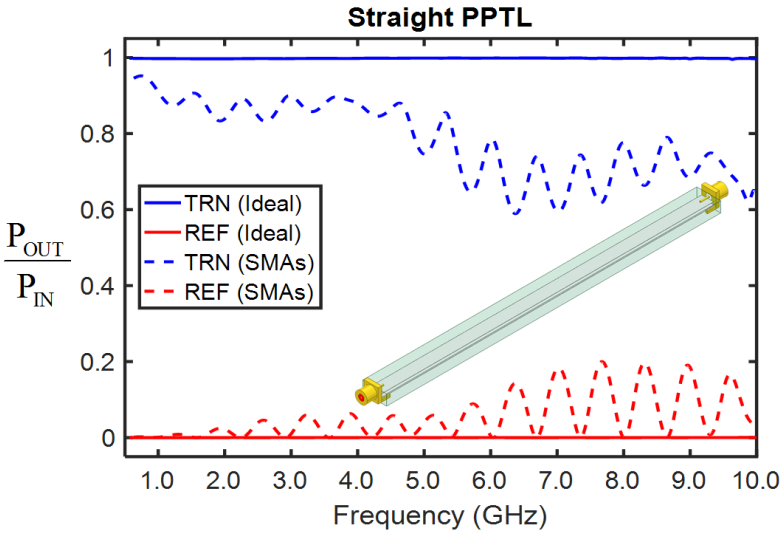

Figure 7.2: Straight PPTL HFSS model and simulation results.

7.1.2 In-Plane Bends

Initially, we modeled a series of parallel plates with varying bend radii to find out bending rules that would maintain maximum transmittance. We assumed perfect conductors fully embedded within ABS plastic. Our first simulation was of a parallel plate with a width of w = 3.48 mm and a height of h = 1.00 mm. Its characteristic impedance was 50 Ω from 500 MHz to 10 GHz. Figure 7.3 shows the power transmitted and reflected with bend radii r of 5 mm, 10 mm, 15 mm, 25 mm, and 50 mm at an angle of 90°. Below 10 GHz, both small and large bend radii did not have negative effects on reflectance and transmittance.

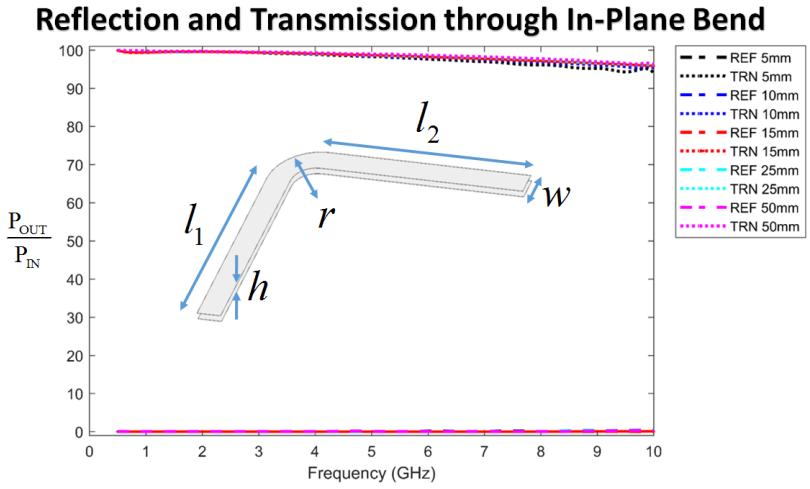

Figure 7.3: In-plane PPTL power loss as a function of a radii sweep

During our second simulation, the dimensions of the PPTL were changed keeping the same characteristic impedance. This PPTLs have a width of w = 5.60 mm and a height of h = 1.73 mm making the design to have a larger gap separation between plates. Figure 7.4 demonstrates the power results where transmittance appears to degrade faster than the previous simulation. The trend is still independent of the bend radii. The loss of in an in-plane bend is not considerable affected by the radius r.

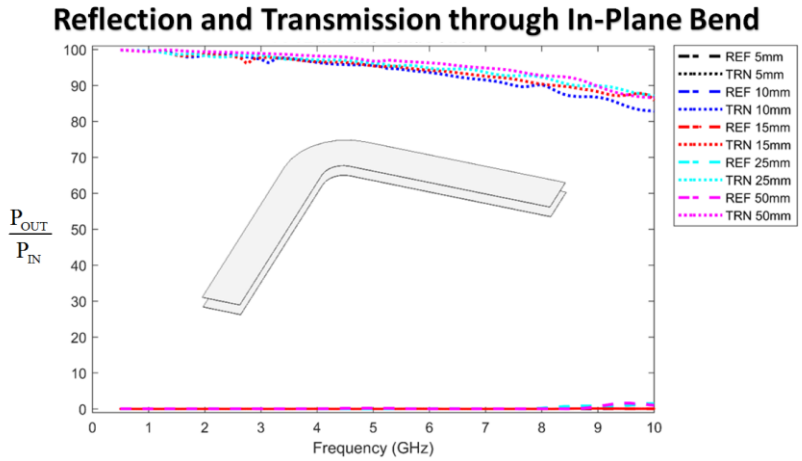

Figure 7.4: In-plane PPTL power loss as a function of a radii sweep

The two previous simulations showed no decrease in functionality up to 10 GHz when simulated with wave ports. To decrease printing time, the enclosing ABS box was reduced to a 2w by 3h in order to keep the same functionality but with reduced dielectric material. Then, the smallest device (bend radii of 5.7 mm) was modeled SMA connectors shown in Figure 7.5 to take into account the transition between connectors and PPTL. As shown, transmittance is in blue and reflectance is in red. For reasons described in the straight PPTL section, the top two prongs of the SMA connectors were removed. Even still, the loss of power and rolling behavior of the signal is attributed to the transition from SMA connector to PPTL.

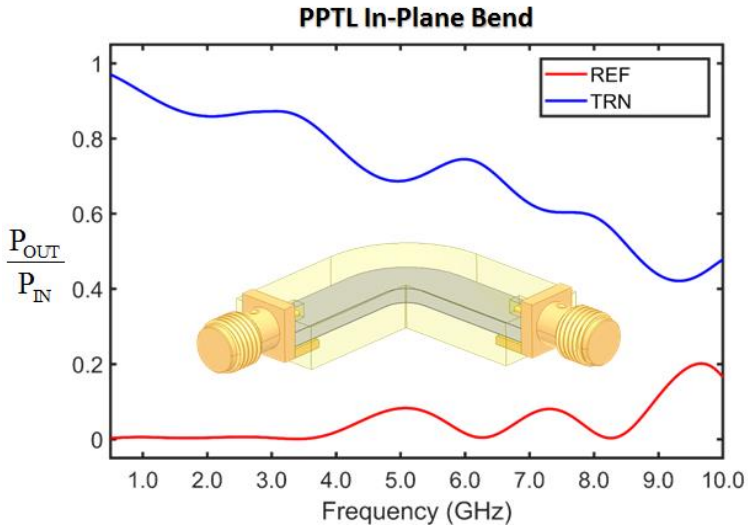

Figure 7.5: Small radius in-plane bend HFSS simulation and model.

7.1.3 Out-of-plane Bends

Similarly, models were built for a 90° out-of-plane bend. Expecting similar results to those of an in-plane bend. Two simulations were done where one had a very sharp bend and one with a larger bend radius (r = 0.8825 mm and r = 25.8775 mm respectively) as opposed to a larger variety of bend radii. The physical dimensions of the PPTLs remained the same as the previous bend in order to have a design that works with SMA connectors. The simulated models are shown in Figure 7.6 along with the electric field distribution at 5.25 GHz. The models are fully embedded in ABS with a relative permittivity of 2.5. The materials used for simulation were lossless and perfect electric conductors for the parallel plates. Passive rectangular wave ports are used as the form of excitation (red for input and blue for output).

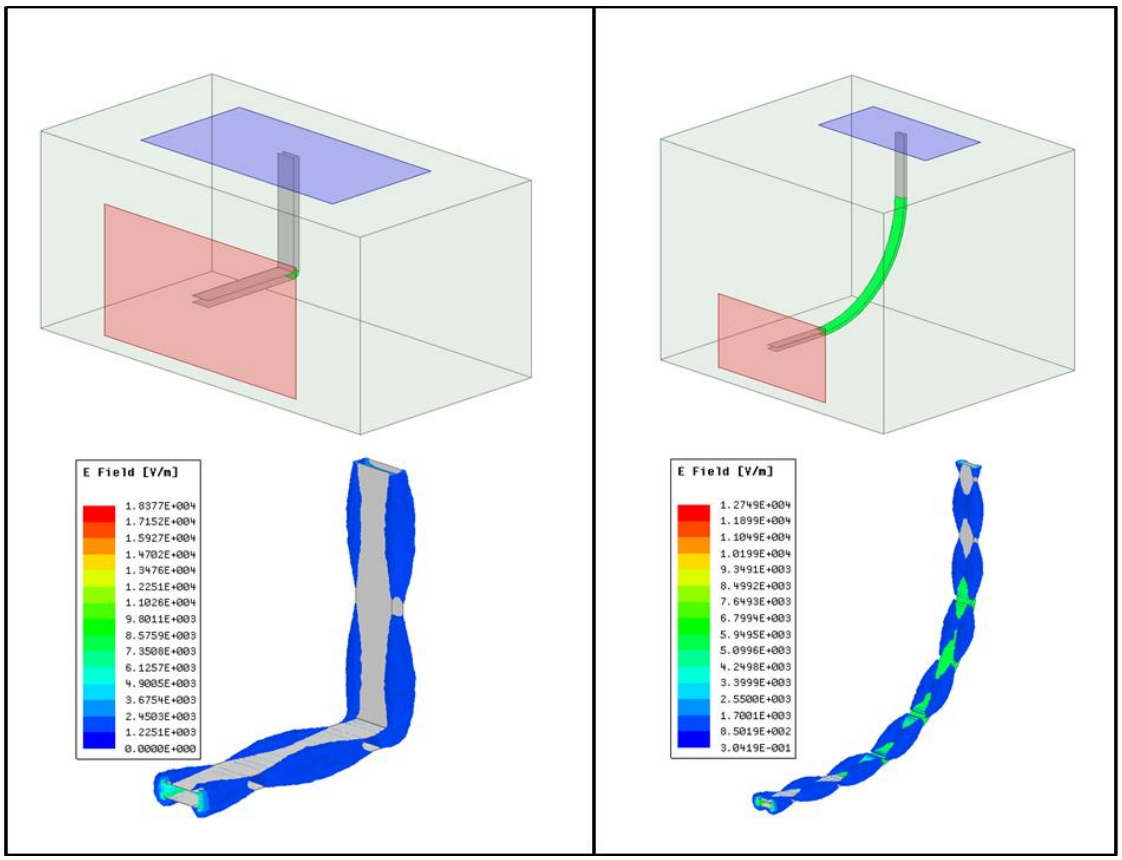

Figure 7.6: (Left) shorter or tight bend radius simulation and field distribution. Bent section is outlined in green. (Right) Large bend or longer bend and field distribution.

Figure 7.7 shows simulated results for these out-of-plane bends, where the reflection and transmission are shown in dashed lines and results for the longer bend radius are solid lines. No SMA or reduced ABS box was applied. What was observed from these simulations was that bends that are tighter, (happened over a short distance) would maintain the overall transmission of the model over the bends that are loser (happened over a longer distance). In-plane bends had a power drop at high frequencies when the dimensions were adjusted to those matching our SMA connectors. However, as opposed to the in-plane bends, slight rolling behavior indicative of a standing wave was observed in the out-of-plane bends.

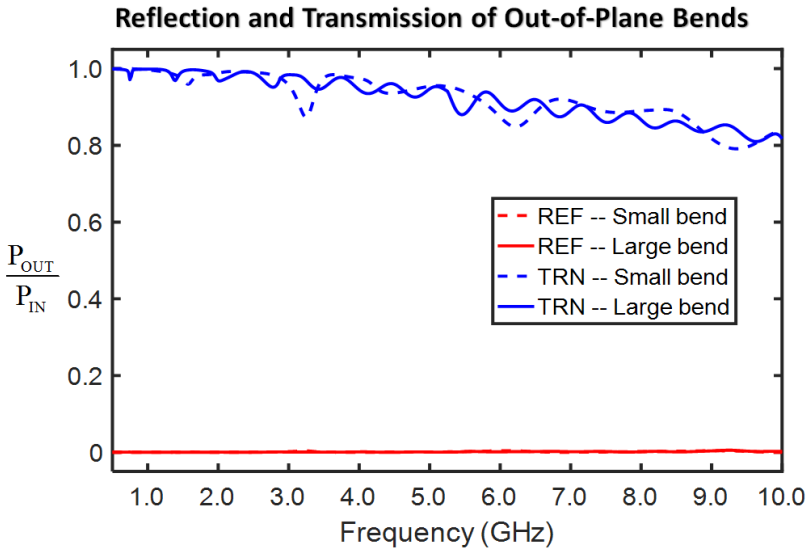

Figure 7.7: Plot showing linear response of out-of-plane bends for two different bend radii with PEC and no SMAs.

Then, the sharp bend radius out-of-plane PPTL was modeled for 3DP since it would lead to shorter printing times. The modified model containing SMA connectors is shown in Figure 7.8. The simulated results for this model are also shown with transmittance in blue and reflectance in red. Like the models before it, the transition from SMA connector to PPTL was poor.

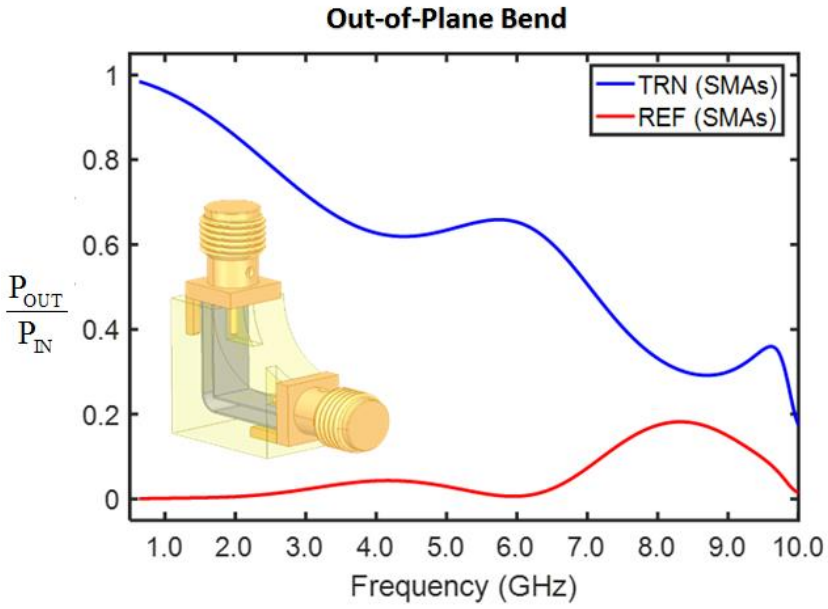

Figure 7.8: Small radius out-of-plane bend HFSS simulation and model

7.2 SMA To Parallel Plate Transition

The SMA connector was simulated using the Finite-Difference Method, as it is composed of a coaxial transmission line. Then the simulation was compared to a PPTL composed of a top and bottom conductor. Figure 7.9a describes the models with their corresponding field distributions. From these electrostatic simulations, we are able to determine the characteristic impedance Z_0, distributed capacitance C, distributed inductance L, and effective refractive index. The characteristic impedance and the mode profile matching the transition between SMA and PPTL are of particular interest for us. In order to achieve a high transmission efficiency, the impedance of both the SMA and the transmission line must be the same. For this transition, we chose 50 Ω PPTL lines. Then, the physical dimensions of each line were scaled until the impedances were sufficiently matched. For the PPTL, h is 0.75 mm and w is 5.9 mm. For the coaxial line, r_i is 0.375 mm and r_o is 1.275 mm. The mode profile must also be matched. The magnitude of standing waves at the transition between SMA and PPTL helped to calculate how much power is lost in reflections.

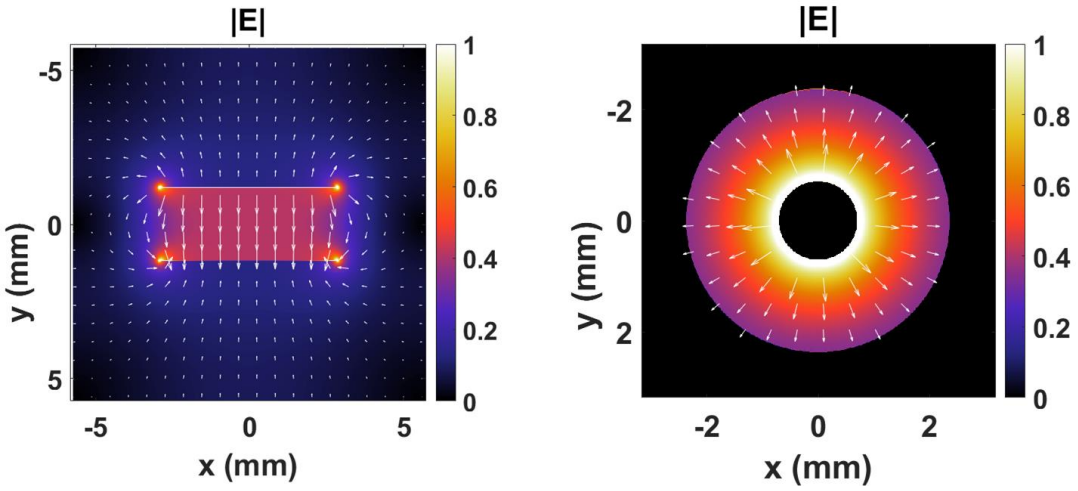

Figure 7.9: (Top) Coaxial transmission line model and field distribution. (Bottom) PPTL model and field distribution.

The physical dimensions obtained from the matched impedance models allowed a basic 3D model in HFSS. Figure 7.10 shows the straight PPTL model with two SMA connectors at the input and output. The model is suspended in air, it has PEC at the plates, and has no dielectric materials in order to simplify the model as much as possible and minimize any possible factors that might cause reflections. For the

same reason, no material absorption loss is incorporated into the ABS box or metals. Perfect conductors are used instead of finite conductivities and a Teflon with a simple dielectric constant of 2.1 is used for the SMA connectors. In order to achieve a proper connection between the PPTL and SMA, the top conductor required a small gap of 1.0 mm between the top plate and the SMA pin to avoid a short circuit from signal to ground. This small gap shown closer on the right in Figure 7.10 on the right.

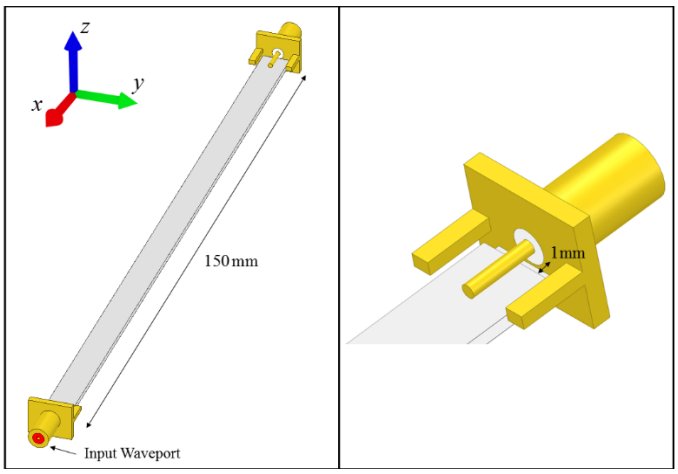

Figure 7.10: (Left) SMA to PPTL to SMA HFSS model. (Right) SMA model showing 1 mm gap.

7.2.1 Fitting SMA Connectors

Cavities were added in the ABS box for SMA connectors to fit easily on the final devices (shown in Figure 7.15). Due to inaccuracy in the physical dimensions of printed models, these cavities needed to be 300 μm wider in all directions adding 1.11 mm in total width. The only cavities that were added are for the two prongs and for the pin of the SMA connector.

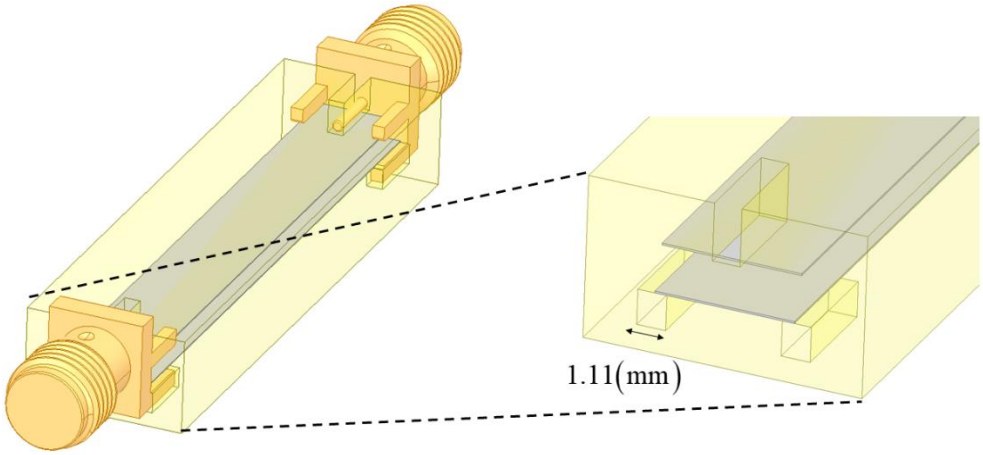

Figure 7.11. Final printable model containing voids to properly fit SMA connectors and a reduction in overall transmission line length.

7.2.3 Simulated Results

The simulated results of the SMA to PPTL to SMA transitions from 500 MHz to 10 GHz are shown in Figure 7.16. It can be seen that the overall transmission of the PPTL significantly decreases as frequency increases when SMAs are included. Recall Figure 7.2, it shows simulations without the SMAs in place with the expected response of full transmission and no reflections. The following results are labeled “type 1 SMA.” With the use of perfect material boundaries, these reflections are due solely to the poor transition from SMA to PPTL. As was shown in Figure 7.12, the SMA contains a cylindrical mode when compared to the linear mode of a PPTL. This mismatch in mode profile is the primary cause of reflections. The rolling observed is caused by a standing wave produced by the impedance mismatch. As to the severity of these reflections, we continued to alter our model to further observe the effect of SMAs.

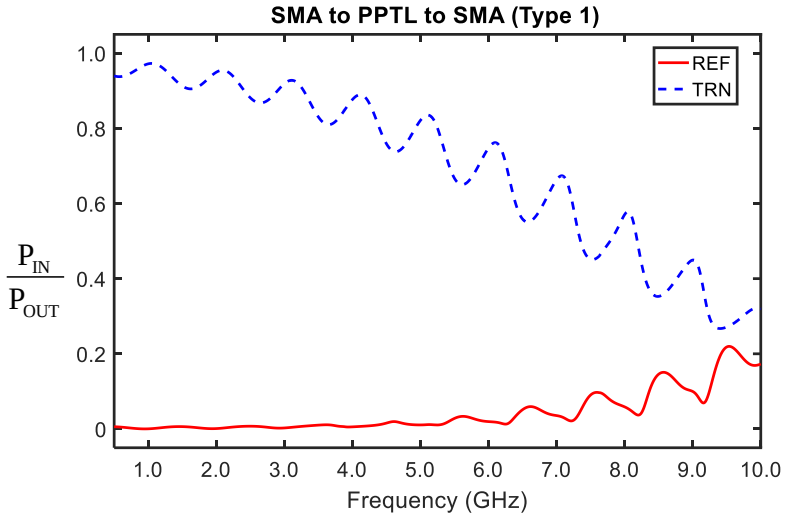

Figure 7.12: Simulated results of two transitions of SMA-PPTL to PPTL-SMA. Plot shows transmittance in a dashed blue line and reflectance in a solid red line.

Following this, the same setup was simulated with a new SMA model labeled "type 2 SMA." For the type 2 SMA, all the prongs extending from the base of the SMA were removed. This model is shown in Figure 7.14. Our interest here was to alter the SMA topology slightly in attempt to sculpt the fields leaving the SMA to look closer to the ones matching the mode in the PPTL. The results of this simulation are shown in Figure 7.15 along with the ones with the previous SMA model. As can be seen, the overall response of the device improved by 35% of power losses. However, rolling behavior indicative multiple scattering points is still observed. A single transition was simulated to reduce the components of the simulation.

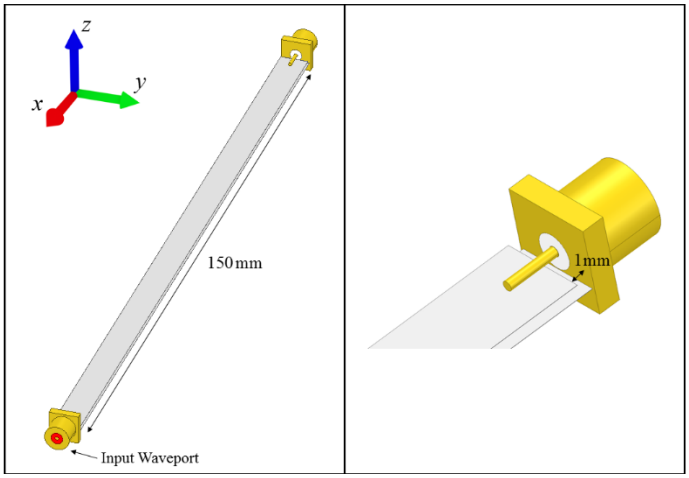

Figure 7.13: (Left) "Type 2" SMA model. (Right) Close up of "type 2" SMA showing removed prongs.

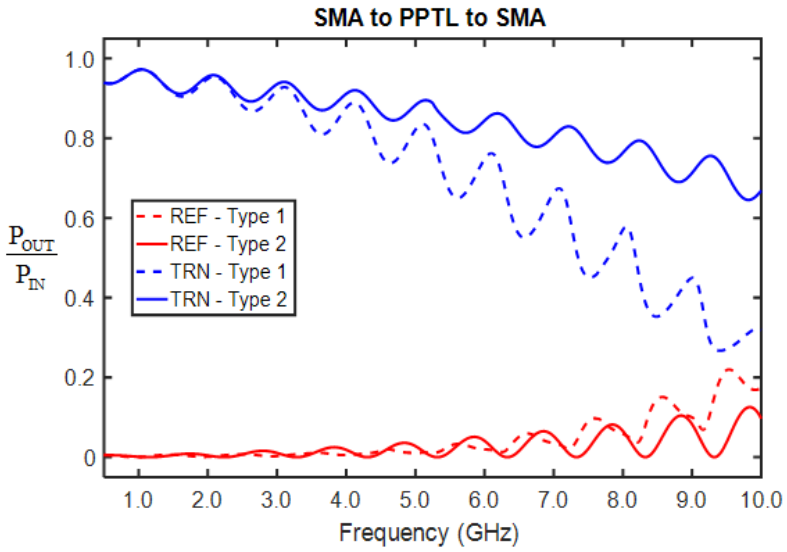

Figure 7.14: Simulated results for both SMA models. "Type 1" results are shown in dashed lines and "type 2" results are shown in solid lines.

To substantiate the reflections observed are caused by the SMA connectors. This final setup and simulated results are shown in Figure 7.15. For this setup, a single SMA connector as the source. Opposite to the source is a rectangular wave port outlined in blue. As opposed to an SMA, this wave port is passive and does not load the PPTL in anyway. Effectively this models a single SMA to PPTL transition as opposed to the two transitions in our previous models. We observe that the response of the device is improved further with a higher amount of transmission when compared to the two SMA model. By removing an SMA, we are closer to achieving the ideal response of a transmission line. This is a good indicator that the loading of the SMAs is what is causing the reflections we are observing in the models.

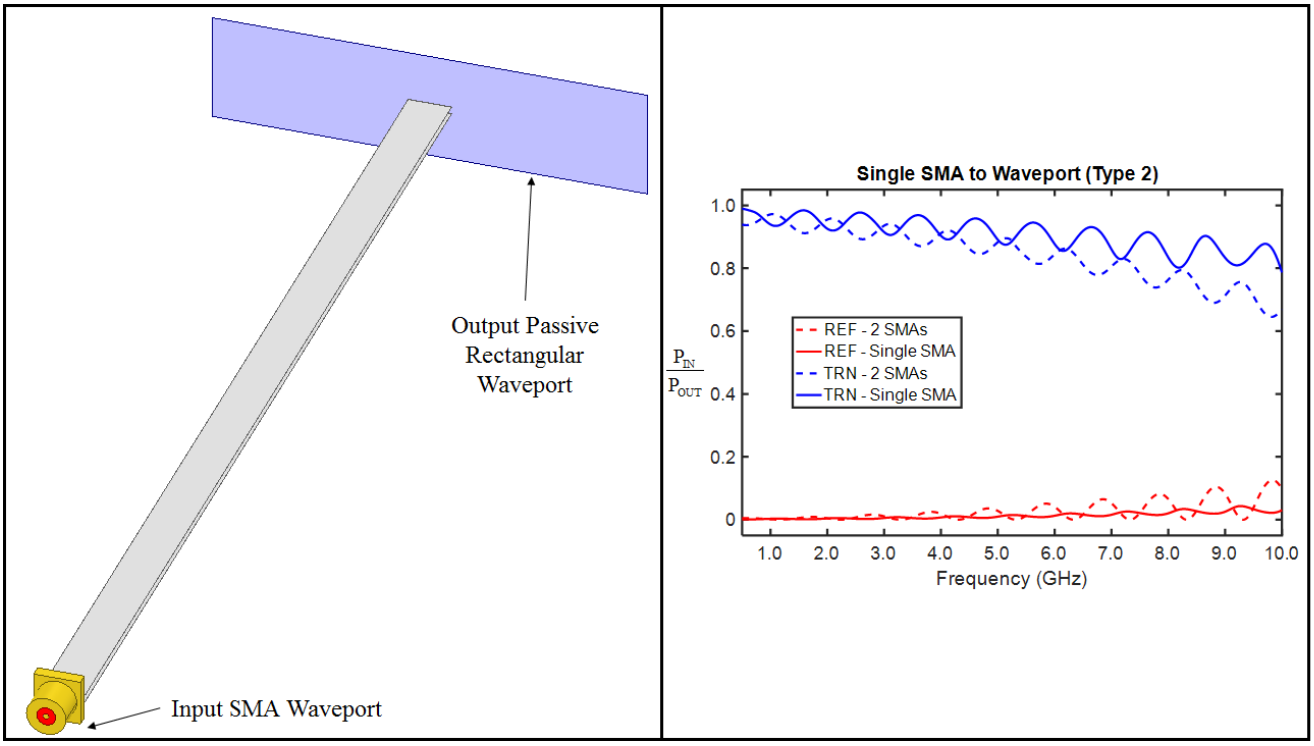

Figure 7.15: (Left) Single SMA to Wave port HFSS model. (Right) Simulated results show an improvement over a model that uses two SMAs.

Chapter 8: 3D Printing of Parallel Plate Transmission Lines

Moving from the PPTL design and simulation into manufacturing requires processing the considered models into a 3D printing software methodology, preparing the nScrypt printer, and post-treating the printed devices. This chapter covers the printing process development of PPTLs. Currently; these printers are primarily used to print flat electronic devices containing planar traces that require multiple processes. In addition, the printer is capable of printing within a tolerance of 1.0 μm, which makes it very sensitive to changes implemented at the micron level. Preparing the materials ahead of time, finding the proper configurations to print the devices, and maintaining the performance throughout the print jobs were the most challenging and time-consuming tasks of this research.

8.1 3D Printing Rules and Preparations

The preparation for the manufacturing of PPTLs consisted of managing the materials, initializing the settings of the 3D printer, and handling the printing environment. Furthermore, this section describes rules and settings for manufacturing the PPTLs in detail. As the models were printed, there was a need for adjustments to the initial rules and preparations to accommodate for layer thicknesses and printed line widths.

The PPTLs were manufactured using the practices developed in previous chapters. Table 8.1 summarizes the printing parameters previously set on the machine for the PPTs. EPOTEK H20 conductive epoxy was used to bond the SMA pin and prongs onto the parallel plates. The benefit of the conductive epoxy is its ability to hold the SMA connectors in place while providing a conductive seal. In addition, optical epoxy was used to create a bond with the SMA and ABS box body. This was made to strengthen the adhesion of the connectors while avoiding the conductive epoxy to be broken during the measurement step.

Table 8.1: Printing parameters for PPTLs

	nTips	**Dispense gap**	**Print ratio**	**Print speed**
SmartPump™	125μm	55 μm	1.06	60 mm/s
nFD™	125 μm	55 μm	0.98	20 mm/s

The nScrypt Tabletop printer is fitted with two heating elements that control the printing surface, or heat plate, and the nFD™ heating element that can go up to 450˚C. The heat plate was set to 74˚C so

ABS material can adhere to a hot surface. The surface was also covered with polyethylene terephthalate (PET) tape, which consists of tape with silicone adhesive mostly used in high temperature masking. In addition to the tape and heated surface, we add a thin layer of a solution made of extruded ABS (~10 gr by weight) with approximately 400 ml of acetone by volume. As the acetone dilutes the ABS plastic, a sticky solution is produced that creates a layer of thin plastic on top of the PET tape as the acetone evaporates. Moreover, the heating element on the nFD™ pump was set to 275 ˚C to achieve a fluid extrusion for the ABS plastic. Several settings are previously loaded in Slic3r that calculate the rate of extrusion and material deposition. The infill rectilinear pattern density is 100% where the infill is combined every alternating layer. Two loops of skirt (wall surrounding printable objects) were used 6 mm away from the printed devices. This helps debris left on the pen tips from the layer to attach itself to the skirt and start every layer with a clean pen tip. In addition, the extra time needed to print the skirt helps the curing time needed for the thin layers of silver ink cure and settle. The printing speeds were set to 30 mm/s with the exception of the support material to be at 20 mm/s. This speed is necessary for thicker lines of ABS, as slower deposits agglomerate material. On the same note, first layer speed is 18 mm/s to ensure good adhesion. The extrusion width was defaulted to 200 μm as the printing is at a height of 50 μm and this makes the tip to over extrude. This helps the printing surface to be smoother than following the pre-set parameters.

As the machine was set for microdispensing, there was a need to manage the ink, the valve, and the pressure used to push the ink. The ink needed to be mixed at least 5 minutes prior to the job since is not a homogeneous mixture of silver micro-particle flakes that tends to separate as time goes by. Mixing the ink prior, helps keep the particles distributed and thus prevents abrupt changes in viscosity throughout the print job. The solvent mixed along the silver ink is abrasive; therefore, we changed the O-rings in the valve from Viton™ fluoroelastomer to Kalrez® perfluoroelastomer O-rings [53]. These new rings behave much better when exposed to CB028 and will not deteriorate even after days of exposure. The drawback to using the new rings is the expense. Perfluoroelastomer O-rings sold by nScrypt are forty times more expensive than Viton™. The valve is set to an opening position and closing position with a difference of 35 μm. The open and close position values depend on the individual settings of the 3D printer. Still, a

pressure of 8 psi is needed to push the material out through the dispenser. The printer environment needs to be managed since it also affects the print jobs. There are suspended particles that can clog the 125 μm pen tips, there is a need to keep a low humidity level since the ABS filament is not hydrophobic, and maintaining a constant printing envelope temperature helps the ABS plastic and silver ink to cure from high temperatures to room temperature. Keeping a clean room environment keeps suspended particles from attaching to the pen tips, deposited materials, process cameras, and heating elements on the printing envelope. In our laboratory, we chose to create a clean room environment where plastic barriers, air extractors, constant room cleaning, and filtered air help us maintain an ISO 7 standard. The entire printer was vacuumed before and after every printing job. The areas around the printer were wiped down to eliminate dust and small particles as best as possible. The nFD™ pen tip was scrubbed down with steel wool to eliminate burnt plastic stuck to the head. Similarly, the ink pen tip was cleaned frequently to prevent ink from clogging the tip. The pen tips were cleaned in periods between one to two hours before any print jobs. If the majority of prints were failing, then a thorough cleaning of the work area must be done, which takes 1 to 2 days. On the same note, low humidity is necessary to prevent water entering the filaments used to 3DP. Once a filament is moist, the extrusion of the plastic releases water in the form of vapor. This affects the temperature of the plastic by cooling it down as it is deposited. Furthermore, the printing lines the nFD™ dispenses do not adhere at the proper temperature we calculated, resulting in uneven surfaces. To treat this, the filament spool was cooked inside a control oven set at 50˚C for at least three hours. This process will remove the moist from the filament to ensure proper extrusion and adhesion in our print jobs. Finally, the printing temperature envelope was monitored constantly since rapid drops of temperature affects the ABS plastic by compressing it too fast. This was fixed by keeping the temperature at the printing room constant and opening the door of the printer only when the print job is done.

Due to the printer being highly sensitive, it is fit to calibrate the printer after every major cleaning and before any print. Calibration involves: (1) finding the floor value of the printing deck, (2) finding the location differences between the nFD™ and SmartPump™, (3) finding the SmartPump™ parameters (pressure, valve open/close positions, valve speed, trigger speed, and layer height), (4) find the nFD™

parameters (perimeter skirt, layer height, layer spacing, and extrusion rate) and (5) tuning these parameters to ensure that printing plastic over a layer of ink will be deposited properly. To test this, there was a need to develop a calibration file as seen in Figure 8.1. The pad features five layers of dielectric, a long strip of ink, a layer of ink surrounded by a perimeter of plastic, and a covered layer of ink. Figure 8.2 shows the attempts at printing the calibration file.

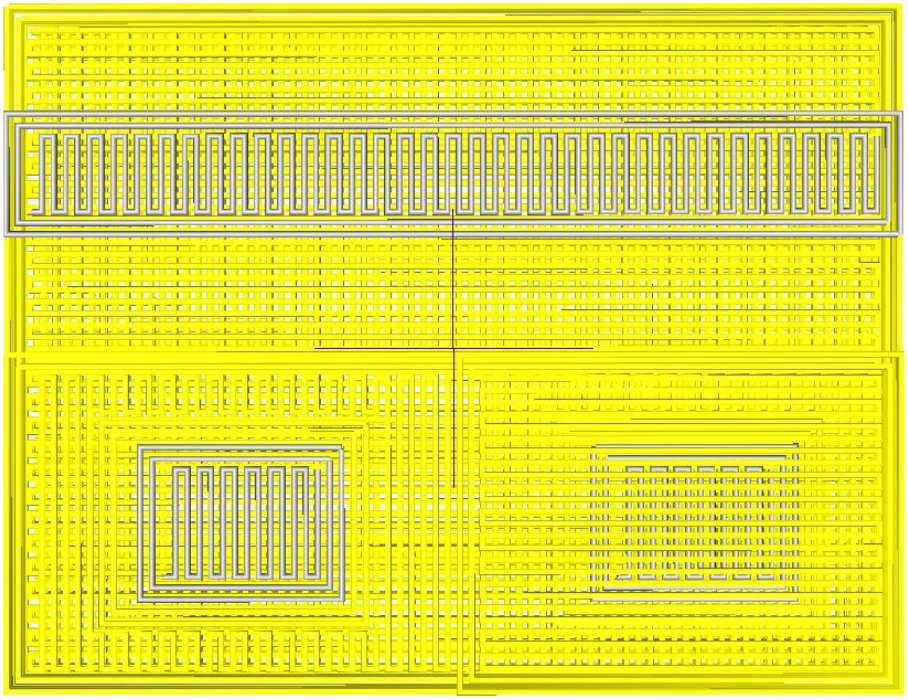

Figure 8.1: (Top) Strip of ink not contained within dielectric. (Bottom left) Two consecutive layers of ink uncovered. (Bottom right) Layer of ink covered by a single layer of dielectric.

The calibration file must be printed before printing a hybrid device. Each file takes five minutes to print. If the calibration parameters are off, then the time taken to calibrate the machine can easily reach a few hours. Once the printer has been calibrated, printing devices can then be attempted. Then, small adjustments might be needed as print goes on.

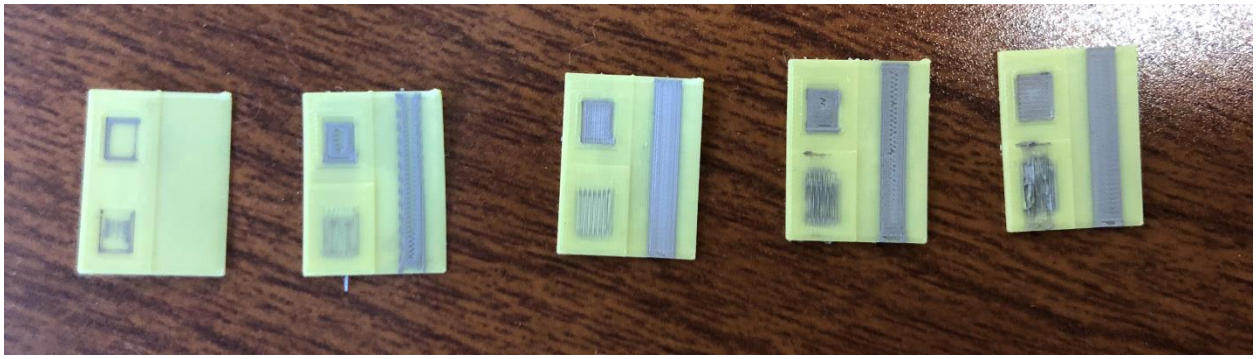

Figure 8.2: Calibration file attempt. (Far left) Little to no ink dispensed. (Middle left) Not enough ink dispensed causing small breaks in the strip. (Middle) Ideal amount of ink dispensed. (Middle right) Too much ink dispensed causing slight smearing. (Far right) Too much ink dispensed causing high smearing.

8.2 SLICING PROCESS AND METHODOLOGIES

As the designs were prepared for printing, there were a few final changes to the simulation models in order to improve their printability. It was decided to print the smaller versions of the designs reducing printing times and, depending on the model, kept prints below 8 hours. Figure 8.3 shows a final printing sliced model used outlining the printing paths through different print stages and close ups on the layers. Green is used for ABS while silver signifies DuPont CB028 silver ink. A skirt was also added to help prevent the bowing of ABS due to the long print times. Lastly, a prime tower was added as a separate object to the model in order to prime both plastic and ink nozzles before beginning a new layer. This prime tower is a simple cubic cylinder of plastic with ink layers inside it. The tower ensured that ink did not solidify on the tip of the dispenser by allowing the ink to continuously flow throughout the print in between layers. Additionally, the thickness of the parallel plates varied through the different bends since the team was finding the best rules of thumb to create thin, conductive, and printable PPTL models.

8.2.1 3D Hybrid g-code Generator

Currently, to print a device with both ABS plastic and DuPont CB028 conductive ink, each material must be printed in a 2D fashion as separate projects with separate g-code files. This makes printing in the vertical direction unattainable unless more sophisticated printing tools are used [54]. In previous chapters, a manufacturing process flow was demonstrated that routed the interconnects, prepared the models for 3D printing, and run a multi-material hybrid 3D printing process. For printing the PPTLs,

the same manufacturing process was used. However, the PPTL designs needed more materials and time than previous devices. Figure 8.3 displays the in-plane bend PPTL at several stages of the slicing process.

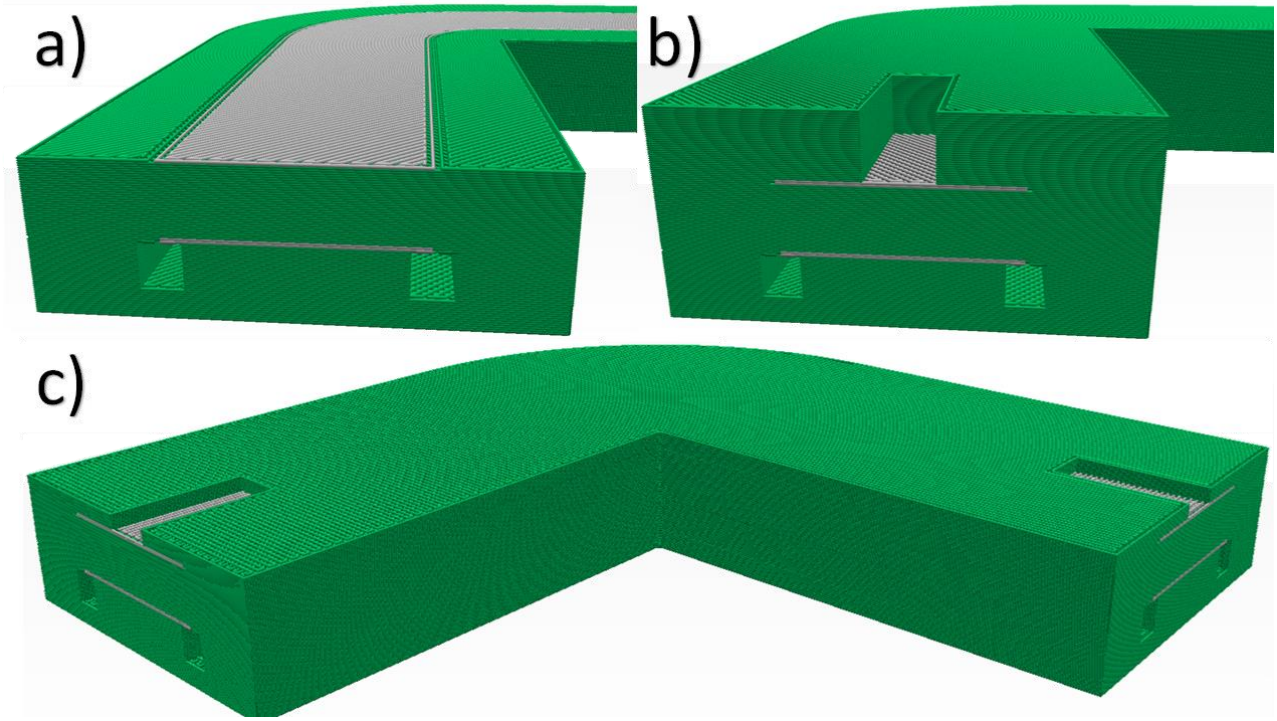

Figure 8.3: a) Zoomed-in view of exposed PPTL. b) Zoomed-in view of covered PPTL. c) Completed in-plane bend PPTL sliced model

8.3 3D Printed Devices

In this section, the slicing of models and 3D printed devices for each PPTL design is demonstrated. There were changes to layer thicknesses, print orientations, addition of priming geometries, and size reductions from to the initial models to make them more printable. Each following section describes the slicing and printing process particularly to each PPTL design.

8.3.1 Straight PPTL

Only one straight PPTL device was fabricated and used as a baseline for both measurements and printing parameters for the rest PPTLs. One of the changes made was a reduction in the straight model to a length averaging 35 mm overall. The overall print time was 5 hours and 4 minutes. The fabricated device is shown in Figure 8.4. EPOTEK H20 conductive epoxy was used to glue the SMA connectors onto the parallel plate. The benefit of the conductive epoxy is its ability to hold the SMA connectors in

place while providing a conductive seal. In addition, we added optical epoxy to enhance the bonding of the SMA connectors to the PPTL. Notice in the figure, the addition of the skirt and the cylindrical tower with plastic and ink. These help the printing process to stay clean and successful.

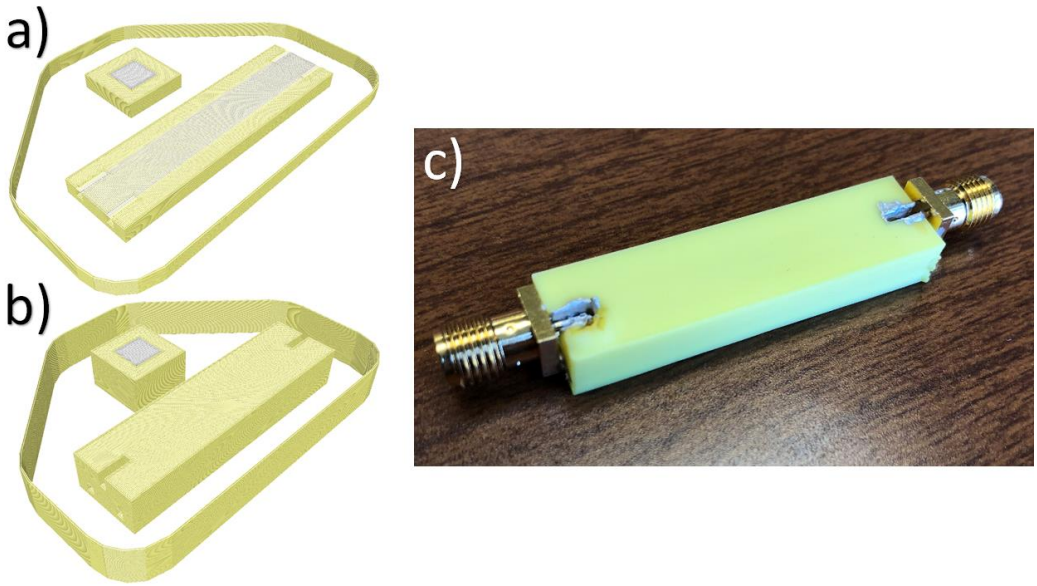

Figure 8.4: a) Layer #53 showing first ink layer printed corresponding to the bottom plate of the PPTL. b) Layer #140 showing fully sliced model. c) 3DP straight PPTL with SMA connectors

8.3.2 In-Plane Bend PPTL

The smallest in-plane bend of 5.7 mm bend radius was printed to save on print time. The thickness of the plates is 75 um and required only one layer of ink. The SMA connectors were attached with EPOTEK H20 conductive epoxy. The sliced models and final print jobs can be seen in Figure 8.5. These devices completed the entire duration of the print and did not have any noticeable defects. The first in-plane bend device was purposely left without conductive epoxy to evaluate its strength and transmission. It was not a successful measurement and the SMA connector was lose. Then, the conductive epoxy and optical epoxy was added to the SMA connectors in the subsequent in-plane bends.

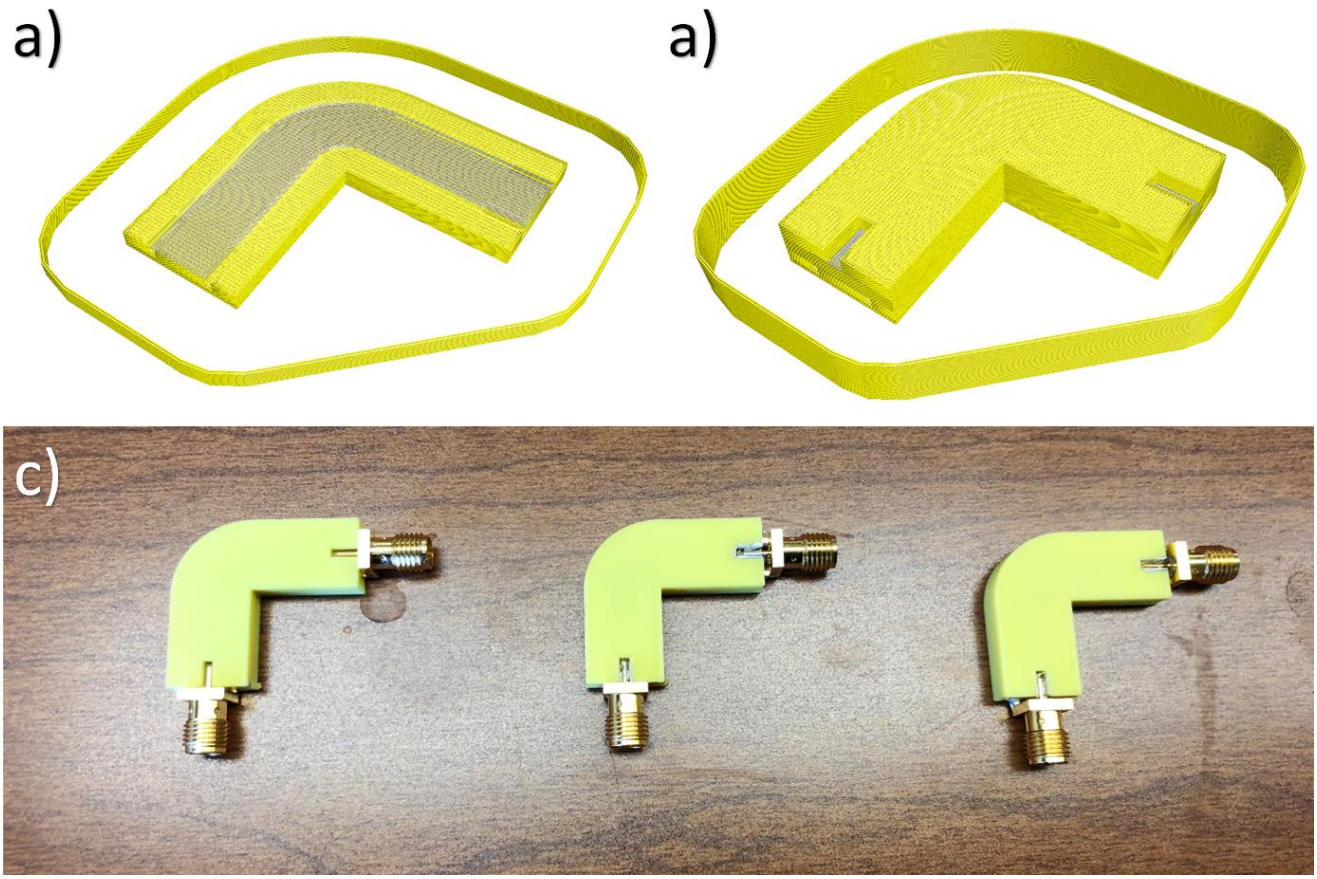

Figure 8.5: a) Layer #35 showing first ink layer printed corresponding to the bottom plate of the PPTL. b) Layer #102 showing fully sliced model. c) three 3DP in-plane bend PPTL with SMA connectors

8.3.3 Out-of-Plane Bend PPTL Printed results

Similar to the models before it, the out-of-plane bend required the same cavities in order to fit SMA connectors. One of the major changes of this model was the need for the plates thicknesses to be increased to $t = 200$ µm. The slicing had trouble recognizing parallel plates going vertically. In order for the ink paths to be properly sliced, they must be at least the size of a line width. This increase in conductor thickness effectively decreased the overall height of our PPTL. It was then necessary to adjust the width of the parallel plate in order for the resistance to remain 50 Ω ($w = 4.4$ mm). The sliced model showing both plastic and ink layers is shown in Figure 8.6. Out-plane-bend PPTLs were had added a level of difficulty as the plates needed to be thicker, fortuitously, good measurements were reported. In total, two out-of-plane devices with a sharp bend radius were completed the full printing process and were good

candidates for measurement. One of these prints was questionable. It was seen during the printing process that not enough ink was dispensed for the conductive paths of this print. This led to empty patches or holes along the conductive plates. When measured, it was found that this line did not function properly. These results were omitted. The measured results for the functioning device are shown in the next chapter

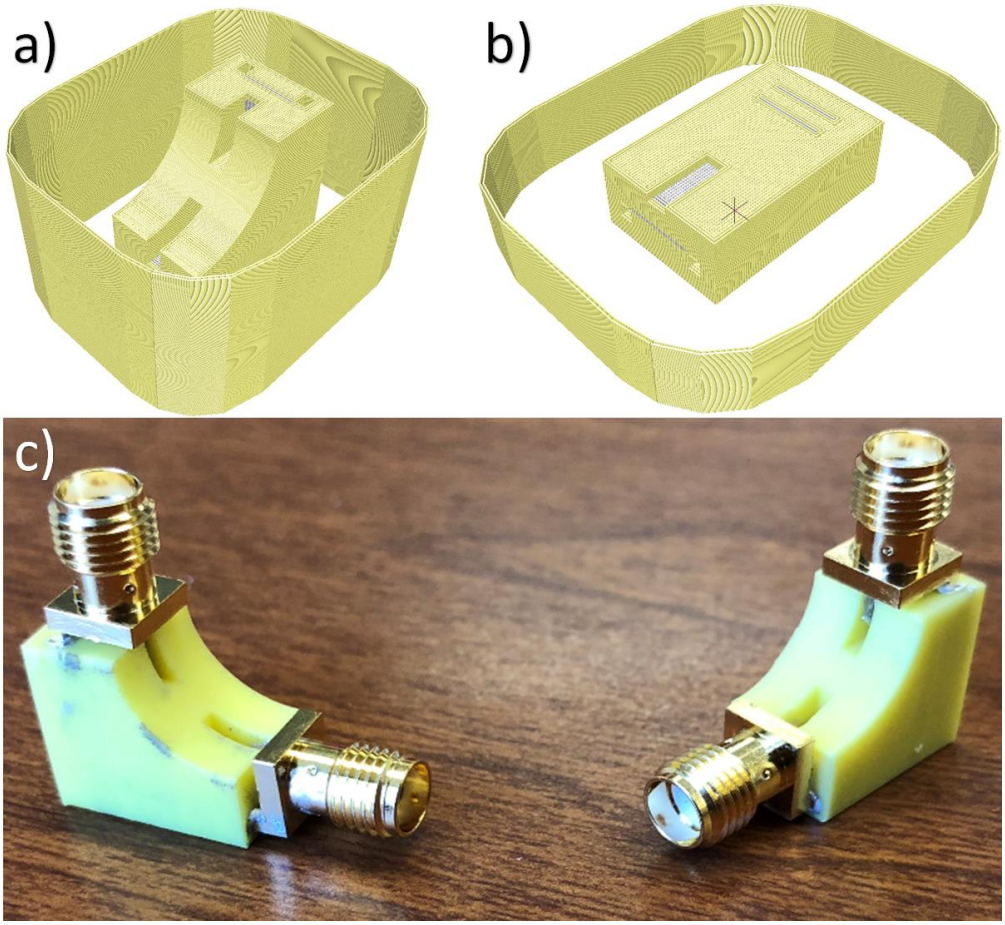

Figure 8.6: a) Layer #108 showing transition of PPTLs from horizontal to vertical. b) Layer #314 showing fully sliced model. c) Two 3DP out-of-plane bend PPTL with SMA connectors

8.4 Manufacturing Results, Expectations, and Foreseeable Complications

The slicing and 3D printing results worked as expected. The complexity of the PPTLs add to material resources, need more careful preparation before manufacturing processes, and require more research to produce higher quality functional devices. Overall, the most important problems with manufacturing the PPTLs were observed with surface roughness, CB028 ink gaps made by under dispensing, and over dispensing, and the need for a more sophisticated curing process that can speed time

by eliminating skirt rims, added priming towers, and reduce the added waiting time for layers to cure. Fragile SMA connections were noticed throughout evaluating the parts, oxidation of the silver lines and the need for acrylic film to protect devices are also needed. Table 8.3 shows the 3DP parameters for each PPTL design. Notice how the more complicated the design the more resources the manufacturing requires for a good print job. However, there is a noticeable saving of resources between the straight and in-plane bends. We see the biggest jump of parameters as the PPTLs bend out of plane and start meandering in all directions.

Table 8.3: Detailed results for the 3DP PPTL devices

Parameters	Straight	In-Plane Bend	Out-of-Plane Bend
Length of line (mm)	35	30	25
Printing time (hrs)	3	3.2	2.06
Layer count	140	140	366
Total number of lines	97,500	49,693	72242
Filament extruded (mm)	1,502	1023	787
Ink dispensed (mm)	22	14	12

As the print times go longer than nine hours, we foresee a problem with plastic O-rings. As the print job takes longer times, the small lower O-ring inside the valve takes mechanical abuse compromising its structure integrity, causing the opening/closing values for the valve to change. An evaluation of friction and heat is suggested, to understand the integrity of the O-rings inside the valve, alongside, the evaluation of different materials the O-rings can be made off. The use of an O-ring less valve is needed to avoid this problem. This valve is made entirely out of stainless steel with a tapered valve that does not require a ring.

8.5 MEASUREMENTS AND COMPARISONS

8.5.1 Measuring Techniques

Overall, the test results show agreement with the trends observed in simulation. However, there is a noticeable loss of power with a slight frequency shift overall measured results. All PPTLs were measured with an Agilent N5245A PNA-X VNA with a 1601-point sweep from 1 GHz to 10 GHz. The results display the simulated and measured S_{11} curve alongside S_{21} results for each PPTL. As each PPTL device is attached by SMA connectors, SMA cables were used with respective adaptors to match the impedance between the VNA; as shown in Figure 8.7. Each PPTL was calibrated and characterized using the Ecal

feature of the VNA. This feature did the testing of ports using a single connection rather than having to connect multiple “open”, “short”, and “load” devices. This Ecal calibration accounted for the adaptors, SMAs, and cables attached to the PPTL devices. Furthermore, an x-ray micro computed tomography (micro-CT) system was utilized to look at the parallel plates inside the ABS plastic; as shown in Figure 8.7. A Zeiss Xradia 520 micro-CT system to detect ink continuity and porosity.

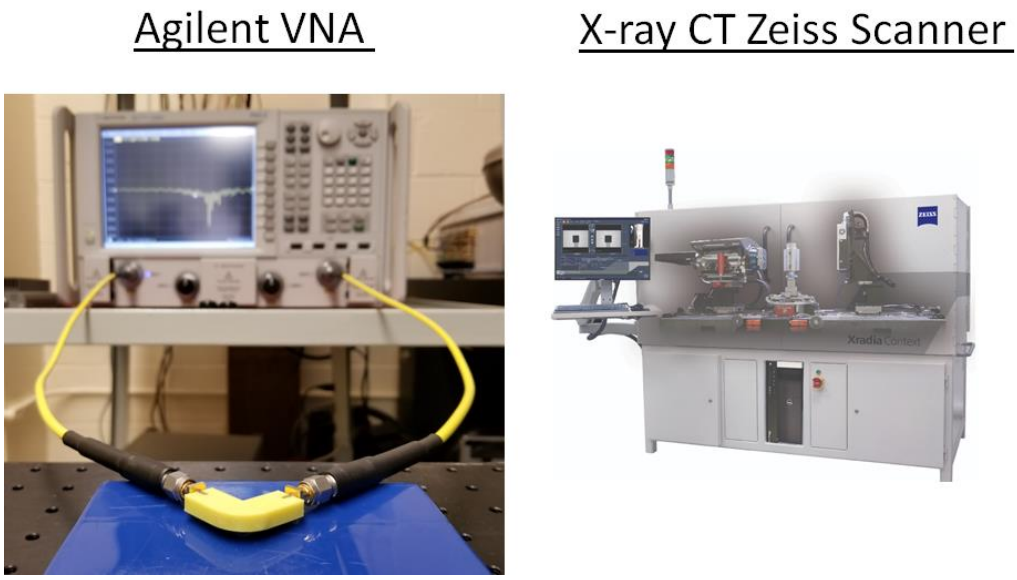

Figure 8.7: (Left) Agilent VNA uses SMA connectors attached along SMA cables with respective adaptors to match the impedance between the VNA and our devices. (Right) An x-ray micro-CT system was utilized to look at the parallel plates inside the ABS plastic

8.5.2 Results vs. Simulation

8.5.2.1 Straight PPTL

Figure 8.8 shows the measured vs simulated results from the straight PPTL. Dashed lines show the reflectance and transmittance of the models simulated using SMAs in Ansys HFSS. Solid lines show the measured results using an Agilent N5245A PNA-X Vector Network Analyzer. While the results are in good agreement, a slight decrease in power is seen in the measured results. Models were simulated using perfect conductors while in reality the lower conductivity of the silver ink when compared to copper would lead to higher ohmic losses in our devices. Another aspect to take into consideration is any inaccuracy in physical dimensions of the printed devices that would lead to a change in impedance. This

would create a mismatch between the transmission line and the 50 Ω SMA connectors that would also cause a decrease in transmitted power.

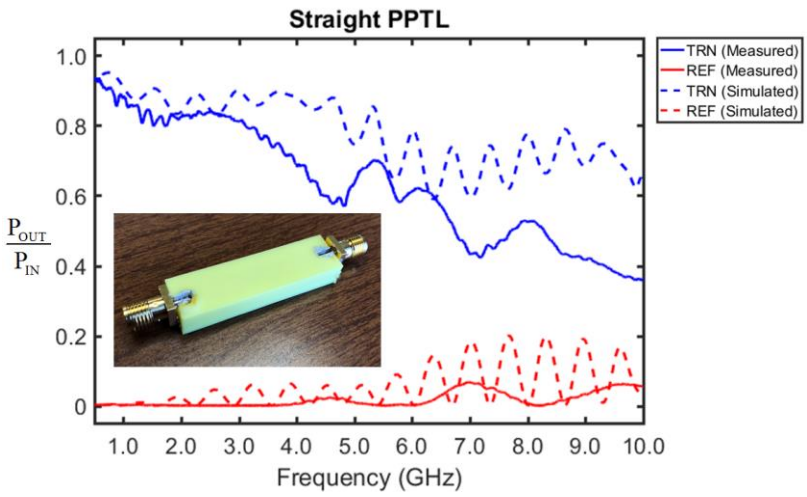

Figure 8.8: Straight PPTL simulated results plotted together with measured results.

8.5.2.2 In-Plane Bend PPTL

The results for all three in-plane bends are shown in Figure 8.9. The figure shows the simulated results as broken lines and the measured results as solid lines. Linear power transmittance and reflectance are shown in blue and red respectively. Conductive epoxy was not applied to the first in-plane bend, only to the second and third had epoxy to look for a noticeable difference. The strong deviation in the results in the first in-plane bend seem to reflect this decision. In the second and third in-plane bends, the results indicate a similar trend between the simulated and measured results. In addition to the reasons addressed with the straight PPTL, the decrease in transmittance may be a result from not changing the plate thickness as we did in the straight line and out-of-plane bends. The wider and thinner plate may have affected the sheet resistance and the overall performance of the device.

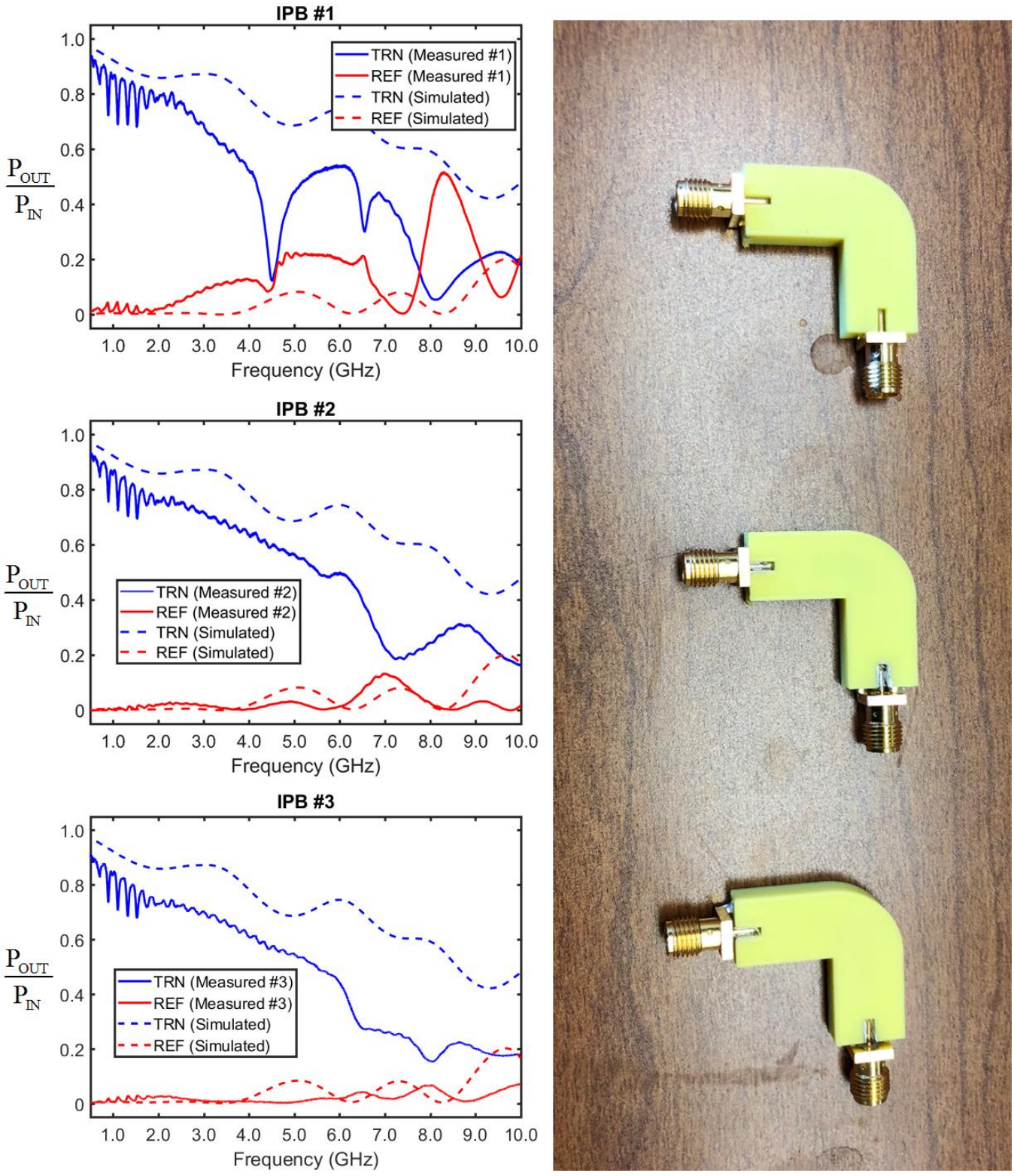

Figure 8.9: Measured vs. simulated results for in-plane-bend (IPB) PPTL #1, #2, and #3 in descending order.

8.5.2.3 Out-of-plane Bend

The measured results for the functioning out-of-plane PPTL are shown in Figure 8.10. This figure shows the simulated results in dashed lines (blue for transmittance and red for reflectance) and the measured results in solid colored lines. It can be seen that the simulated results and the measured results are in good agreement. We attribute the discrepancies in all of our simulations to variations and surface roughness in the printed part that are not accounted for in the simulation. The model for this PPTL had substantial changes done to the thickness of the parallel plates so the vertical plates could be recognized and by the slicing software. The model went from 75 µm to 200 µm adding volume to the metal conductors. The team believes that thicker plates contribute to the resistance propagation of surface waves since they have skin effects that help them propagate easier in thinner metals.

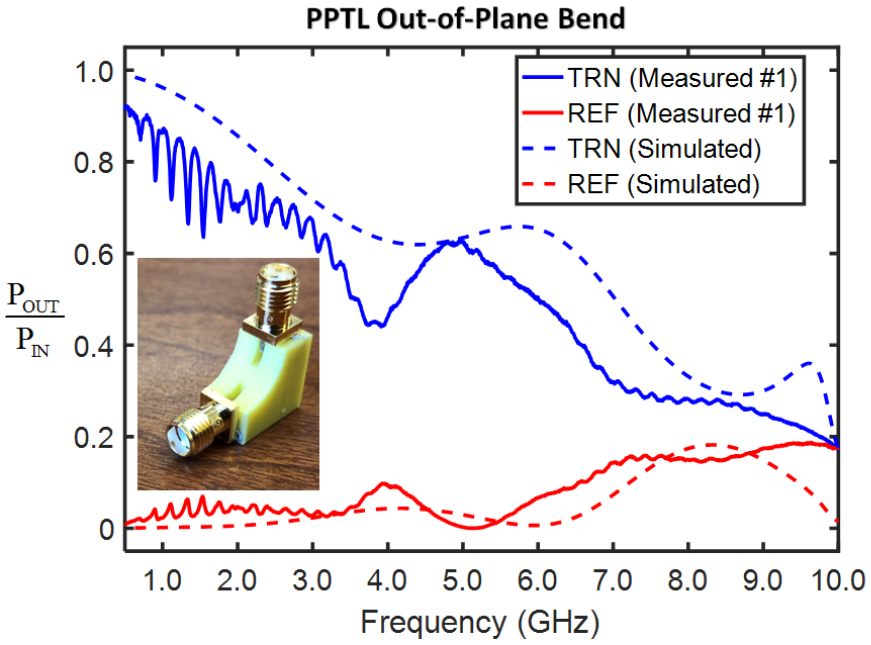

Figure 8.10: Measured vs. simulated results for out-of-plane bend (OPB) PPTL.

8.5.3 X-ray imaging

The Army Research Lab (ARL) utilized x-ray micro computed tomography (micro-CT), measured via a Zeiss Xradia 520 micro-CT system, to detect ink continuity and porosity. The sample showed ink present throughout the length of the parallel plate channels. Porosity was sufficient to make reliable electrical connections, but a few discontinuities were identified. Figure 8.11 shows the micro-CT ink PPTL on the left and the porosity and continuity readings on the right. The figure shows a translucent TL

when the contrast between a solid SMA connector and the printed PPTL is too great to compare in the same image. This required images for the plates to be taken apart from the SMA connectors to avoid the contrast problem. The parallel plates appear to look thin and transparent because the silver ink is very thin. Parts b) and c), show the porosity of the ABS plastic and the silver ink. Part b) displays a side view where the TLs are continuous. Likewise, part c) displays a section of the plates imbedded in plastic viewed from the top. The silver ink is dispensed properly and continuously through the PPTL.

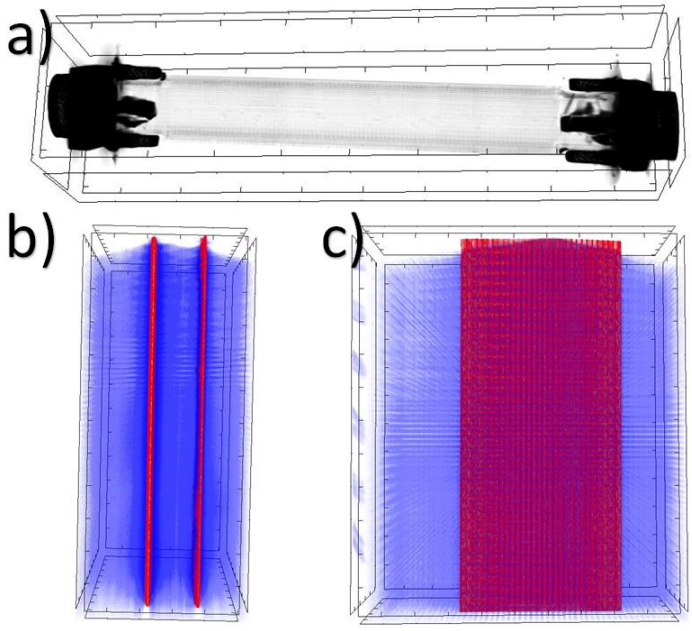

Figure 8.11: Straight PPTL x-ray tomography. Part a) highlights the straight PPTL with SMA connectors. Part b) side view of the parallel plates imbedded in plastic. Part c) top view of the parallel plates imbedded in plastic.

The in plane bend x-ray tomography shows a higher density on the plates. Agglomeration of silver ink particles can be appreciated throughout the plate in Figure 8.12 part b) and d). This is caused by debris coming from the SmartPump^{TM} pen tip. The density of the plastic looks the same as the straight PPTL. Part c) shows a side view on the in plane bend. Overall, the images show no breaks or holes in the metal or plastic parts. The surface roughness on the plates is a cause for skin effects and leads to power losses.

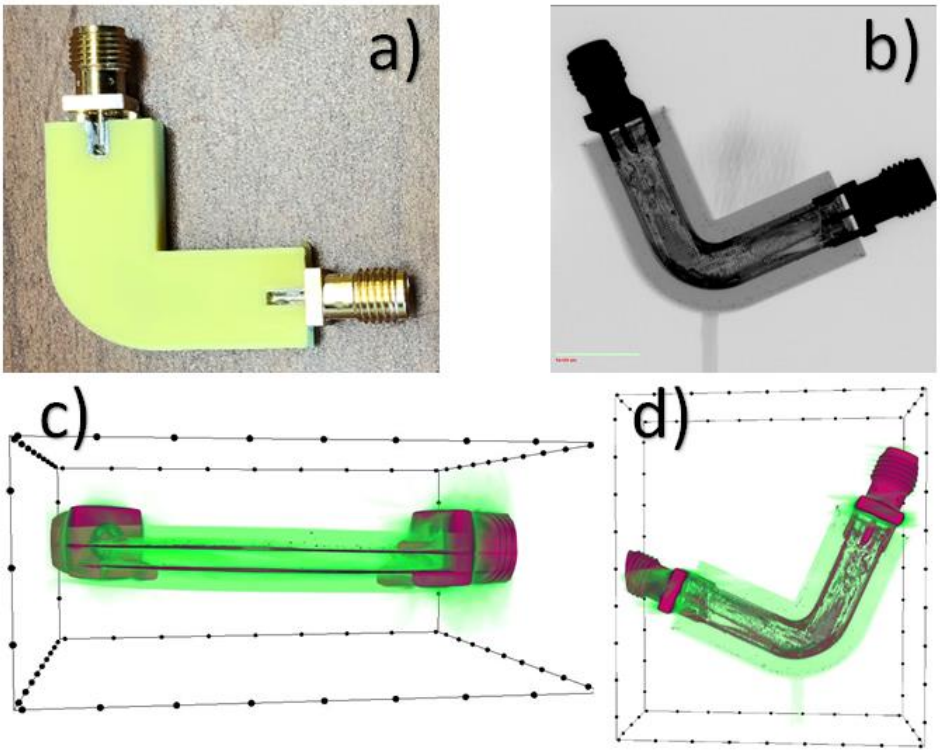

Figure 8.12: X-ray imaging of the in-plane PPTL bend. Part a) is the printed part for reference. Part b) shows the x-ray image from the top. Part c) side view of the PPTL with density of metals and plastics. Part d) bottom view with density tomography for metals and plastics.

The out-of-plane PPTL bend was x-rayed in the same manner as the previous devices. The imagining shows similar surface roughness as the in-plane bend in Figure 8.13. There are no breaks or holes through the metal plates or plastic structure. A higher density of metal can be appreciated since the line widths of the ink were made thicker than previous print models. Due to the surface roughness, the power losses are expected to be greater in the out-of-plane bend than the in-plane prints. The density of materials are shown in red for inks and green for plastics.

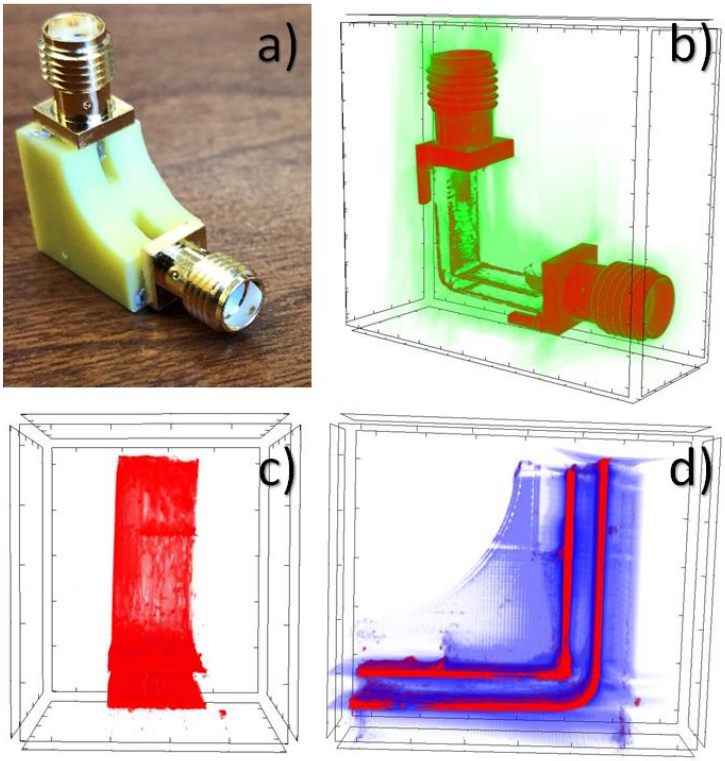

Figure 8.13: Out-of-plane PPTL x-ray tomography. Part a) shows the 3DP part for reference. Part b) side perspective on the bend. Part c) font view of the metal plates. Part d) shows a side view on the plates and plastics in blue.

The x-ray imaging showed the structural integrity of the printed PPTLs. On one hand, the prints show no breaks or holes affecting the plastic structure or the metal plates. The manufacturing process proved to build the models as planned. However, the imaging shows a surface roughness problem that affects power losses. It is recommendable to decrease the pen tips to create finer features and reduce the surface roughness seen across the prints. It is also necessary to add tools for the pen tips to be cleaned in between layers. This will reduce the accumulation of materials as they are dispensed between layers.

8.6 CONCLUSION

The team conducted a study where the surface roughness showed to be a contributing factor for power loss of the TLs. Figure 8.14 shows how power is lost if the plates printed are printed with a rougher surface. The enclosing of metal conductors needs to be improved by maintaining smooth and flat layers throughout the printing process. This can be achieved by milling in between layers, applying chemical abrasive substances to reduce scalloping, and reducing the size of the pen tips down to 12.5 µm.

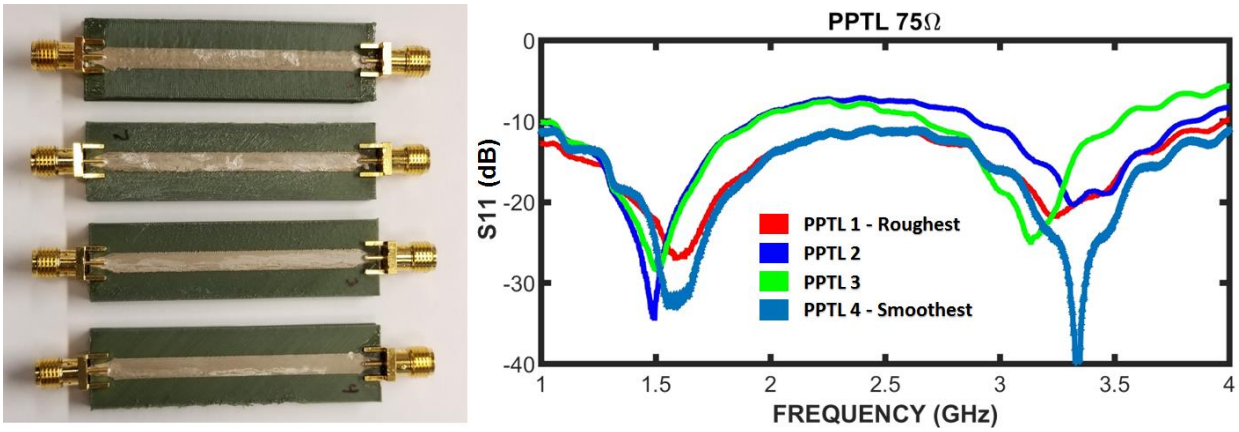

Figure 8.14: PPTL Surface roughness vs smoothness

There is a need for different measuring devices and techniques that can correct the problem between the SMA connectors and the PPTLs. The need is for further research that matches the shape of the mode traveling between the SMA and the PPTL. The use of Picoprobes model 40M that incorporate a balun is proposed for matching the connector transition. These probes work from DC up to 40 GHz. They feature customizable contacts that are spring loaded. However, adding contact pads to the PPTL would require careful design that may introduce problems.

This research studied arbitrarily placed and rotated PPTLs that were manufactured with hybrid 3DP. The electric field distribution in this line is also fairly contained. Therefore, these types of transmission lines operated in tight circuit configurations. Ideally, a coaxial transmission line would be better suited for this task. However, we avoided coaxial lines due to the high complexity of manufacturing these lines using hybrid 3D printing. While the results were not encouraging, they were excellent for the goals of this research. This opens the opportunity for further work on optimizing the SMA, designing a new transition between PPTL and the signal launch, or rethinking the way launches can be made with the use of hybrid 3DP.

8.6.1 Manufacturing

There is a pressing need for inks that can be used with smaller pen tip sizes, less abrasive, and easier to cure. The current curing methods used in this effort were adding time to the print job through the addition of skirts, letting the printed devices cool down through time as the inks cured, and the printing of thin ink layers that take very short times to cure. We also highlighted the need for insulated pen tips to

dispense materials that are not affected by the heat of the print. Sensors could be added in the nozzles to monitor viscosity and pressure. Cleaning tools can be added to eliminate the debris from pen tips between layers. As 3DP electronics get larger, the print jobs will take longer times an evaluation of friction and heat to understand the integrity of the O-rings inside the valve is needed. On the same note, there is also a need for an evaluation of different materials the O-rings can be made off. The use of an O-ring less valve is also suggested.

8.6.2 Follow-Up Research

The long-term version for 3D circuits will have components placed in any orientation and at any position throughout all three dimensions as illustrated in Figure 8.15. Interconnects will likely be differential or coaxial transmission lines meandering smoothly throughout the circuit. Future research includes 3D printing of high frequency interconnects, incorporating active devices, and forming passive 3D circuit elements such as filters and antennas.

Figure 8.15: Rendered model of meandering transmission lines.

A robust and generic slicing tool that handles every step of the automated hybrid printing process within one package is becoming much needed. It will handle everything from component 3D layout, routing interconnects, rules of printing, hybrid slicing, handling large data structures, incorporating advanced electromagnetic functionality, and 3DP. The use of Picoprobes® that can be used inside the printing envelope as the print job is built in real-time to ensure impedance and conductivity. We see the

slicing process interacting design files with the ability to calculate our own boolean functions, mesh healing, the use of voxelize functions into a 3D binary map that creates a path for every layer alternating material A and material B with spatially varied tool paths. Every step of the automated process from schematics and 3D electronic models to viewing of print paths and rendered functions. This will prove to be a highly enabling technology in many areas, even outside of electronics and electromagnetics. The long-term vision for 3D printed electronics is depicted in Figure 8.16 Where spatially variant anisotropic metamaterials bend fields away to avoid crosstalk between components. Filters can be design in very 3D fashions.

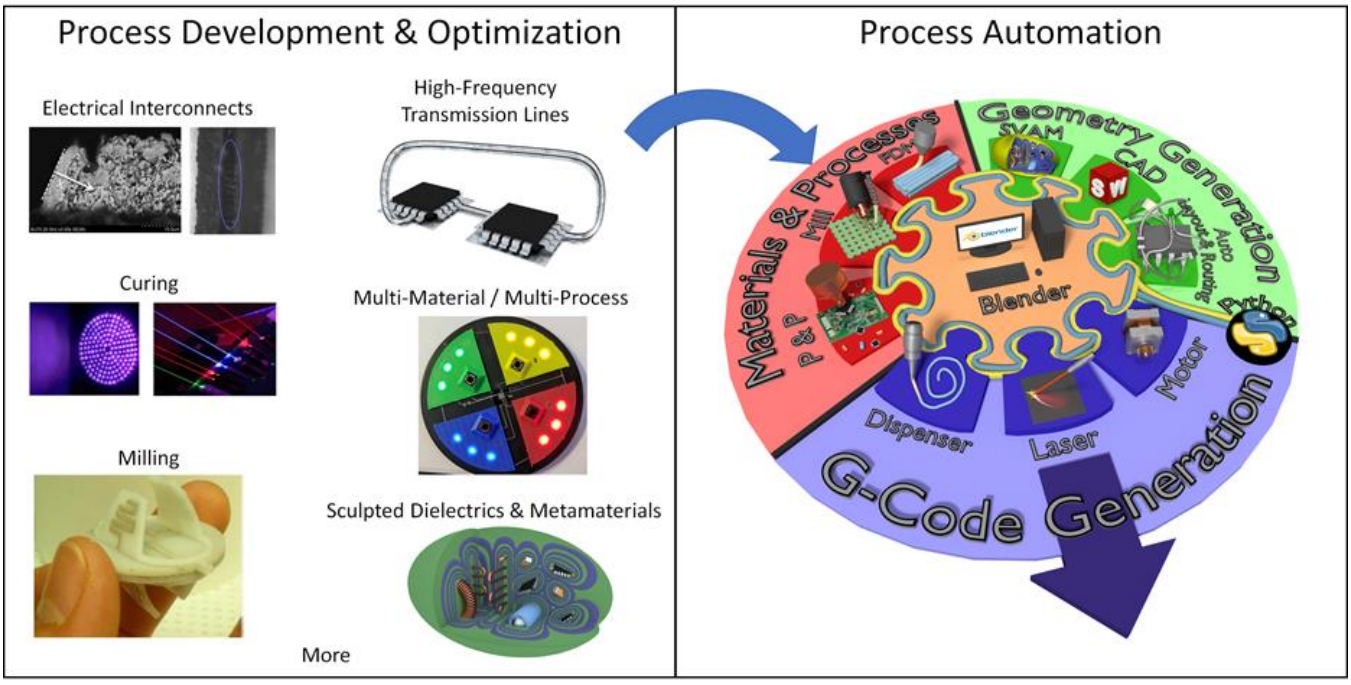

Figure 8.16: Long-term vision of automated hybrid 3DP electronics

References

[1] David Espalin, et al. 3D Printing Multifunctionality: Structures with Electronics. The International Journal of Advanced Manufacturing Technology. May 2014, Volume 72, Issue 5, pp 963-978

[2] Gibson, Ian, David W. Rosen, and Brent Stucker. Additive manufacturing technologies: rapid prototyping to direct digital manufacturing. Springer, 2010

[3] K. Church, et al., "Printed electronic processes for flexible hybrid circuits and antennas," Flexible Electronics & Displays Conference and Exhibition, 2009, vol., no., pp.1,7, 2-5 Feb. 2009

[4] Ubaldo Robles, Andelle Kudzal, Raymond C. Rumpf. Automated Hybrid 3D Printing of 3D Meandering Interconnects. IEEE Trans. on Components, Packaging, and Manufacturing, [Pending Review], 2018.

[5] H. Lipson and M. Kurman, Fabricated: The New World of 3D Printing. Hoboken, NJ, USA: Wiley, 2013.

[6] Amit J. Lopes, E. MacDonald, and R. Wicker. Integrating Stereolithography and Direct Print Technologies for 3D Structural Electronics Fabrication. University of Texas at El Paso, El Paso, Texas, United States. Rapid Prototyping Journal (Impact Factor: 2.03). 03/2012; 18(2):129-143.

[7] Clyde F. Coombs, Jr. 'Printed Circuits Handbook McGraw-Hill', Fifth Edition, 2001.

[8] E. G. Fubini and P. J. Sutro, "A Wide-Band Transformer from an Unbalanced to a Balanced Line," in Proceedings of the IRE, vol. 35, no. 10, pp. 1153-1155, Oct. 1947.

[9] Klopfenstein, R. W., "A Transmission Line Taper of Improved Design", Proceedings of the IRE, January 1956, pp. 31-35.

[10] K. Nam-Soo, H. N. Kenneth (2010, Nov.). "Future Direction of Direct Writing," J. Appl. Phys. 108, 102801.

[11] U. Robles, et al., "High Frequency Filters Manufactured using Hybrid 3D Printing Method." Progress In Electromagnetics Research, 2018 [Pending Review]

[12] J. Sorocki, S. Koryciak, I. Piekarz, S. Gruszczynski and K. Wincza, "Investigation on additive manufacturing with conductive PLA filament for realisation of low-loss suspended microstrip microwave circuits," 2017 International Conference on Electrical, Electronics and System Engineering (ICEESE), Kanazawa, 2017, pp. 48-51.

[13] T. P. Ketterl, et al., "A 2.45 GHz Phased Array Antenna Unit Cell Fabricated Using 3-D Multi-Layer Direct Digital Manufacturing" IEEE Transactions on Microwave Theory and Techniques, vol. 63, no. 12, pp. 4382-4394, Dec. 2015

[14] U. Robles, "3D Printed Impedance Elements by Micro-Dispensing," M.S. Thesis, University of Texas at El Paso, 2013.

[15] D. Roper, B. Good, R. McCauley, S. Yarlagadda, J. Smith, A. Good and M.S. Mirotznik, ' Additive Manufacturing of Graded Dielectrics', Smart Materials and Structures, Vol. 23, No. 4, April 2014.

[16] P. Deffenbaugh, "3D Printed Electromagnetic Transmission and Electronic Structures Fabricated on a Single Platform Using Advanced Process Integration Techniques," Ph.D. Dissertation, University of Texas at El Paso, August 2014.

[17] Li, P.A. Clarck, and K.H. Church, “Robust Direct-Write Dispense Tool and Solutions for Micro/Meso-Scale,” Proceedings of the 2007 International Manufacturing Science and Engineering Conference, MSEC2007. October 15-17, 2007, Atlanta, Georgia, USA.16

[18] Gilbert T. Carranza, et al. CAD Tool for Three-Dimensional Circuit Layout, Routing, and Manufacturing. IEEE Trans. on Components, Packaging, and Manufacturing, [Pending Review], 2018.

[19] nScrypt Specification Sheet “Table Top Printer Specification Sheet”. nScrypt Inc. Orlando, FL. [Online] http://www.nscrypt.com

[20] Seroglou, F., Koumaras, P. & Tselfes, V. Science & Education. Kluwer academic publishers (1998) 7: 261. https://doi.org/10.1023/A:1008649319416

[21] C. A. Balanis, Advanced Engineering Electromagnetics (Wiley, 1989).

[22] nScrypt Specification Sheet “SmartPumpTM 100 Specification Sheet”. nScrypt Inc. Orlando, FL. [Online] http://www.nscrypt.com

[23] nScrypt Specification Sheet “nFDTM Specification Sheet”. nScrypt Inc. Orlando, FL. [Online] http://www.nscrypt.com

[24] Technical Data Sheet “DuPont CB028 Silver Conductor” 19: 1345. doi:10.1007/BF02662823. [Online] http://www.mcm.dupont.com

[25] National Bureau of Standards. “Copper Wire Tables” Circular of the Bureau of Standards No.31, Vol. 31 pg. 71. MARCXML Washington Govt. Print, 1914.

[26] Epoxy Technology, Inc. EPO-TEK® H20E Technical Data Sheet.

[27] Epoxy Technology, Inc. EPO-TEK® 353 ND Technical Data Sheet.

[28] ANSYS® Academic Research Mechanical, Release 18.1, Help System, Coupled Field Analysis Guide, ANSYS, Inc.

[29] Agilent. PNA Series Network Analyzer Programming Guide. Firmware A.09.42 September 2011.

[30] Lu X, Lee Y, Yang SF, Hao Y, Ubic R, Evans JRG, Parini CG (2008) Fabrication of electromagnetic crystals by extrusion freeforming. Metamaterials 2(1):36–44.

[31] Lee Y, Lu X, Hao Y, Yang SF, Ubic R, Evans JRG, Parini CG (2007) Rapid prototyping of ceramic millimeterwave metamaterials: Simulations and experiments. Microw Opt Technol Lett 49 (9):2090–2093.

[32] Ubaldo Robles, Justin Kasemodel, Jose Avila, Tenoch Benitez, and Raymond C. Rumpf, "3D Printed Structures by Micro Dispensing Materials Loaded with Dielectric and Magnetic Powders," IEEE Trans. on Components, Packaging, and Manufacturing, Vol. PP, Issue 99, pp. 1-7, 2018.

[33] Mohammad Vaezi, Hermann Seitz and Shoufeng Yang, ‘A review on 3D micro-additive manufacturing technologies’, Int J Adv Manuf Technol (2013) 67:1721–1754, DOI 10.1007/s00170-012-4605-2# Springer-Verlag London, 2012

[34] Lu X, Lee Y, Yang SF, Hao Y, Ubic R, Evans JRG, Parini CG (2009) Fabrication of millimeter-wave electromagnetic bandgap crystals using microwave dielectric powders. J Am Ceram Soc 92 (2):371–378

[35] M. M. Abdin, J. Castro, J. Wang and T. Weller, "Miniaturized 3D printed balun using high-k composites," 2015 IEEE 16th Annual Wireless and Microwave Technology Conference (WAMICON), Cocoa Beach, FL.

[36] Smay JE, Gratson GM, Shepherd RF, Cesarano J, Lewis JA (2002) Directed colloidal assembly of 3D periodic structures. Adv Mater 14:1279–1283

[37] Silicone Solutions, "SS-3045," Cuyahoga Falls, OH 44224 [Online] Available: http://siliconesolutions.com/ss-3045.html

[38] Sigma Aldrich, "Strontium Titanate Powder, 5μm, 99%," SN: 12060-59-2 St. Louis, MO [Online] http://www.sigmaaldrich.com/sigma-aldrich/home.html

[39] D. Roper, B. Good, R. McCauley, S. Yarlagadda, J. Smith, A. Good and M.S. Mirotznik, ' Additive Manufacturing of Graded Dielectrics', Smart Materials and Structures, Vol. 23, No. 4, April 2014

[40] Planetary Centrifugal Mixer "THINKY MIXER ARE-310 THINKY USA. [Online] http://www.thinkyusa.com/products/item-all/rotation-revolution-mixer/are-310.htmlO.

[41] O. Luukkonen, S. I. Maslovski and S. A. Tretyakov, "A Stepwise Nicolson–Ross–Weir-Based Material Parameter Extraction Method," in IEEE Antennas and Wireless Propagation Letters, vol. 10, no., pp. 1295-1298, 2011.

[42] W. P. Mason and R. A. Sykes, "The use of coaxial and balanced transmission lines in filters and wide band transformers for high radio frequencies:' Bell Syst. Tech. J., vol. 16, pp. 275-302, 1937.

[43] R. Levy, S.B. Cohn, "A History of Microwave Filter Research Design and Development", Microwave Theory and Techniques IEEE Transactions on, vol. 32, pp. 1055-1067, 1984, ISSN 0018-9480.

[44] Pozar, David M. Microwave engineering. John Wiley & Sons, 2009.

[45] J. R. Aguilar, M. Beadle, P. T. Thompson and M. W. Shelley, "The microwave and RF characteristics of FR4 substrates," IEE Colloquium on Low Cost Antenna Technology (Ref. No. 1998/206), London, 1998, pp. 2/1-2/6.

[46] Kikinis R, Pieper SD, Vosburgh K (2014) 3D Slicer: a platform for subject-specific image analysis, visualization, and clinical support. Intraoperative Imaging Image-Guided Therapy, Ferenc A. Jolesz, Editor 3(19):277–289 ISBN: 978-1-4614-7656-6 (Print) 978-1-4614-7657-3 (Online)

[47] nScrypt proprietary software "PCAD". nScrypt Inc. Orlando, FL. [Online] http://www.nscrypt.com

[48] Hot-World GmbH & Co. KG. Repetier-Host. "3D printing Application". Knickelsdorf 4247877 Willich, Germany.

[49] A3200 Motion Composer Suite. 1994–2018 Aerotech Inc. Web https://www.aerotech.com

[50] Carl Zeiss, Inc. ZEISS Xradia 520 Versa Submicron X-ray Imaging. 07745 Jena, Germany microscopy@zeiss.com. [Online] www.zeiss.com/520-versa.

[51] J. Moore and H. Ling, "Characterization of a 90 degrees microstrip bend with arbitrary miter via the time-domain finite difference method," in IEEE Transactions on Microwave Theory and Techniques, vol. 38, no. 4, pp. 405-410, April 1990.

[52] Amphenol RF. RF Connector, SMA End Launch Jack for 0.062 inch PCB, 50 Ohm, Round Post Contact. Part number132322.

[53] DuPont et al. High Performance Perfluoroelastomer Parts. Kalrez® O-rings. 2018.

[54] Harvey Tsang, "Digital Processes and Characterization for Fabricating 3D RF Devices," Ph.D. Dissertation, University of Texas at El Paso, December 2016.

[55] P. I. Deffenbaugh, T. M. Weller and K. H. Church, "Fabrication and Microwave Characterization of 3-D Printed Transmission Lines," in *IEEE Microwave and Wireless Components Letters*, vol. 25, no. 12, pp. 823-825, Dec. 2015.

[56] E. A. Rojas-Nastrucci, T. Weller, V. L. Aida, F. Cai and J. Papapolymerou, "A study on 3D-printed coplanar waveguide with meshed and finite ground planes," *WAMICON 2014*, Tampa, FL, 2014, pp. 1-3.

Appendix

A. Balanced vs Unbalanced Signal

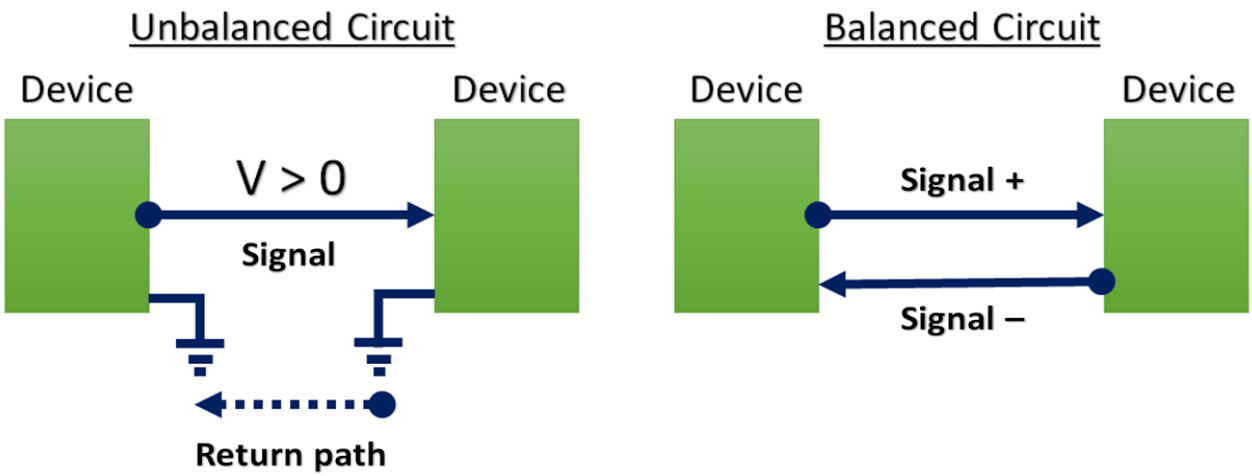

Figure A.1: Unbalanced and balanced circuits

B. Stepped Impedance Microstrip Line

All measurements calculated from the microstrip lines are derived from the measured S_{11} and S_{21}. The first equations in the Nicolson-Ross Weir method are:

$$X = \frac{{S_{11}}^2 - {S_{21}}^2 + 1}{2S_{11}}$$

$$r = X \pm \sqrt{X^2 - 1}\,, \qquad |r| \leq 1$$

$$t = e^{-\gamma l} = \frac{S_{11} + S_{21} - r}{1 - (S_{11} + S_{21})r}$$

Where r is the reflection coefficient between the microstrip and the SMA coaxial line, and t is the transmission coefficient (equivalent to the plane-wave equation) through the microstrip. We hypothesized that increasing reflections might give a more accurate conductivity measurement as an S_{11} close to 0 would appear to tend toward infinity. The model in Figure A.1 was used in simulation.

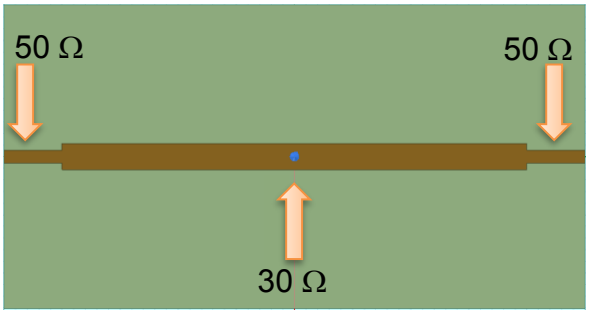

Figure B.1: Stepped Impedance Microstrip

A.1 Simulation Results

While the calculated loss of the stepped impedance microstrip was similar to that of the normal microstrip, there were errors encountered that seem to inhibit the measurement more than aiding it. When there are reflections present, the length of the entire line plays a notable role in the input impedance. At certain frequencies, transmission line acts as a quarter-wave transformer, and the microstrips input impedance increases rapidly towards infinity, causing a high amount of reflection. Using the original NRW method, the algorithm considers these high reflections as loss depicts this. Shown in Figure A.2.

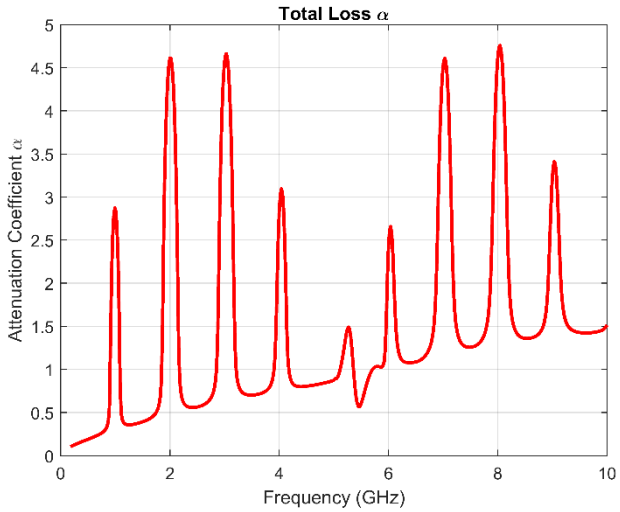

Figure A.2: Loss from Multi-Segmented Microstrip

In order to overcome these deviations, we eliminated the data containing high reflections. Interpolation was then performed to fill in the gaps. Figure A.3 shows the interpolated loss against the

original loss. Because of these drawbacks, we decided not to print the model described in Figure as it would not be beneficial.

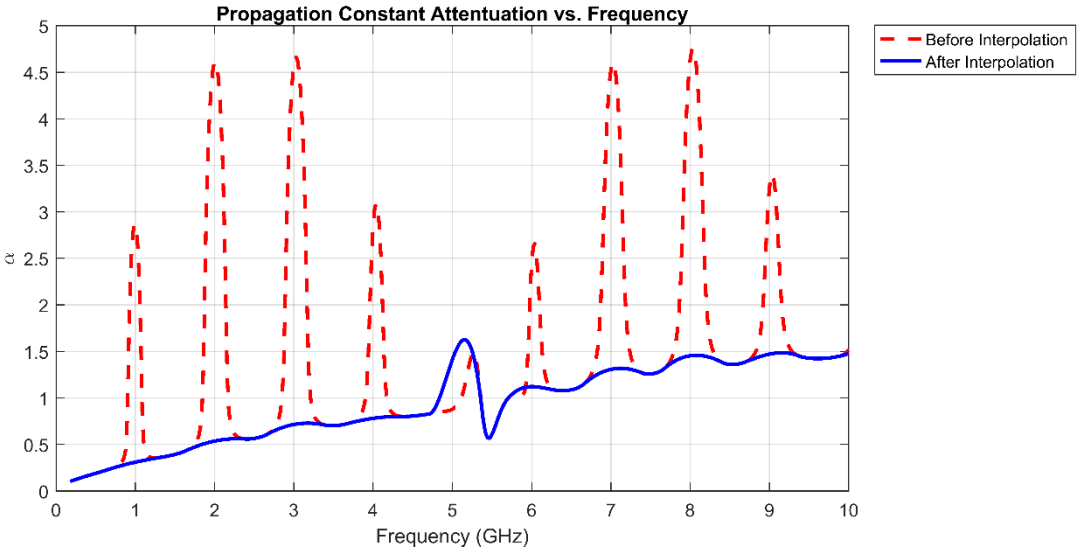

Figure A.3: Before and after interpolation on loss

While this technique may not improve the accuracy and consistency of the measurements, we do find its use as a general tool for measuring conductivity if unexpected reflections arise.

B. Absorptance and Attenuation Coefficient Relation

There are three primary ways of describing the percentage of power of a microstrip relative to the incident wave: power that is reflected (reflectance), power that is transmitted (transmittance), and power that is absorbed (absorptance). Reflectance may be calculated by squaring the magnitude of S_{11}. Similarly, transmittance can be calculated from squaring the magnitude of S_{21}. Using the symmetric Fabry-Perot model in Figure B.1, the reflection and transmission coefficients r and t previously described can also be calculated from S_{11} and S_{21}. Since we are interested in finding total loss described by η , the attenuation coefficient, we theorized that this total loss could be described mathematically in terms of absorptance.

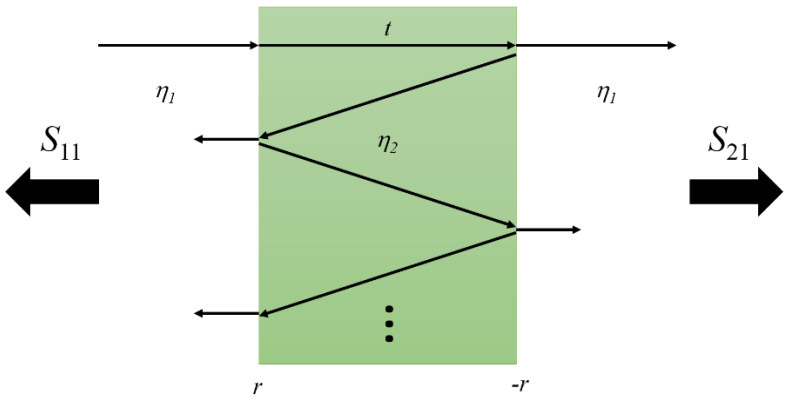

Figure B.1: Symmetric Fabry-Perot Model

The derivation comes from the Fabry-Perot model in Figure. Ignoring loss due to radiation, we can describe the total percentage in the microstrip with the following:

$$R + T + A = 1$$

$$S_{11}{}^2 + S_{21}{}^2 + A = 1$$

where *R*, *T*, and *A* are the reflectance, transmittance, and absorptance respectively. If we take the infinite sums of reflected and transmitted rays, we get the relations:

$$S_{11} = \frac{(1 - t^2)r}{1 - r^2t^2}$$

$$S_{21} = \frac{(1 - r^2)t}{1 - r^2t^2}$$

Inserting these into the last equation, we arrive at:

$$A = \frac{1 - r^2 - t^2 + 2r^2t^2 - r^4t^2 - r^2t^4 + r^4t^4}{1 - 2r^2t^2 + r^4t^4}$$

Because we want to analyze only the percentage of power absorbed by the medium (microstrip), we take the limit as *r* approaches zero, equivalent to perfectly matched impedances. This eliminates any loss effects due to reflection. The relation now becomes:

$$A = 1 - t^2$$

Finally, the equation can be reduced:

$$t^2 = e^{-2\gamma l} = 1 - A$$

$$e^{-2\alpha l} e^{-2j\beta l} = 1 - A$$

$$e^{-2\alpha l} = |1 - A|$$

$$\alpha = -\frac{1}{2l} \ln(|1 - A|)$$

In the final equation, the absolute value operation may be dropped as its operand will always be positive.

Vita

Ubaldo Robles Dominguez was born in Cd. Juarez, Chihuahua, Mexico. The third son of Eduardo Robles Sandoval and Dalia Dominguez Carrasco, he graduated from El Chamizal High School, Ciudad Juarez, Chihuahua, Mexico. In fall 2000, Ubaldo entered The University of Texas at El Paso as an International Student. While pursuing a bachelor's degree in electrical engineering, he was diagnosed with Leukemia at the same time that worked as a Mathematics and Science peer leader and tutor at UTEP. During the years 2002-2006 he co-founded and managed the SOLAPSUS café and tutoring center for students in Cd. Juarez, Mexico, while staying a student and a tutor in college. Later on, Ubaldo became the founder of the Automated Engineering Association in El Paso, TX under the leadership of Dr. Louis Everett. As an Electrical Engineer he worked as a Circuit Designer in the University of Texas at El Paso under several projects. Finally, in 2008 Ubaldo took the responsibility of managing the measurements laboratory for the Electromagnetics Laboratory, or EM Lab under the mentoring of Dr. Raymond C. Rumpf, while pursuing his Master's Degree in Science for Electrical Engineering. Ubaldo Robles has won "Best Student Presentation Award." And "Outstanding Paper Award" during IMAPS Advanced Technology Workshop on RF and Microwave Packaging. San Diego CA. February 7-8, 2012. Ubaldo has also proven to be an entrepreneur at heart by leading a team to win "Best Business Proposal" in the Paso Del Norte Venture Competition in El Paso, TX. Currently, Ubaldo Robles is pursuing his Doctoral Degree in Electrical Engineering while maintaining a research position and managing the 3D printing side of the laboratory in the EM Lab at the same time that he performs community work, fundraising, teaching, and mentoring at Intervarsity Christian fellowship helping students in college find the way of a truthful future.

Permanent address: Ubaldo.Robles@gmail.com

This dissertation was typed by Ubaldo Robles Dominguez.